

**A PRECISION MEASUREMENT OF THE NEUTRAL PION LIFETIME VIA
THE PRIMAKOFF EFFECT**

A Dissertation Presented

by

ERIC R. I. CLINTON

Submitted to the Graduate School of the
University of Massachusetts Amherst in partial fulfillment
of the requirements for the degree of

DOCTOR OF PHILOSOPHY

July 2007

Physics

© Copyright by Eric R. I. Clinton 2007

All Rights Reserved

**A PRECISION MEASUREMENT OF THE NEUTRAL PION LIFETIME VIA
THE PRIMAKOFF EFFECT**

A Dissertation Presented

by

ERIC R. I. CLINTON

Approved as to style and content by:

Rory Miskimen, Chair (Professor of Physics)

Barry Holstein (Professor of Physics)

David Lawrence (Adjunct Assistant Professor)

John Kwan (Professor of Astronomy)

Jonathan L. Machta, Department Head
Department of Physics

DEDICATION

For my wife, Jennifer, who put up with my often hectic and unpredictable schedule, my incomprehensible babble regarding physics analysis during long walks with our dogs, and my iconoclastic and socially gauche sense of humor.

Love you, 'Nnifer.

ACKNOWLEDGMENTS

I did not finish the dissertation without help. I have stood on the shoulders of giants. Some were people like my advisor Dr. Rory Miskimen of UMass Amherst and my mentors Dr. David Lawrence and Dr. Michael H Wood, both formerly UMass Amherst Post Doctoral Research Associates. Others were my colleagues in the PrimEx collaboration, with whom I have worked for the past eight years in furtherance of measuring this little bit of physics. And finally my family: my wife Jennifer, parents George and Susan, and sisters Melissa and Cheryl.

Thank you all for your unyielding support, knowledge, and care.

ABSTRACT

The neutral pion radiative width has been measured to $8.411 \text{ eV} \pm 1.8\% + 1.13\% - 1.70\%$ (lifetime = $7.826 \pm 0.14 + 0.088 - 0.133 \times 10^{-17} \text{ s}$) utilizing the Primakoff effect and roughly 4.9 to 5.5 GeV photons at the Thomas Jefferson National Accelerator Facility in Newport News, VA. The Hall B Photon Tagger, the Hall B Pair Spectrometer, a state of the art Hybrid Calorimeter enabled precision incident photon energy measurement, photon flux measurement, and neutral pion identification, respectively. With these and other hardware and software tools, elastic neutral pion yields were extracted from the data. A well developed and understood simulation calculated geometric and software cut efficiency curves. The simulation also provided photo-pion production response functions to fit the experimental cross sections and extract the Primakoff cross section and thus the neutral pion radiative width and lifetime. Future work includes improving understanding of the nuclear incoherent process and any other background sources of elastic neutral pions in this data.

A PRECISION MEASUREMENT OF THE NEUTRAL PION LIFETIME VIA THE PRIMAKOFF EFFECT

FEBRUARY 2008

ERIC R. I. CLINTON, B.S, WORCESTER POLYTECHNIC INSTITUTE

M.S., UNIVERSITY OF MASSACHUSETTS AMHERST

Ph.D., UNIVERSITY OF MASSACHUSETTS AMHERST

Directed by: Professor Rory Miskimen

TABLE OF CONTENTS

	Page
ACKNOWLEDGMENTS	v
ABSTRACT.....	vi
LIST OF TABLES	x
LIST OF FIGURES	xi
INTRODUCTION	1
1.1 Introduction.....	1
PHYSICS MOTIVATION.....	3
2.1 Low Energy QCD, Chiral Perturbation Theory, and the Primakoff Effect.....	3
PREVIOUS EXPERIMENTS	7
3.1 Overview.....	7
3.2 Direct Method	7
3.3 $\gamma\gamma$ Collisions	8
3.4 The Primakoff Effect	9
3.5 Final remarks on previous experiments	10
THE EXPERIMENT	11
4.1 Overview.....	11
4.2 Experimental Setup.....	15
4.2.1 PrimEx Experimental Targets.....	17
4.2.2 Carbon Target Thickness Measurement	18
4.2.3 The TJNAF Hall B Photon Tagger	21
4.2.4 Scintillating Fiber (SciFi) Photon Beam Monitor.....	23
4.2.5 Determining electron and photon beam characteristics and trajectory	25
4.2.6 The Total Absorption Counter and Absolute Photon Flux	34
4.2.7 The Pair Spectrometer and Relative Photon Flux.....	36
4.2.8 PrimEx Hybrid Calorimeter (HYCAL)	41
4.2.9 HyCal Charge Particle Veto Counters	50
4.2.10 The Light Monitoring System.....	55
4.2.11 PrimEx Data Acquisition, Trigger Design, and Event Rate	56
BACKGROUND SUBTRACTED NEUTRAL PION ANGULAR DISTRIBUTION ..	61
5.1 Data Source.....	61

5.2 Method of event selection and evaluation of selection misidentification	63
5.3 Yield extraction from HyCal Tungstate. Mass and Elasticity Correlation Enhancement.....	69
5.3.1 Mass and Elasticity Correlation Enhancement	69
5.3.2 Signal and Background Lineshape and Integration Range	71
5.3.3 Maximizing pion signal to noise.....	76
5.3.3.1 Elastic Pion Yield Versus Timing Window.....	77
5.3.3.2 Elastic Pion Yield Versus Fit Range.....	78
5.3.3.3 Elastic Pion Yield Versus Background subtraction range.....	80
5.3.3.4 Background subtracted, in-time, elastic π^0 yields.....	82
5.4 Systematic error in yield extraction method	82
5.4.1 Systematic error in signal and background lineshape choice	83
5.4.2 Systematic error from Hybrid Mass spectrum construction	85
5.4.3 Systematic error in cluster position finding algorithm.	86
5.5 Yield extraction with full HyCal acceptance	86
5.6 Yields, charged particle veto applied.....	93
PRIMEX MONTE CARLO SIMULATION DEVELOPMENT, RESULTS, AND OTHER EXPERIMENTAL INEFFICIENCIES	99
6.1 Monte Carlo location in the PrimEx software release	99
6.2 Energy leakage correction, tracking threshold study, resolution tuning	100
6.2.1 Energy leakage correction.....	101
6.2.2 GEANT tracking threshold in HyCal.	103
6.2.3 Invariant mass resolution tuning.....	104
6.3 Geometric, reconstruction/resolution, and software cut efficiency calculations	109
6.4 Small π^0 production angle Resolution Effects	117
6.5 Validity of the simulation	120
6.5.1 Recreation of the experimental angular spectrum	121
6.5.2 Effects of a dead detector or detectors.....	124
6.5.3 Trigger efficiency study.....	128
6.6 Comparison of Cluster Position Finding Methods.....	130
6.7 PrimEx Target Thickness effective pt and Photon Flux Calculation	132
EXTRACTION OF THE π^0 RADIATIVE WIDTH AND FUTURE WORK	134
7.1 Obtain normalized yields	134
7.2 Generation of simulated normalized yields and fit to physical data	134
7.3 Acceptance corrected cross sections.	137
7.4 Error and Systematic Uncertainty Estimation.....	137
7.4.1 Photon Flux.....	138
7.4.2 Timing accidental suppression and charge particle veto misidentification	138

7.4.3 Cluster Position Reconstruction.....	138
7.4.4 Target Thickness.....	139
7.4.5 Yield Extraction, Possible Fitting Range Systematics.....	139
7.4.6 Yield Extraction, Possible Integration Systematics.....	139
7.4.7 Yield Extraction, Signal and Background Lineshape Degrees of Freedom.....	139
7.4.8 Total Error Budget.....	140
7.5 Preliminary radiative width.....	140
7.6 Future work.....	141
7.6.1 “Conjoined” tungstate and lead glass analysis.....	141
7.7.2 Additional nuclear incoherent photopion production models.....	142
7.7.3 The ω background contribution.....	142
7.7.4 Evolving the cross sections to one photon energy.....	144
APPENDICES	145

RUN LIST FOR TAGGER RADIATORS A AND B ... **Error! Bookmark not defined.**

LIST OF HYCAL SIMULATION ANODE/DYNODE CHANNELS**Error! Bookmark not defined.**

PHOTON FLUX AND ENERGY BINNING **Error! Bookmark not defined.**

CROSS SECTIONS..... **Error! Bookmark not defined.**

REFERENCES **Error! Bookmark not defined.**

LIST OF TABLES

Table	Page
Table 1.1: Summary of PrimEx projected experimental error.....	14
Table 4.2: HOPG Elemental Analysis	19
Table 7.1: Cluster Position Systematic Error.....	138
Table 7.2: Background and Signal Model Systematic Error	139
Table 7.3: Table 7.3: Total Error Accounting.....	140

LIST OF FIGURES

Figure	Page
1.1. The Primakoff Effect.....	2
2.1. The axial anomaly, also known as the “triangle” anomaly.....	3
2.2. Summary of experimental and theoretical $\pi_0 \rightarrow \gamma\gamma$ decay width.....	6
3.1. The Direct Method.....	8
3.2. $\gamma\gamma$ Collisions.....	9
4.1. Total neutral pion cross section for ^{12}C	13
4.2. The conceptual PrimEx Setup in Hall B.....	17
4.3. The HOPG target placed in the support and mounting frame.....	18
4.4. Electron micrograph scan of HOPG surface.....	19
4.5. Water immersion density measurements.....	20
4.6. Target Masks for ^{12}C	20
4.7. The Hall B Photon Tagger.....	22
4.8. The Sci-Fi monitor PMT’s and electronics (left), light guides (center), and fibers (right side).....	24
4.9. The Sci-Fi monitor, both planes assembled.....	25
4.10. Calibrated beam position from “Double Arm Compton” data.....	26
4.11. BPM 2C24A electron beam position data.....	27
4.12. Non-calibrated Sci-Fi monitor photon beam position.....	27
4.13. Summary of Sci-Fi, HyCal, “Double Compton” and BPM data.....	28
4.14. Survey calibrated Sci-Fi monitor photon beam position.....	29
4.15. Graphical explanation of beam path parameterization.....	29

4.16.	Double Compton extracted beam position for roughly 1 st half of data.....	30
4.17.	Double Compton extracted beam position for 2 nd half of data.....	31
4.18.	Sample Tagger Electron harp scan.....	32
4.19.	A Tagger Photon harp scan, before physics target, just after Tagger radiator. Parameters p_0/p_3 , p_1/p_4 , and p_2/p_5 are the amplitude, mean, and sigma of a gaussian, respectively	32
4.20.	Sample Physics Target Photon harp scan. Parameters p_0/p_3 , p_1/p_4 , and p_2/p_5 are the amplitude, mean, and sigma of a gaussian, respectively.....	33
4.21.	Tagging Ratios (R_{abs}) as a function of T-Counter for various calibration currents.....	36
4.22.	The Pair Spectrometer telescopes and helium bag (foreground) and the blue PS magnet. Beam direction points along aperture of PS magnet through helium bag.....	37
4.23.	B-field map of the Pair Spectrometer dipole at a central field of 1 Tesla.....	38
4.24.	Sample Pair Spectrometer telescope high voltage plateau.....	39
4.25.	Relative tagging ratios (with contamination) vs. run number.....	41
4.26.	Sample Lead Tungstate (smaller) and Lead Glass blocks used in HyCal.....	42
4.27.	Sample Lead Tungstate module.....	43

4.28.	Sample Lead Glass module.....	44
4.29.	Back view of HyCal chassis showing custom printed circuit boards handling ~5000 data channels from HyCal.....	45
4.30.	Front view of HyCal, fully stacked with inset Tungstate.....	46
4.31.	Front and view of HyCal and chassis in “run configuration”.....	47
4.32.	Views of HyCal, chassis, and cable handling while on the HyCal Transporter.....	49
4.33.	Placement of the Veto Counters in from of HyCal.....	51
4.34.	Veto Counter Rate vs. Central Hole size Simulation study.....	52
4.35.	Rate versus Hole Size, all events less then 2.26 cm from Beam Center excluded, simulated.....	52
4.36.	Photon Conversion efficiency for a typical veto counter.....	54
4.37.	Charged particle detection efficiency midline along HyCal and veto counters.....	55
4.38.	PrimEx Fastbus Data Acquisition Set-up.....	57
4.39.	Blocks of like detectors going to individual UVA 120 modules.....	58
4.40.	PrimEx electronics and cabling.....	59
5.1.	Sample skewed Gaussian fit of Tagger-HyCal total Sum co-incidence after Likelihood selection.....	64
5.2.	Skewed Gaussian with cubic background fit of elasticity for all cluster pair types.....	65
5.3.	Skewed Gaussian with cubic background fit of reconstructed mass for all cluster pair types.....	66

5.4.	Final likelihood for most likely entries with time cut from 5.3.7.....	68
5.5.	Misidentification of events with entries in different angular bins.....	68
5.6.	Angular distribution of Most Likely vs. Next Most Likely entries and “Most Likely π^0 production angle - Next Most Likely π^0 production angle”.....	69
5.7.	Correlation of Mass and Elasticity for selected angles.....	72
5.8.	Projection of (HyCal tungstate acceptance) data onto the Orthogonal axis.....	72
5.9.	Correlation of Mass and Elasticity for selected angles with diffuse background cut away.....	73
5.10.	Pion candidates removed by the “diffuse cut”.....	74
5.11.	Sample Fits at selected π^0 production angle bins, HyCal tungstate acceptance.....	75
5.12.	π^0 Yield as a Function of Angle, HyCal tungstate acceptance.....	76
5.13.	Elastic pion yield as a function of the timing window, HyCal tungstate acceptance.....	77
5.14.	Elastic pion yield as a function of photonuclear process dominated angular regions and the fitting range, integration range = 0.022 HMU’s, HyCal tungstate acceptance.....	79
5.15.	Radiative width as a function the fitting range, integration range = 0.022 HMU’s, HyCal tungstate acceptance.....	80
5.16.	Elastic pion yield as a function of photonuclear process	

	dominated angular regions and integration range.....	81
5.17.	Radiative width as versus integration range.....	82
5.18.	Graphical explanation of the parameters varied for elastic yield plateauing studies and the contributor to systematic effects in yield extraction methodology.....	84
5.19.	Comparing various lineshapes, all normed to double regular gaussians with a cubic background, HyCal tungstate acceptance.....	85
5.20.	Projection of (entire HyCal acceptance) data onto the Orthogonal axis.....	87
5.21.	Sample Hybrid Mass fits using entire HyCal acceptance.....	88
5.22.	Elastic pion yield as a function of the timing window, entire HyCal acceptance.....	89
5.23.	Elastic pion yield as a function of photonuclear process dominated angular regions and integration range, entire HyCal acceptance.....	90
5.24.	Elastic pion yield as a function of photonuclear process dominated angular regions and fitting range, integration range = 0.022 HMU's, entire HyCal acceptance.....	91
5.25.	Comparing various lineshapes, all normed to double regular gaussians with a cubic background, full HyCal acceptance.....	92

5.26.	Elastic π^0 Yield, full HyCal acceptance.....	93
5.27.	Effect of the Veto Counters on PrimEx π^0 candidate spectra.....	96
5.28.	Extracting a “photon misidentification efficiency”.....	97
5.29.	Notch effect, full HyCal acceptance.....	98
6.1.	Ratio of HyCal Cluster pair energy and Thrown Photon energy – Simulation.....	101
6.2.	Ratio of energy not contained in cluster pair (but deposited in HyCal) and Thrown Photon energy – Simulation.....	102
6.3.	Ratio of energy not contained in cluster pair and Thrown Photon energy – Physical Data.....	102
6.4.	Elasticity (post energy correction) as a function of reconstructed ‘X’ position of cluster for both high and low energy decay photons.....	103
6.5.	Invariant Mass and Elasticity Spectrums for all physical data, no event likelihood selection.....	105
6.6.	Invariant Mass and Elasticity spectrums for tracking threshold of 10 keV. Resolution has also been5 tuned to physical spectrum.....	106
6.7.	Invariant Mass and Elasticity spectrums for tracking threshold of 100 keV. Resolution has also been tuned to physical spectrum.....	107
6.8.	Invariant Mass and Elasticity spectrums for tracking threshold of 500 keV. Resolution has also been tuned	

	to physical spectrum.....	108
6.9.	Invariant Mass and Elasticity spectrums for tracking threshold of 1000 keV. Resolution has also been tuned to physical spectrum.....	109
6.10.	Geometric acceptance over entire HyCal	110
6.11.	Geometric acceptance over HyCal tungstate.....	111
6.12.	Geometric and geometric×reconstruction efficiencies for all photo-nuclear processes, entire HyCal acceptance.....	112
6.13.	Geometric and geometric×reconstruction efficiencies for all photo-nuclear processes, tungstate only acceptance.....	113
6.14.	Reconstruction efficiencies for all photon-nuclear processes, entire HyCal acceptance.....	114
6.15.	Reconstruction efficiency, summed over all photon-nuclear processes, entire HyCal acceptance.....	115
6.16.	Reconstruction efficiencies for all photon-nuclear processes, tungstate only acceptance.....	116
6.17.	Reconstruction efficiency, summed over all photon-nuclear processes, tungstate only acceptance.....	117
6.18.	Shifting of thrown small angle events to larger reconstructed angles	118
6.19.	Reconstructed vs. Thrown Primakoff Production Angle. Note the large “background” at small production angle.....	119
6.20.	Thrown small angle events are getting pushed out to higher	

	reconstructed angles due to limited phase space.....	120
6.21.	Original physical π^0 candidate angular spectrum before and after running through simulation, entire HyCal acceptance.....	122
6.22.	Original physical π^0 candidate angular spectrum before and after running through simulation, HyCal tungstate acceptance.....	122
6.23.	Location of physics events that failed to reconstruct after passing through simulation, HyCal tungstate acceptance.....	123
6.24.	Original physical π^0 candidate angular spectrum, before simulation and after photon vertical and horizontal momenta rotation and through simulation, HyCal tungstate acceptance.....	123
6.25.	How acceptance with dead <i>tungstate</i> detectors changes with respect to full acceptance, <u>total HyCal</u> acceptance.....	126
6.26.	How acceptance with dead <i>glass</i> detectors changes with respect to full acceptance, <u>total HyCal</u> acceptance.....	127
6.27.	How acceptance with dead <i>tungstate</i> detectors changes with respect to full acceptance,	

	<u>HyCal tungstate</u> acceptance only.....	128
6.28.	How acceptance with dead <i>tungstate dynodes</i> changes with respect to full acceptance, <u>HyCal tungstate</u> acceptance only.....	129
6.29.	Comparing cluster position finding algorithms. Full HyCal acceptance, 36 million events thrown, ~21.8 million accepted.....	131
6.30.	Comparing cluster position finding algorithms. HyCal tungstate acceptance, 36 million events thrown, ~13.2 million accepted.....	132
6.31.	Photon Flux for ^{12}C data, tagger rad. B. Total Flux = 3.34898×10^{12} photons.....	133
7.1.	Acceptance Uncorrected Differential Cross Section, a.k.a. Normalized Yields.....	136
7.2.	Normalized Yields with Fit to 2.5° , HyCal tungstate acceptance.....	136
7.3.	Acceptance corrected cross sections, HyCal tungstate acceptance.....	137
7.4.	“Conjoined” yields.....	141
7.5.	Efficiency to accept coherent ω event.....	143
7.6.	Reconstructed π^0 candidate spectra from coherent ω background.....	143

CHAPTER 1

INTRODUCTION

1.1 Introduction

The neutral pion lifetime is arguably the most precise theoretical calculation possible in low energy QCD, but the current world's data are not commensurate with theory. Recent calculations predict a neutral pion radiative width of $8.1 \text{ eV} \pm 1\%$ [1 & 2], while the PDG average stands at $7.84 \text{ eV} \pm 7\%$. The Primakoff Experiment (PrimEx) collaboration has utilized the Primakoff effect (Figure 1.1), photo-meson production in the Coulomb field of nuclei, to generate neutral pions. The Primakoff process is particularly advantageous because the π^0 lifetime is directly proportional to the Primakoff cross section. The real ($\sim 6\text{GeV}$) photons required to irradiate the nuclear targets were created using the Hall B photon tagger at Jefferson Lab. The interaction of a real photon with a virtual photon from the nuclear targets creates a π^0 . This neutral pion then decays ($\sim 98.8\%$ of the time) into two real photons via the chiral anomaly [3]. These decay photons are then detected in a calorimeter, where both energy and position information can be inferred. From this data, the 4-vectors of the original neutral pion can be reconstructed. A differential cross section can be extracted over small pion production angles from the elastic π^0 yields. The collaboration had expectations to measure the Primakoff contribution, and thus the π^0 radiative width, to a precision of 1.5%.

The timeliness of this experiment is important. As mentioned, the PDG's radiative width for the π^0 is only known to within 7%. Recent theoretical calculations have

reached very impressive precision and agreement. Finally, any measurement of the π^0 radiative width is arguably the most fundamental test of low energy QCD and Chiral Perturbation Theory possible with few GeV photons. The latest theoretical results, the paucity of an experimental measurement of commensurate precision, and the fundamental nature of the neutral pion lifetime underscore the importance of the result of the PrimEx collaboration and this dissertation. The collaboration hopes to measure the π^0 radiative width to a precision of 1.5%.

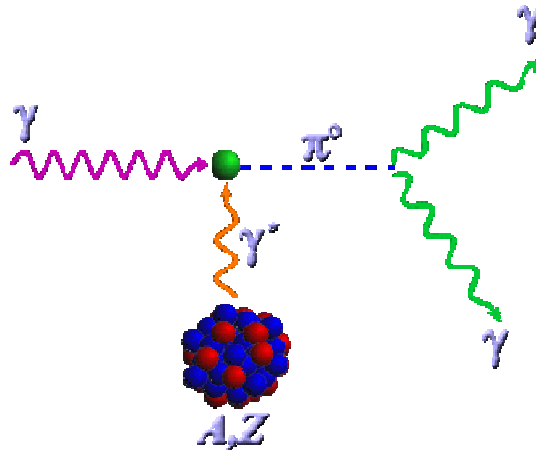


Figure 1.1: The Primakoff Effect

CHAPTER 2

PHYSICS MOTIVATION

2.1 Low Energy QCD, Chiral Perturbation Theory, and the Primakoff Effect

The axial anomaly (Figure 2.1) is one of the most profound and fundamental examples of spontaneous symmetry breaking in quantum mechanics. The axial anomaly arises from the coupling of quarks and gluons to the U(1) symmetry of the classical Lagrangian in QCD in the chiral limit where quark masses approach zero. In the axial anomaly coupling of the π^0 to a pair of photons, the divergence of the axial-vector current becomes proportional to the product of $E_a \cdot B_a$ of the chromo electric and chromo magnetic fields.

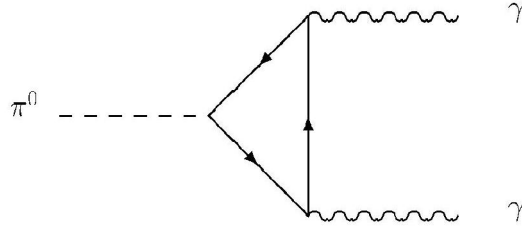


Figure 2.1: The axial anomaly, also known as the “triangle” anomaly

If the discussion is limited to the axial anomaly that couples quarks to photons [3, 4 & 5] and only the two lightest quarks flavors, u and d, the isotriplet axial vector current is $\bar{q}I_3\gamma_\mu\gamma_5q$. If still using the exact isospin symmetry, the π^0 only couples to the electromagnetic current $\bar{q}(\frac{1}{6} + \frac{1}{2}I_3)\gamma_\mu q$ where I_3 is the third isospin generator in both current equations. When coupling to a single photon, the isosinglet and isotriplet electromagnetic currents explicitly break the symmetry with the axial-vector current.

This symmetry breaking for a single photon-gluon coupling directly influences how a π^0 decays to two photons. The predicted decay amplitude for a $\pi^0 \rightarrow \gamma\gamma$, to leading order is:

$$A_{\gamma\gamma} = \frac{N_c (e_{em}^2)}{6(4\pi F_\pi)^2} \varepsilon_{\mu\nu\rho\sigma} (k^\mu k'^\nu \varepsilon^{*\rho} \varepsilon^{*\sigma}) \quad (2.1)$$

or

$$A_{\gamma\gamma} = \alpha N_c / (3\pi F_\pi) = 2.513 \cdot 10^{-2} \text{ GeV}^{-1}. \quad (2.2)$$

We define $N_c=3$ to be the number of colors in the Standard model, $F_\pi = 92.42 \pm \text{MeV}$ [5] is the pion decay constant, k and k' are the photon momentum, and ε and ε' are photon polarizations. This in turn gives is the decay width for the neutral pion

$$\Gamma(\pi^0 \rightarrow \gamma\gamma) = \frac{m_\pi^3 |A_{\gamma\gamma}|^2}{64\pi} = 7.725 \pm 0.044 \text{ eV}, \quad (2.3)$$

The uncertainty in this value is due to the 0.6 % uncertainty in F_π , and this value needs no additional correction in the chiral limit of $m_q=0$. This value for the decay width predicted by the anomaly is in good agreement with the Particle Data Group Average.

Corrections to this leading order decay width prediction arise from real world considerations. Quark masses are not zero, but rather $m_u \sim 4 \text{ MeV}$ and $m_d \sim 7 \text{ MeV}$. This gives rise to two corrections. The most important correction simply changes F_π to F_{π^+} and is a result of applying Alder and Bardeen's non-renormalization theorem to the anomaly [6 & 7]. A second correction due to non-vanishing quark mass is also the result of excited mesonic states such as the η and η' mixing into the saturated matrix element of the divergence of the axial current. This is a model dependent correction increasing the width by about 2% [8].

Spurred by the progress of the PrimEx collaboration, [1 & 2] have re-investigated the effects of the excited mesonic states on the π^0 decay width. Their new Chiral Perturbation Theory technique calculations are regarded as the most robust and definitive calculations to date. Both calculations report that the π^0 decay width is increased by roughly 4% to a value of

$$\Gamma(\pi^0 \rightarrow \gamma\gamma) = 8.10 eV \pm 1\% \quad [1] \text{ and} \quad (2.4)$$

$$\Gamma(\pi^0 \rightarrow \gamma\gamma) = 8.00 eV \pm 1\% . [2]. \quad (2.5)$$

This new theoretical calculation, a summary of our current experimental knowledge, and the projected PrimEx data point are presented in Figure 2.2.

The theoretical value is in good agreement with the PDG average, though no experiment listed in the world data has an uncertainty commensurate with the latest theory calculations. In view of the recent theoretical news, demonstrable poor world data, the availability of a precision measurement, and that the π^0 lifetime is a fundamental test of the chiral anomaly [3,4, & 5], a new experiment is needed to fill this gap in our knowledge of low energy QCD. This makes PrimEx possibly one of the most fundamental experiments one can perform with few GeV photons.

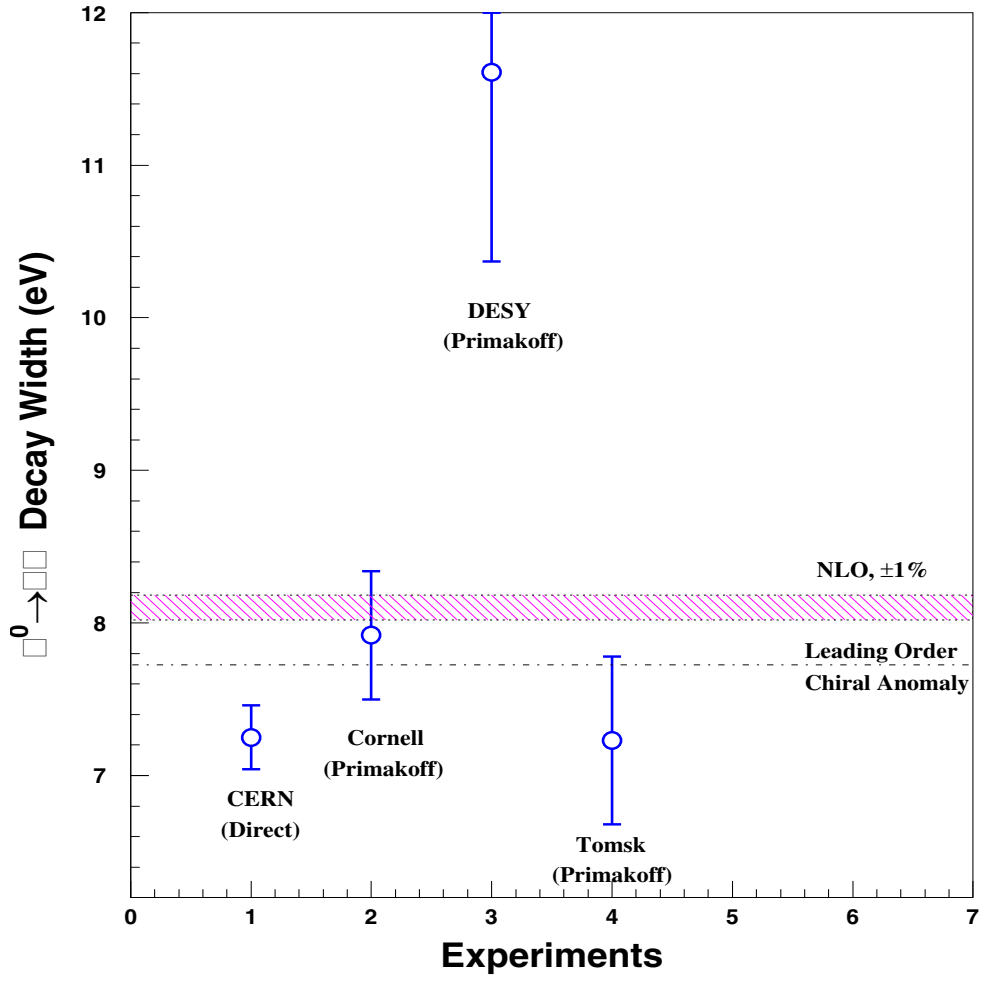


Figure 2.2: Summary of experimental and theoretical $\pi_0 \rightarrow \gamma\gamma$ decay width

CHAPTER 3

PREVIOUS EXPERIMENTS

3.1 Overview

Three general methods have been used to attempt to accurately measure the decay width of the π^0 . The “Direct Method”, $\gamma\gamma$ collisions, and the Primakoff effect have all been used with varying degrees of success. A brief overview of each method will be presented, as well as a close scrutiny of the state of the world data.

3.2 Direct Method

At CERN SPS (and CERN PS at 18 GeV [9]), researchers took advantage of the 450 GeV proton beam to make relativistic neutral pions that survived roughly a few 100 microns of flight length. The “Direct Method” (Figure 3.1) as it has come to be called, is conceptually the cleanest way to measure the π^0 decay width. Relativistically boosted pions will eventually decay in flight along the beam line and produce gammas.

Therefore, if one can measure the number of gammas as a function of distance, a measurement can be made of the π^0 width. At SPS, the proton beam hit a tungsten target that acted as the pion creation site. Another tungsten target was located anywhere from 5 to 250 microns downstream of the pion production target. This second target is where gammas from π^0 decays produced $e^+ e^-$ pairs. By varying the distance between targets and taking positron energy and position measurements, SPS was able to infer a neutral pion decay width of $7.34 \pm 0.22 \pm 0.11$ [10]. Error contributions are from uncertainty in the pion energy spectrum, which was taken to be the arithmetic mean of the π^+ and π^- . The SPS value is used in the PDG average, and is the most precise of all

π^0 measurements. It is, however, three standard deviations away from the newest theoretical calculations.

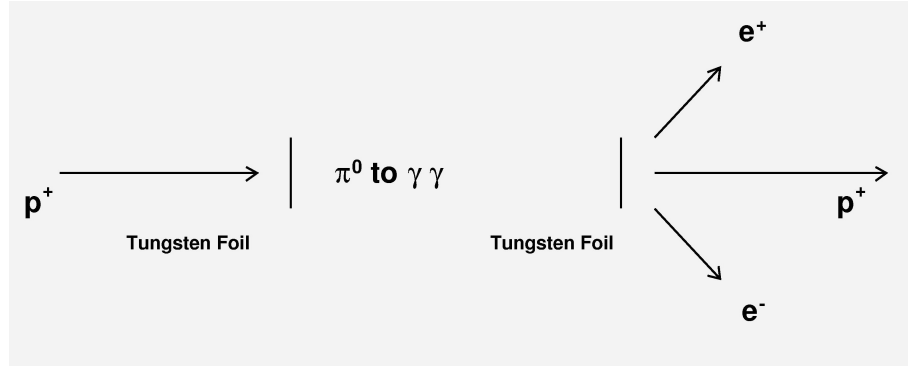


Figure 3.1: The Direct Method

3.3 $\gamma\gamma$ Collisions

In September of 1988, DESY published their results from $e^+ e^- \rightarrow \gamma\gamma e^+ e^-$ reactions (Figure 3.2) [11]. They reported decay widths for three resonances from 100 MeV to 3000 MeV. That collaboration used the Crystal Ball Detector, made of 672 NaI (sodium iodide) crystals with 93% solid angle coverage. They measured a neutral pion width of $7.7 \pm 0.5 \pm 0.5$ eV. This value is commensurate with the current world data, but is not included in the Particle Data Group average [5]. Contributions to the error include background cosmic rays, beam gas collisions, luminosity normalization, and detector efficiencies.

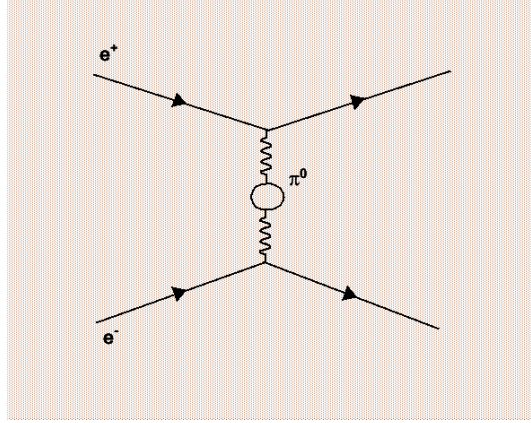


Figure 3.2: $\gamma\gamma$ Collisions

3.4 The Primakoff Effect

The Primakoff effect has been a very common but challenging method used to measure the neutral pion decay width. Primakoff first published his idea in 1951 [12], and in 1965 [13] and 1969 [14] a DESY collaboration published the results of two successful Primakoff π^0 decay width measurements. Two previous collaborations at MIT and Cal Tech had made neutral pion measurements, but lacked sufficient energy and/or angular resolution for a precise measurement [13]. The first DESY attempt at 0.95 GeV and 1 GeV yielded a value of 9.02 ± 0.95 eV for the neutral pion width. The second attempt measured a width of 11.7 ± 1.2 eV. Another Primakoff experiment at Tomsk measured 7.32 ± 0.5 eV at 1.1 GeV in 1969[15].

Other experiments have also attempted to measure the π^0 decay width [16, 17, 11, & 9]. It is worthwhile to explore one of these experiments in some detail. Employing the Primakoff technique, Browman *et al* measured the neutral pion width with 4.4 GeV and 6.6 GeV bremsstrahlung beam [16]. They measured a decay width of 8.02 ± 0.42 eV. However, the quoted uncertainty has been questioned by some [11 &

18]. Specifically, luminosity and detector efficiencies may be underestimated.

Browman *et al* also performed a Primakoff measurement of the η width using the same experimental set-up and technique that is not in agreement with world data [16].

3.5 Final remarks on previous experiments

There is no clear consensus on the neutral pion decay width. The Direct Method approach yielded the most precise measurement to date, yet it is three standard deviations away from the best theoretical value. Gamma-gamma collision data is available, but the inherent uncertainty is too large. Current Primakoff data points are also scattered from roughly 7.32 eV to 11.7 eV, and as stated there is no experiment with an uncertainty at the level of the theory calculations. In light of these experimental inadequacies, a new precision measurement of the π^0 decay width is required.

CHAPTER 4

THE EXPERIMENT

4.1 Overview

The photon tagging facility in Hall B of the Thomas Jefferson National Accelerator Facility can provide a photon beam of energies $(0.2 \rightarrow 0.95) \times (\text{electron beam energy})$. However, the collaboration is only interested in the higher energy photons at highest electron beam energy $(0.848 \rightarrow 0.954) \times (5.765 \text{ GeV})$. The absolute cross section for π^0 photoproduction from high Z nuclei at small angles can be measured using this facility. For unpolarized photons, the Primakoff differential cross section is [14]:

$$\frac{d^3\sigma_P}{d\Omega} = \Gamma_{\gamma\gamma} \frac{8\alpha Z^2}{m^3} \frac{\beta^3 E^4}{Q^4} |F_{e.m.}(Q)|^2 \sin^2 \theta_\pi, \quad (4.1)$$

where $\Gamma_{\gamma\gamma}$ is the pion decay width, Z is the atomic number, m , β , θ_π are the mass, velocity and production angle of the pion, E is the energy of the incident photon, Q is the momentum transfer to the nucleus, and $F_{e.m.}$ is the nuclear electromagnetic form factor. $F_{e.m.}$ is corrected for outgoing pion final state interactions.

As has been mentioned, there are competing processes at small angles ($\sim 0.20^\circ$) to the Primakoff cross section. The source of this competition is an interference term between the nuclear coherent and Primakoff processes. The total cross section is:

$$\frac{d^3\sigma}{d\Omega_\pi} = \frac{d\sigma_P}{d\Omega} + \frac{d\sigma_C}{d\Omega} + \frac{d\sigma_I}{d\Omega} + 2\sqrt{\frac{d\sigma_P}{d\Omega} \cdot \frac{d\sigma_C}{d\Omega}} \cos(\phi_1 + \phi_2). \quad (4.2)$$

The nuclear coherent cross section is given by [19]:

$$\frac{d\sigma_c}{d\Omega} = C \cdot A^2 |F_N(Q)|^2 \sin^2 \theta_\pi, \quad (4.3)$$

and the incoherent cross section is [20]:

$$\frac{d\sigma_I}{d\Omega} = \xi A(1 - G(Q)) \frac{d\sigma_H}{d\Omega}, \quad (4.4)$$

where A is the nucleon number, $C \sin^2 \theta_\pi$ is the square of the isospin and spin independent part of neutral meson photoproduction amplitude for a single nucleon, $|F_N(Q)|$ is the form factor for the distribution of nuclear matter (corrected for pion final state interactions), ξ is the absorption factor for incoherently produced pions, $1 - G(Q)$ is a Pauli exclusion principle effect that reduces the cross section at small momentum transfer, and $\frac{d\sigma_H}{d\Omega}$ is the cross section for π^0 photoproduction on a single nucleon. ϕ_1 is the phase shift between the Primakoff and nuclear coherent amplitudes and the ϕ_2 is the phase shift of the outgoing pion due to final state interactions.

Kinematic considerations allow the data analysis to cleanly separate out the Primakoff cross section. The cross section has a maximum at $\theta_\pi \sim m_\pi^2 / (2E_\pi^2)$ which falls rapidly to zero at larger angles. As shown in equation 5 the Primakoff cross section has a strong energy dependence that goes as E^4 . Figure 4.1 demonstrates the strong small angle dependence of Primakoff pion photoproduction. The amplitudes are normalized to data from [16] and distortion effects are included and expected to vary little with energy [14]. Additionally, it is apparent from Figure 6 that the nuclear coherent and cross term contributions to the cross section add some uncertainty to our final result. The PrimEx collaboration has taken data at larger angles (up to 4.0°) to measure the nuclear coherent and incoherent cross section so their effects at smaller angles can be

understood and subtracted, leaving only the Primakoff contribution.

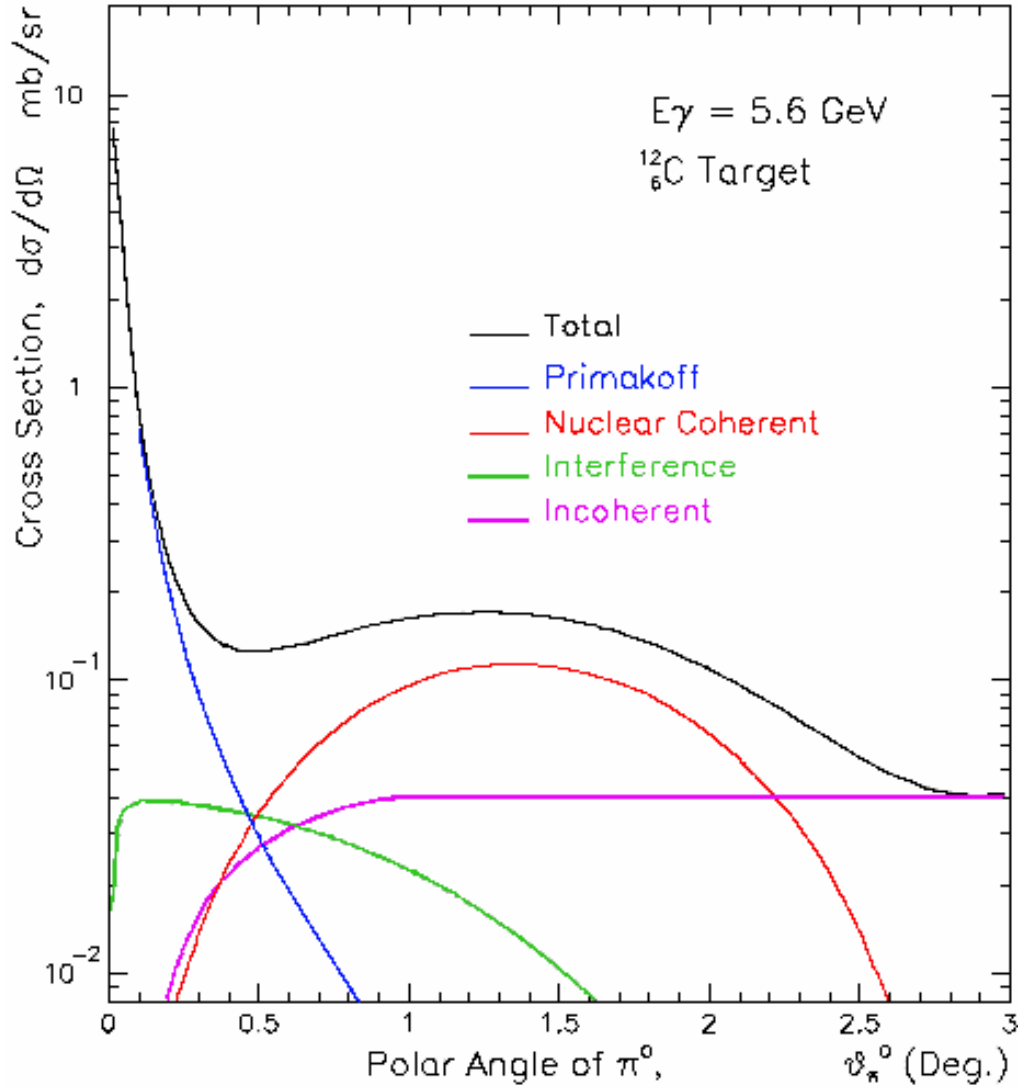


Figure 4.1: Total neutral pion cross section for ^{12}C

This experiment, like many other Primakoff experiments, must concern itself with understanding and minimizing contributions from other neutral vector and scalar mesons. In particular, the ρ , ω and ϕ would be the biggest contributors of background neutral pion events. However, the highly segmented HyCal's resolution and the photon Tagger in Hall B provide for much tighter kinematic constraints than any previous Primakoff experiment. GEANT simulations have given the collaboration confidence

that any background meson events, if not explicitly excluded by geometric and kinematic constraints, can be suppressed sufficiently to make the error budget. Other background events from accidentals, correlated $\gamma\gamma$ background events, and beamline background are well understood, can be modeled in simulation, and/or have been measured in empty target runs during the experiment. Strong force components do make a contribution to the nuclear coherent cross section, and π^0 's created in the nucleus do have a large probability to interact in the nucleus. Corrections for these final state interactions are understood and implemented in simulation studies. Finally, the collaboration intends on extracting a π^0 decay width from ^{12}C and to measure Compton cross sections as checks on systematic uncertainties. The Compton results will not be presented here.

A large driving force behind doing a Primakoff experiment at TJNAF is the low quoted error the PrimEx collaboration feels it can achieve. As has been stated, an uncertainty of 1.5% is the goal of PrimEx. An uncertainty this small is an ambitious proposal, and currently the collaboration is working towards these projected uncertainties. The error budget below details the target precision of the largest contribution to the experimental error bars.

Table 1.1: Summary of PrimEx projected experimental error

Statistical	0.40%
Target thickness	0.70%
Photon flux	1.00%
π^0 detector acceptance and misalignment	0.40%
Background subtraction	0.20%
Beam energy	0.10%
Distorted form factor calibration errors	0.40%
<i>Total error (added in quadrature):</i>	1.40%

4.2 Experimental Setup

To extract a high precision radiative width measurement from measured cross sections, the experimental requirements and set-up must be explained in sufficient detail.

- 1.) Well understood nuclear targets.
 - a. ^{12}C Carbon, $\rho\tau$ (density \times thickness) known to 0.04%.
- 2.) Precise control of electron and photon beam and photon flux (Photon Tagger)
 - a. Beam position monitoring for both electron and photon beam
 - b. Wire harp scans along beamline to determine photon and electron profiles
 - i. Additional Scintillating Fiber Monitor behind calorimeter (HyCal)
 - c. Number of photons on target, i.e. luminosity .
 - i. “Absolute flux monitoring”.
 1. Done at low beam currents (Total Absorption Counter)
 2. Correct for component Tagger detector inefficiencies at π^0 production currents
 - ii. Relative flux monitoring to ensure stable beam/luminosity
 1. At physics (high) beam current (Pair Spectrometer)
- 3.) π^0 yields as a function of production angle must be extracted.
 - a. Neutral pion detector with good energy and angular resolution (HyCal).
 - b. Charged particle veto
- 4.) Trigger design and high speed data acquisition system

- a. Total energy in HyCal sum coincidence with Photon Tagger
- b. Data Acquisition electronics and set-up
- c. Event rate for various detectors

From this information normalized yields can be calculated, as well as cross sections once efficiency corrections are extracted from simulation. Specifically, normalized yields are given by

$$\frac{\pi^0 \text{yield}(\theta_{\pi^0})}{\text{NumberOfPhotons} \times \text{NumberOf}^{12}\text{Catoms}}. \quad (4.5)$$

Efficiency corrected cross sections are given by:

$$\frac{\pi^0 \text{yield}(\theta_{\pi^0}) \times \varepsilon(\theta_{\pi^0})}{\text{NumberOfPhotons} \times \text{NumberOf}^{12}\text{Catoms}}, \quad (4.6)$$

where ε is the average efficiency for that bin of π^0 production angle.

The experimental set-up (Figure 4.2) will be discussed and explained in some detail. The published proceedings on the performance of many components in the experiment are sparse to no-existent. The description of the experimental set-up will follow the above outline in an approximate trajectory along the beamline.

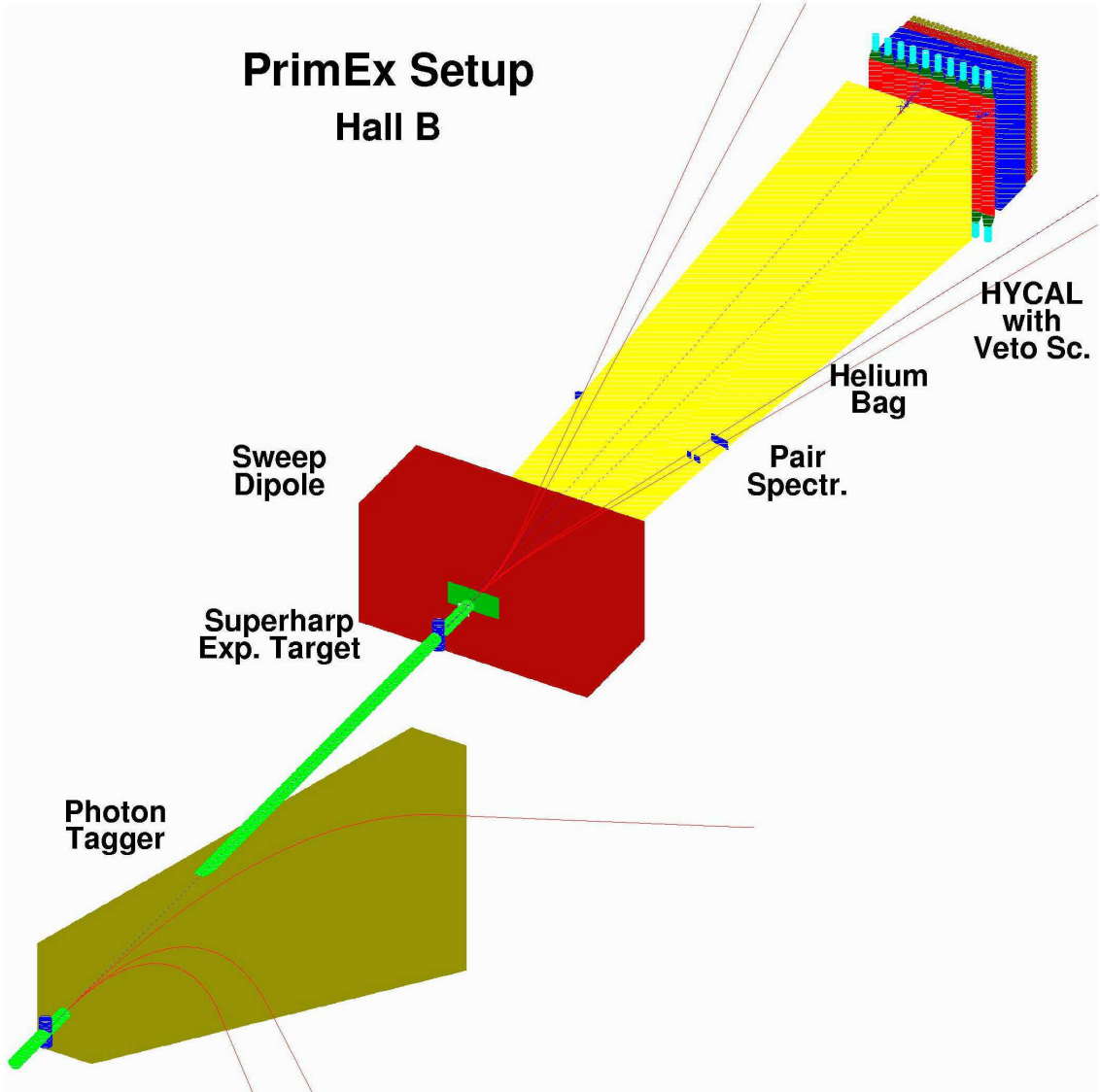


Figure 4.2: The conceptual PrimEx Setup in Hall B.

4.2.1 PrimEx Experimental Targets

The collaboration decided to use three targets with the ground state $J_p = 0^+$. Also, the charge densities of these isotopes are well known from model-independent electron scattering data. The ^{12}C is a 5% radiation length target with well known thickness and density. The required uncertainty in the thickness measurement is 0.7% or better. The collaboration has measured the ρt of ^{120}Sn , ^{208}Pb , and ^{12}C , but only data

and results from ^{12}C will be presented. Interested readers may reference [21] for the details on the ρt measurement of ^{120}Sn , ^{208}Pb . The value ' ρt ' is the density multiplied by the target thickness, a measure of nuclei/cm². The ^{12}C target is of macroscopic thickness and was measured with a micrometer to the required precision. Density variations in the ^{12}C are insignificant.

4.2.2 Carbon Target Thickness Measurement

The PrimEx ^{12}C target (Figure 4.3) is made of Highly Ordered/Oriented Pyrolytic Graphite (HOPG). HOPG is made via Chemical Vapor Deposition (CVD) at temperatures of ~ 3200 K. This fabrication method ensures a highly chemically pure, crystalline structure by depositing atomic layers of ^{12}C (Figure 4.4). This also produces a low porosity material of highly uniform density. Compare HOPG's 1% porosity to 10% porosity for normal graphite. A block of 1 in \times 1 in (area normal to the beam) \times 377 mils (5% radiation length) was cut from a piece of HOPG provided by Stanford Linear Accelerator. Destructive elemental and chemical analyses conducted by independent facilities determined the ^{12}C purity at 99.63% (Table 4.1).

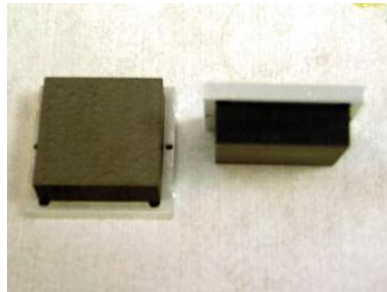


Figure 4.3: The HOPG target placed in the support and mounting frame

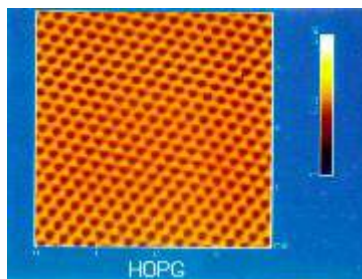


Figure 4.4: Electron micrograph scan of HOPG surface

Table 4.2: HOPG Elemental Analysis

Element	Abundance	Error (PIXE)
Carbon	99.63%	
Hydrogen	< 0.10%	
Nitrogen	< 0.05%	
Oxygen	0.19%	
Aluminum	0.00611%	0.00263%
Silicon	0.00568%	0.00144%
Chlorine	0.00285%	0.00067%
Calcium	0.00302%	0.00054%
Titanium	0.00037%	0.00017%
Vanadium	0.00079%	0.00011%
Chromium	0.00020%	0.00005%
Iron	0.00105%	0.00006%
Copper	0.00025%	0.00004%
Zinc	0.00033%	0.00005%

Water displacement measurements (Figure 4.5) were sufficient to determine the HOPG density due to its guaranteed homogeneity. In addition to water displacement density measurements, micrometer measurements were used to make a determination of ρ_t . A thickness profile of each target was created with a 20 site measurements. The size of the micrometer tip was approximately 2 mm, a very comparable size to the photon beam at Jefferson Lab (as shall be shown).

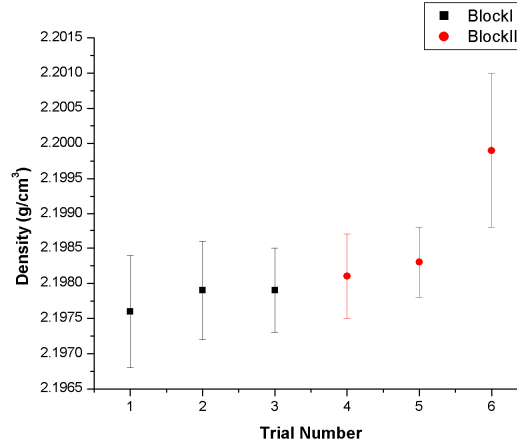


Figure 4.5: Water immersion density measurements

Additionally, custom made masks/jigs were used to assure the reliability and reproducibility of target thickness measurements (Figure 4.6). Variations in the thickness of each target were less than 0.04% (0.3 mils) for the 5% X_o ¹²C target. The micrometer claimed a precision of 0.05 mils. The average measured density via water immersion for the HOPG was $2.1983 \pm 0.0002 \text{ g/cm}^3$, well within the manufacturer specification of $2.200 \pm 0.002 \text{ g/cm}^3$. This results in a pt of $(1.0657 \pm 0.0001) \times 10^{23} \text{ nuclei/cm}^2$.

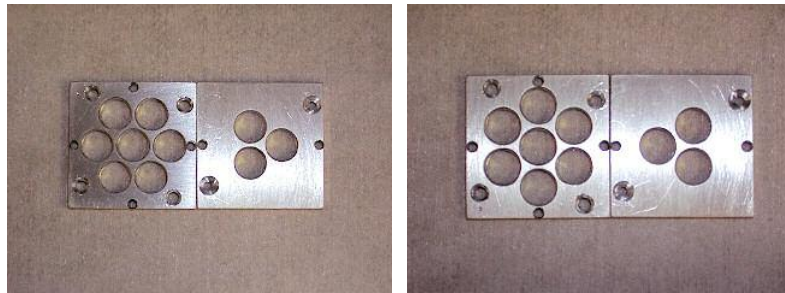


Figure 4.6: Target Masks for ¹²C

Corrections due to incident photon beam absorption and the established impurities yield a final “effective pt” of $1.046 \times 10^{23} \pm 0.04\% \text{ nuclei/cm}^2$, surpassing error budget constraints for target thickness uncertainty.

4.2.3 The TJNAF Hall B Photon Tagger

The Thomas Jefferson National Accelerator Facility is capable of delivering an electron beam of nearly 6 GeV. This electron beam can be steered into Hall B's post-bremmstrahlung electron momentum analyzer, commonly called the Photon Tagger. Since the Primakoff cross section goes as E_γ^4 , the collaboration received the highest energy available at TJNAF in the Fall of 2004 (5.765 GeV). The photon energy spectrum sampled was 5.50 GeV to 4.89 GeV.

The tagged photon beam is created by placing a thin ($X_0 \sim 10e-3$), high atomic Z radiator in the electron beam line, causing beam electrons to bremmstrahlung. The beam electrons produce bremmstrahlung on a thin radiator, and the electron beam is subsequently bent by the Tagger magnet. Most beam electrons do not interact with the radiator and are bent into the beam dump. Those electrons that did produce bremmstrahlung are bent into a set of detectors that momentum analyze the electrons and determine timing and energy information. Downstream events in coincidence with a Tagger event are now highly correlated and the energy of the correlated photon known to within 0.1 percent.

The Photon Tagger (Figure 4.7) consists of 384 "E Counters" which provide the energy information and 61 "T Counters" that provide timing information. The collaboration used only the highest energy E Counters (1-56) and T Counters (1-11) to sample the photon beam since Primakoff kinematics are strongly peaked at higher energy. The T Counters have approximately a 10% overlap with adjacent Counters, resulting in $2\tau-1$ "*T Channel*" bins where ' τ ' is the number of T Counters active. Occupancies in the reconstructed T Channel bins are highly asymmetric. Overlap

channels have much lower statistics than non-overlap Channels. While complicated, this overlapping design ensures no gaps in acceptance. E Counters have roughly a 33% overlap with adjacent Counters. This results in approximately equivalent occupancies for the $2\epsilon-1$ “*E Channel*” bins (ϵ is the number of active E Counters), doubles the effective resolution, and leaves no acceptance gaps. PrimEx used only the top 11 *T Channels* and 120 *E Channels* for π^0 running. For further details on Hall B Photon Tagger, please reference [22].

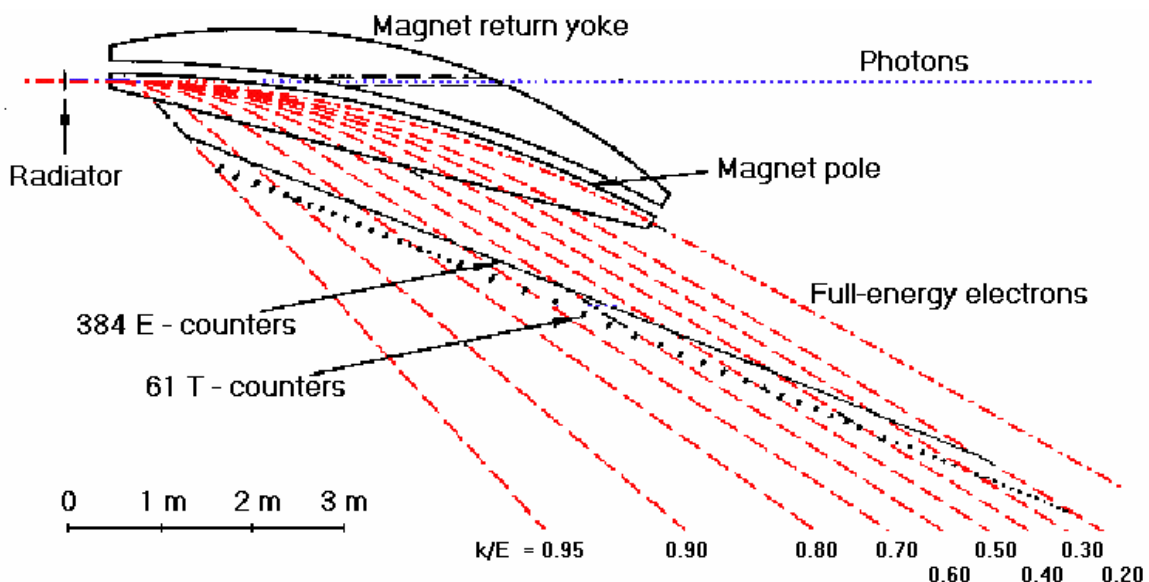


Figure 4.7: The Hall B Photon Tagger

The Hall B Photon Tagger is perhaps the single largest advantage that the PrimEx collaboration enjoys over previous Primakoff experiments [13, 14, 15,& 16]. For example, in Browman *et al.* [17] the 0.5% uncertainty in the untagged photon energy contributed a 3% uncertainty to the decay width [16]. Energy and timing information are crucial to the collaboration’s endeavor.

However, quality of the beam is also critical. While the specifics of beam tune and steering are beyond the scope of this dissertation, knowledge of electron beam

energy, position, profile, and photon position and profile are vital. These data can be accessed by looking at real-time electron and photon beam current and/or position monitoring. If the electron beam is mis-steered or has a large halo (beam spot profile) then reconstructed 4 vectors from HyCal will suffer unknown systematics and/or the photon beam may hit non-physics target material in the beam line, polluting data.

Beam Position Monitors (BPM's) for the electron beam and Wire Harp Scans (WHS's) for both the electron beam and photon beam demonstrate that a well placed and well shaped beam profile were routinely possible. BPM's are a 4-wire antenna array of open ended thin wire striplines tuned to the RF of the accelerator, and are non-destructive, real-time electron beam current and position monitors that give continuous information during active beam conditions. BPM's are located at strategic locations along the accelerator and Hall B enclosure and thus provide good knowledge of the electron beam current and position up to the bremsstrahlung target in the Tagger. WHS's pass high atomic Z wire through either the electron or photon beams. Downstream scalars record events rates as the wires sweep through the beam so that a profile of the beam can be constructed.

4.2.4 Scintillating Fiber (SciFi) Photon Beam Monitor

The Scintillating Fiber (SciFi) detector, placed just behind HyCal at nominal beam path, has also helped to understand and correct any systematic shifts in the photon beam position and profile. Coupled with photon WHS at the physics target and precise survey data, the Sci-fi detector completely defines the photon beam path from target to HyCal. As its name implies, the Sci-Fi is constructed of 2 nearly identical planes of scintillating plastic fibers 1mm in diameter (Figure 4.8 and 4.9). There are 61 channels

in the 'x' plane and 62 channels in the 'y' plane, and each fiber is clad in a light reflective sheath bringing the total individual fiber dimensions to 2mm OD x 13 mm. Both detector planes are normal to the photon beam, but one plane is rotated 90° with respect to the other in order to construct a 2 dimensional beam profile. The scintillating fibers in each plane are optically coupled to four 16-channel multi-plexing R5600-M16 Hamamatsu photomultiplier tubes. A compact electronics module amplified, discriminated, and converted the ADC signals to ECL time over threshold outputs. The ECL signals were then collected via an EPICS interface during active beam condition at 30 second intervals. This is wealth of in-situ photon beam position and profile information.

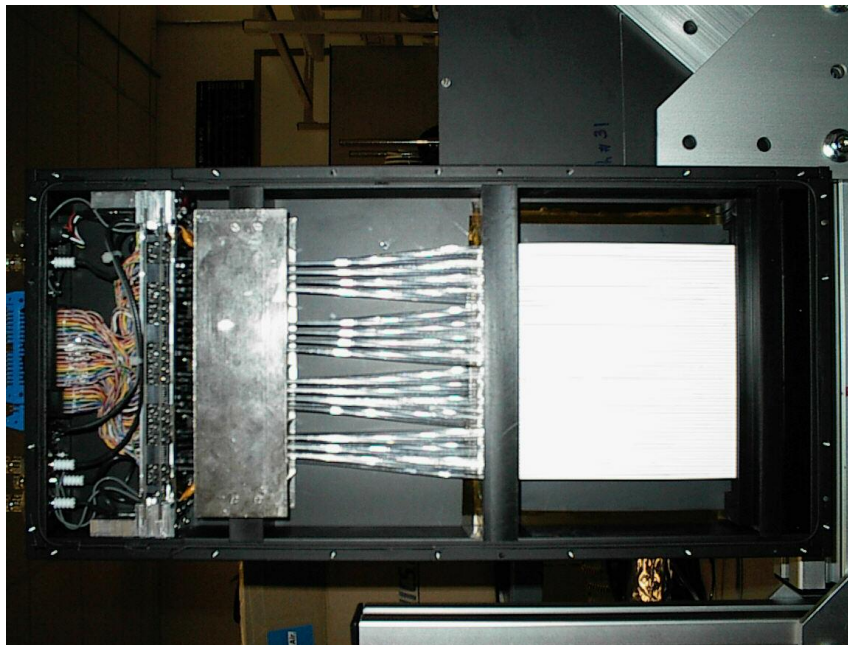


Figure 4.8: The Sci-Fi monitor PMT's and electronics (left), light guides (center), and fibers (right side)

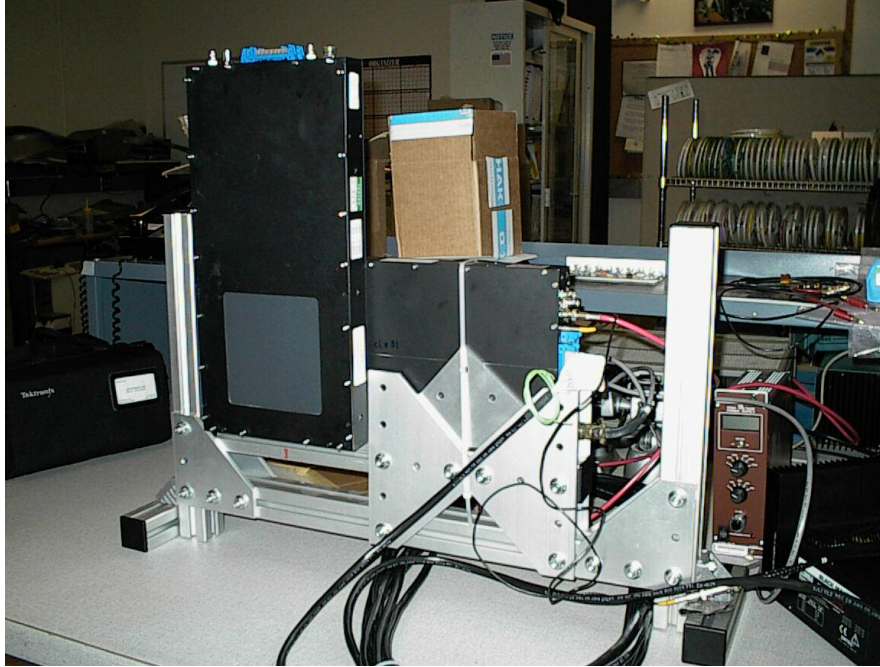


Figure 4.9: The Sci-Fi monitor, both planes assembled

4.2.5 Determining electron and photon beam characteristics and trajectory

A great deal of work has gone into understanding beam stability, mean position, divergence/halo, and incident angle at HyCal. All beam parameter values presented are “absolute” in the sense that each beamline piece of equipment or detector is placed in Hall B and its position and orientation measured with respect to the idealized beam line. All beam monitors are placed in and the positions measured against the same ideal co-ordinate system, thus is no need to discuss relative measurements between arbitrary detector co-ordinate systems.

By utilizing “Double Arm Compton” data runs taken throughout the entire run time, calibration ‘x’ and ‘y’ beam position offsets could be determined (Figure 4.10). These “Double Arm Compton” events are two cluster events where both the Compton scattered photon and electron are detected in HyCal, and are kinematically constrained

to be symmetric about the beam axis. By connecting the electron and photon cluster positions across the face of HyCal, the offset of the nominal HyCal coordinate system origin with respect to the incoming photon beam can be determined. The “Single Arm Compton” signal is present during π^0 running, as the Pair Spectrometer magnet sweeps away the electron, but the Compton photon can still be detected in HyCal. “Double Arm Compton” provides one method of accessing photon beam position at HyCal.

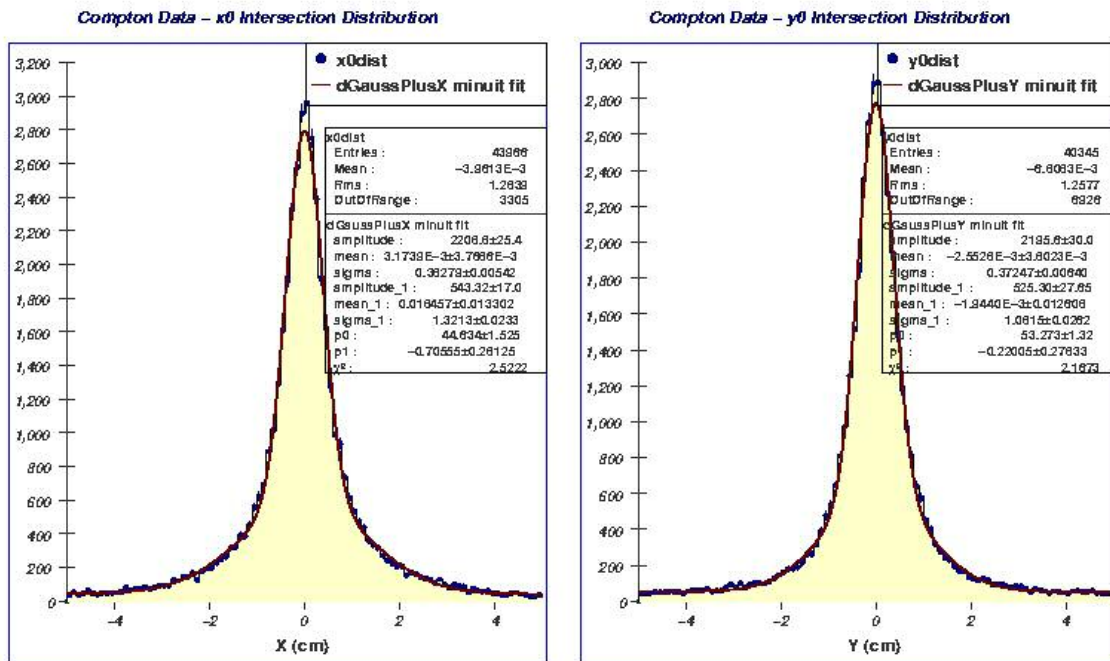


Figure 4.10: Calibrated beam position from “Double Arm Compton” data

Electron beam BPM read-out data radiator (BPM 2C24A) provides absolute information position of the electron just before the Tagger bremsstrahlung. Beam ‘x’ and ‘y’ position can be extracted on a run-by-run basis (Figure 4.11). Sci-fi monitor beam position and beam spot size can also be extracted on a run by run basis (Figure 4.12). With accurate survey data, beam position offsets can be determined for the Sci-Fi detector as well. Figure 4.13 summarizes BPM data, “Double Arm Compton” measured beam position at HyCal, and Sci-Fi survey measured beam position. The

non-zero (survey corrected) Sci-Fi beam position in Figure 4.14 suggests that there is a small trajectory off the nominal photon beam path (Figure 4.15). Verification of and

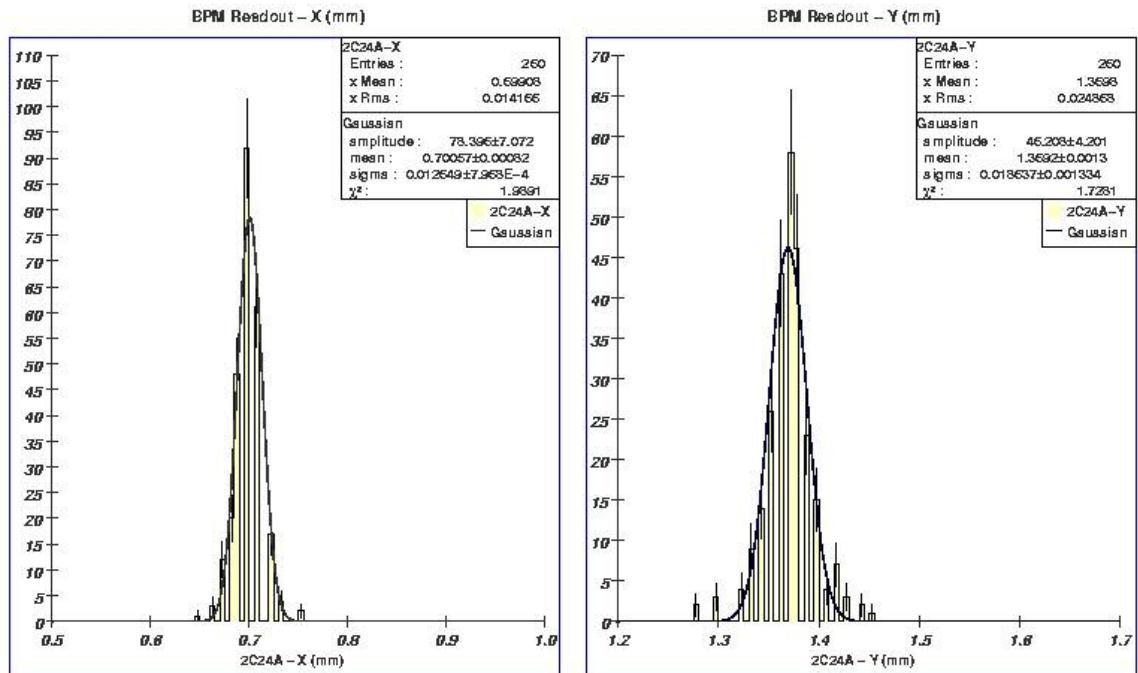


Figure 4.11: BPM 2C24A electron beam position data

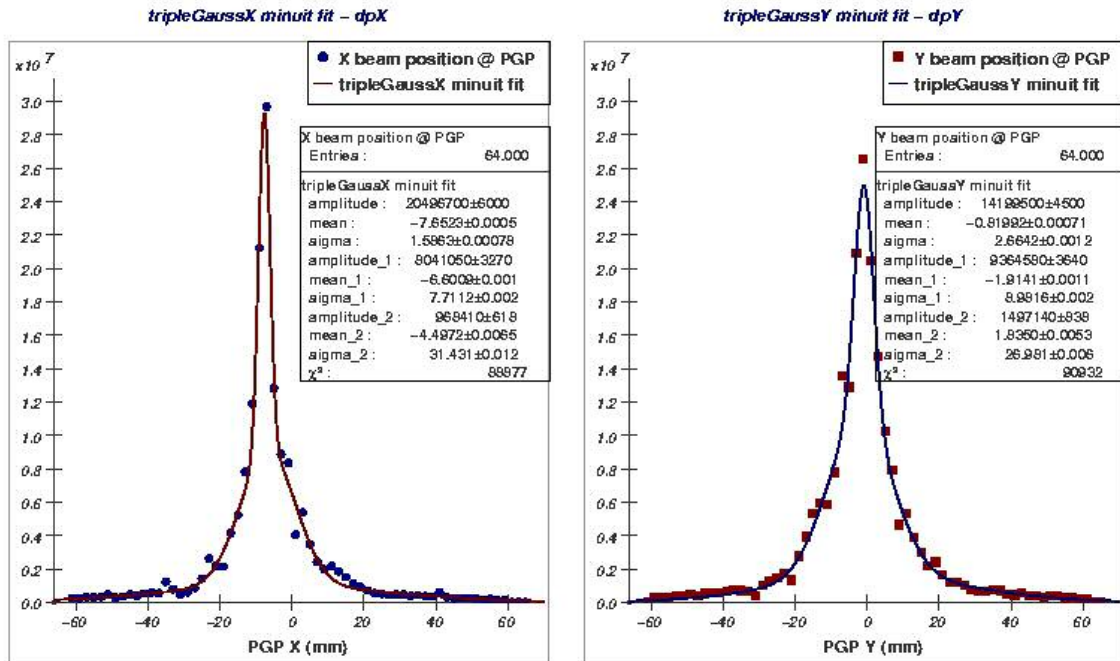


Figure 4.12: Non-calibrated Sci-Fi monitor photon beam position

quantification of the trajectory is currently an active area of investigation in the collaboration. Once any non-nominal trajectory is understood, it can modeled in simulation.

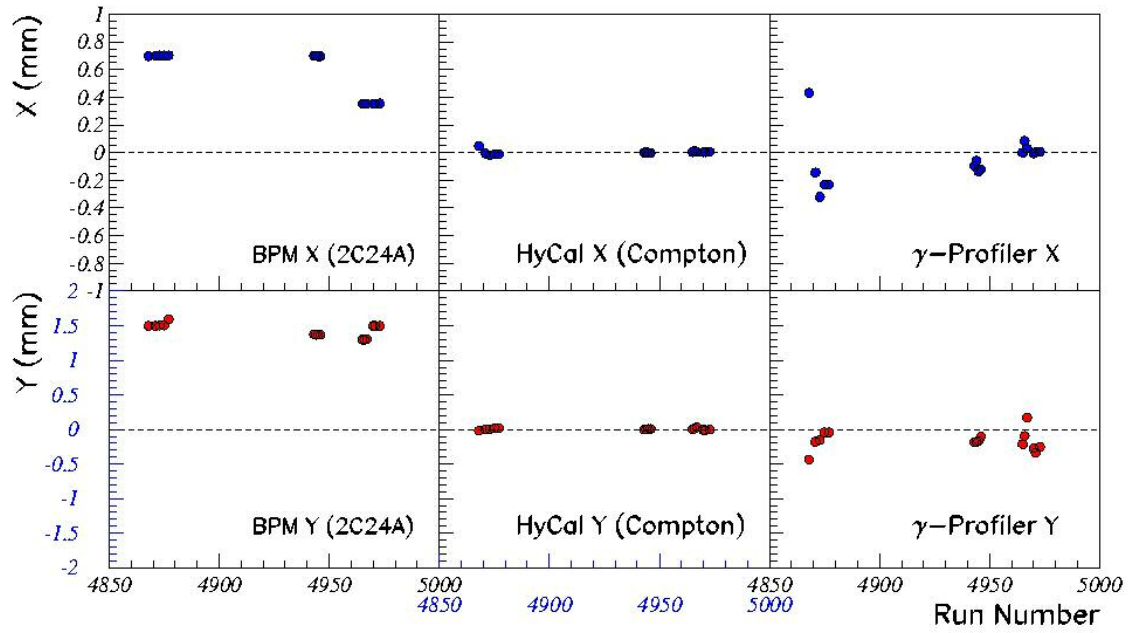


Figure 4.13: Summary of Sci-Fi, HyCal, “Double Compton” and BPM data

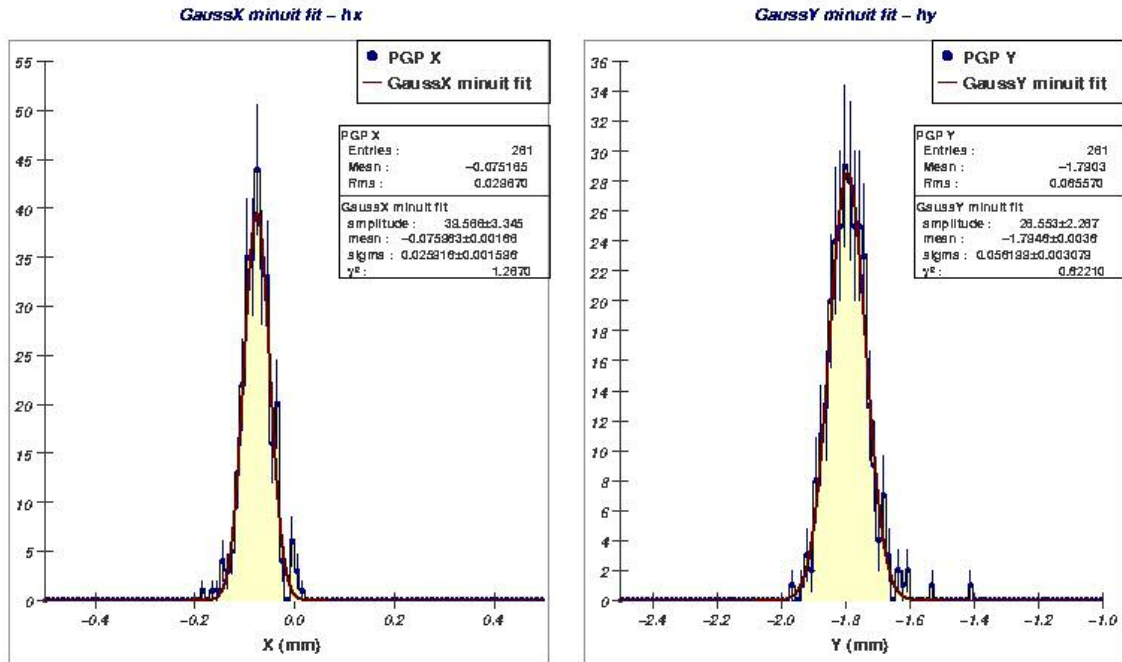


Figure 4.14: Survey calibrated Sci-Fi monitor photon beam position

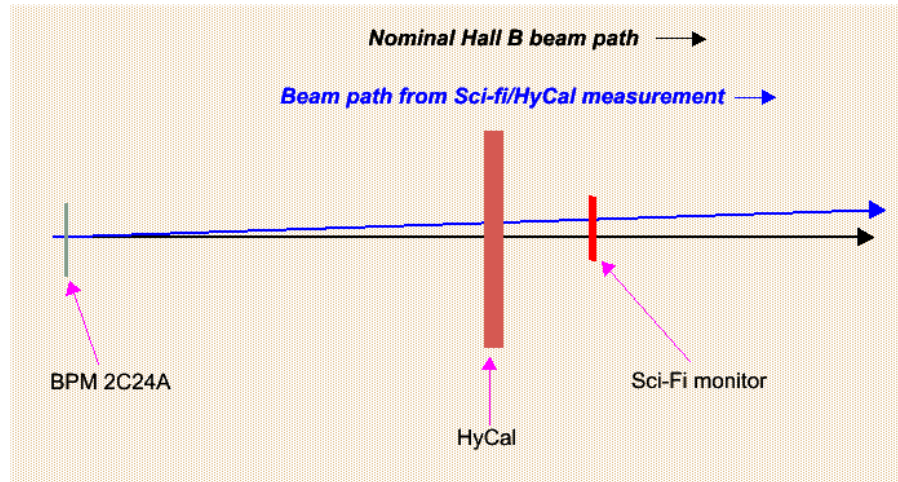


Figure 4.15: Graphical explanation of beam path parameterization.

It should be noted that the beam stability in the ‘x’ direction was very good throughout the entire run time, with position spectrums at HyCal centered to ~ 0.01 mm and a width of ~ 0.025 mm as determined by the Double Compton study. However, the ‘y’ coordinate at HyCal was not a well centered at the face of HyCal and also suffers a

jump in the Double Compton ‘y’ position (Figure 4.16 and 4.17). The average ‘y’ beam position was $\sim 1.4\text{mm}$ with $\sim 0.1\text{mm}$ width. The shift in beam position center was from $\sim 1.4\text{mm}$ to $\sim 1.2\text{mm}$ about mid-way through the total run time. The 2C24A BPM did not show any shift in beam position throughout the entire run time. The source of this shift is unknown, but a slight alteration of the electron beam tune upstream of the Tagger could easily produce this effect. However, this effect has been quantified and calibrations exist to correct it.

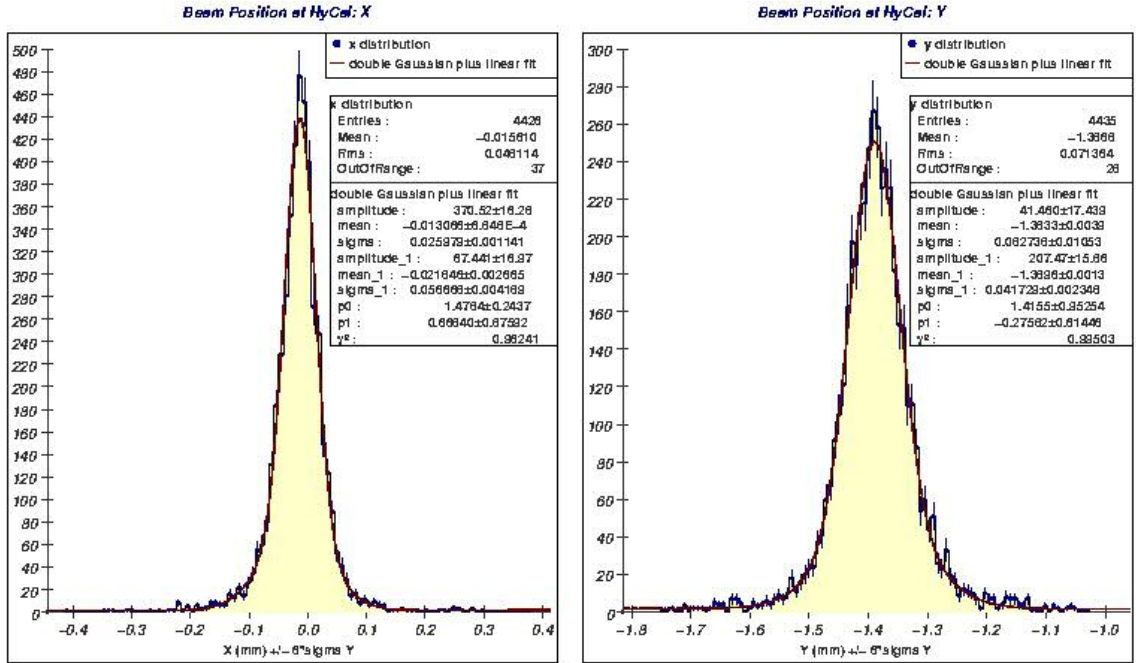


Figure 4.16: Double Compton extracted beam position for roughly 1st half of data

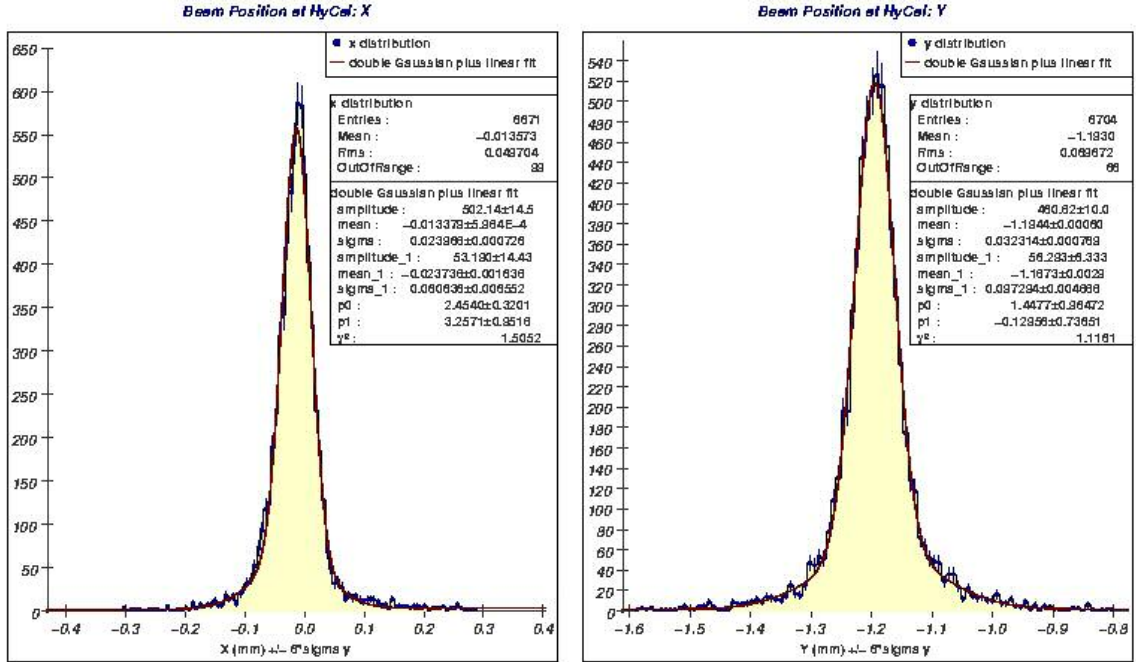


Figure 4.17: Double Compton extracted beam position for 2nd half of data

The electron beam just before the tagger is also well defined (Figure 4.18). It can be demonstrated that the photon beam just past the Tagger radiator and at the physics target is of acceptable quality. Several photon WHS's were conducted throughout data collection. Figure 4.19 is an example of a typical photon WHS near the Tagger. The collaboration also had the ability to perform photon WHS's at the physics target. The position of high Z wires in the target Harp were precisely known (within 0.1mm) both with respect to the ideal beam line and the physics target. Simple geometry and arithmetic ensured that the photon beam was interacting with a flat, uniform pt area of the physics target far away from non-physics target material. Figure 4.20 is an example of a typical physics target WHS. Information regarding photon beam divergence can be determined from this data and Hall survey data for implementation into simulation. While the origins of the co-ordinate systems in Figure 4.18, 4.19, and 4.20 are arbitrary, they share a common scale. It is enough to confirm

that the electron and photon beams maintain a consistent profile and trajectory without resorting to an absolute co-ordinate system for these WHS's.

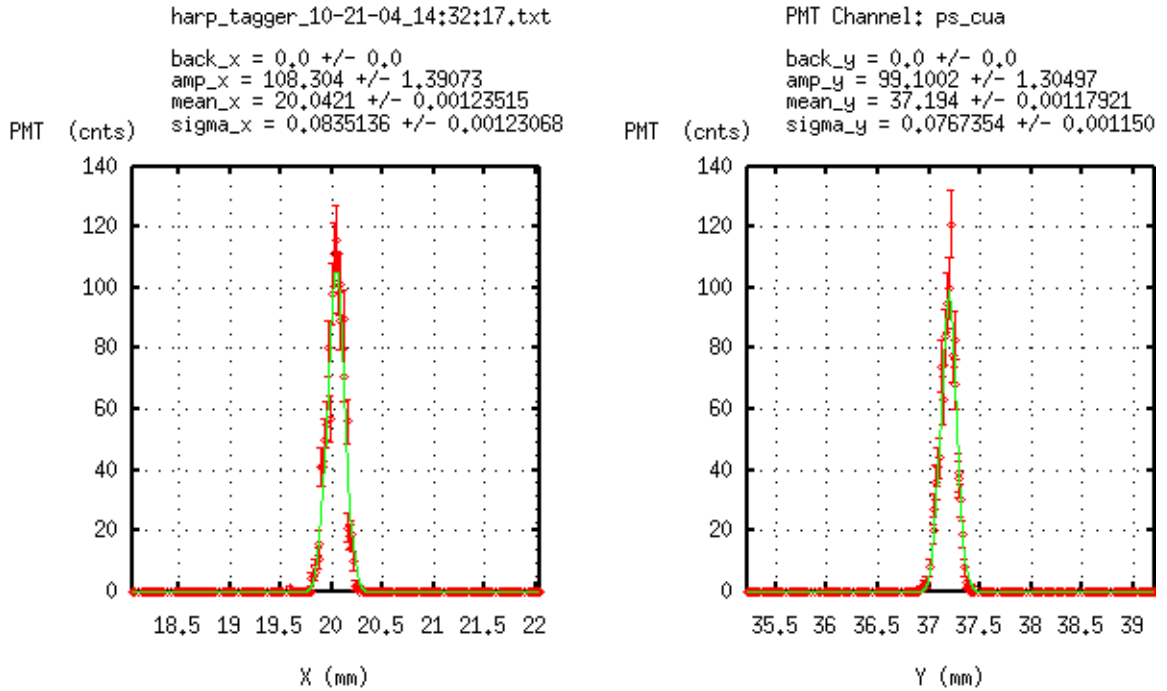


Figure 4.18: Sample Tagger Electron harp scan

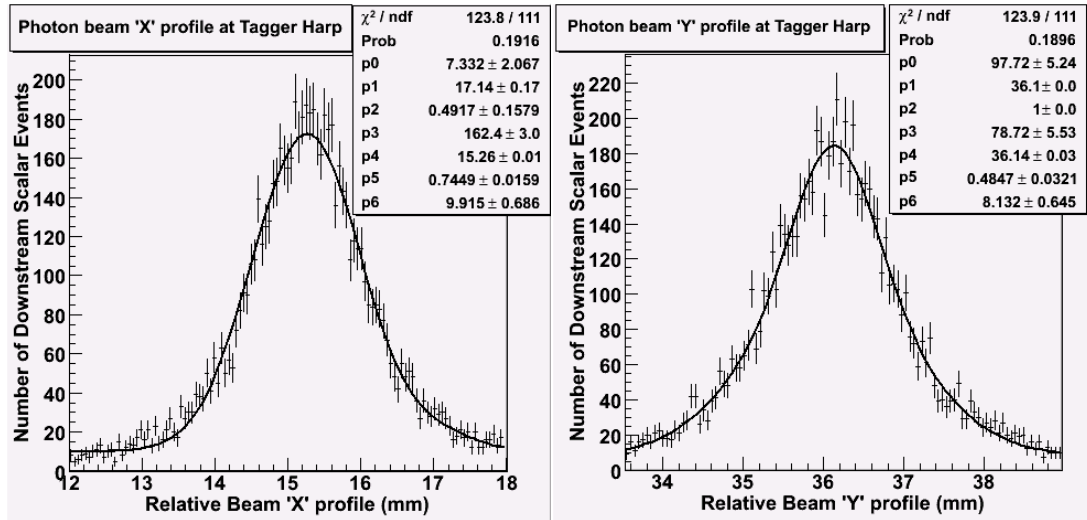


Figure 4.19: A Tagger Photon harp scan, before physics target, just after Tagger radiator. Parameters p0/p3, p1/p4, and p2/p5 are the amplitude, mean, and sigma of a gaussian, respectively.

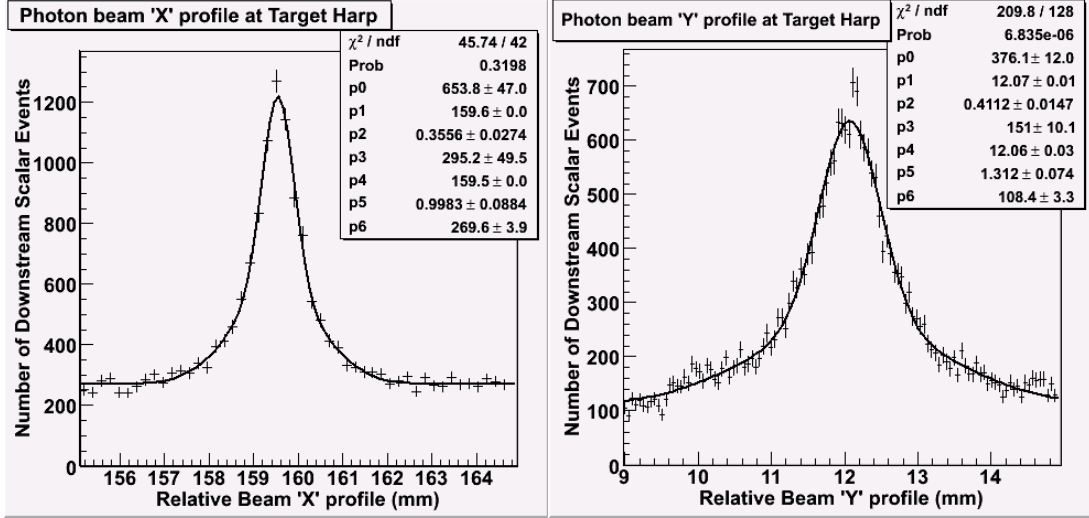


Figure 4.20: Sample Physics Target Photon harp scan. Parameters p0/p3, p1/p4, and p2/p5 are the amplitude, mean, and sigma of a gaussian, respectively.

The end result is that the collaboration feels confident it has high precision knowledge of the electron, and more importantly, photon beam trajectories. A stable photon beam trajectory has been verified, calibration constants/corrections evaluated for beam position on HyCal, photon and electron beam profiles at Tagger and physics targets are known and within acceptable values, and photon beam incident angles at HyCal are small (~ 0.1 mrad).

Information on the electron and photon beam, as well as the use of the Photon Tagger provided to the collaboration a source of photons with precisely determined time, energy, and trajectory information correlated with events downstream. Any electron and photon beam systematic uncertainties were minimized during data collected and offline investigation of smaller beam effects can be measured and corrected with standard or PrimEx installed beamline equipment. The Tagger is also used to count the number of tagged photons thrown downstream. This information is used in conjunction with offline Total Absorption Counter and Pair Spectrometer

analyses to determine the experimental luminosity or, more precisely, relative photon flux.

4.2.6 The Total Absorption Counter and Absolute Photon Flux

A Total Absorption Counter (TAC) constructed of lead glass (20x20x40 cm³) and attached to a 5 in diameter Hamamatsu Photo-Multiplier Tube (PMT), was used to provide data on the T and E Channel tagging ratios. The “absolute tagging ratio” is defined as the ratio of Tagger events (in a specific E or T Channel) to TAC events, where it is assumed that the TAC is 100% efficient. At low beam currents, this is a reasonable assumption because of the small number of multiple Tagger events and the modest event rate in the TAC. Absolute photon flux measurements could not be done at production currents of ~ 100 nA. Lower (~ 50 to 100 pA) beam currents were used to prevent radiation damage to the TAC and to ensure small Tagger photon tagging multiplicity (nearly always one photon per trigger in Tagger) and only one photon in the TAC (~ 100 efficiency). Tagging ratios are defined as

$$TaggingRatio_{Channel} = \frac{N_{\gamma}^{tagged}(calibration)}{N_e(calibration)}, \quad (4.6)$$

for a given E or T Channel. Ratios of less than unity represent the maximal efficiency of that E or T Channel. This effectively introduces and determines energy dependent corrections to the photon flux measurement during high current physics data collection. Specifically, this is defined as

$$N_{\gamma}^{tagged}(\pi^0 production)_{Channel} = N_e(\pi^0 production)_{Channel} \times \frac{N_{\gamma}^{tagged}(calibration)}{N_e(calibration)} \quad (4.7)$$

or,

$$N_{\gamma}^{tagged}(\pi^0 \text{ production})_{Channel} = N_e(\pi^0 \text{ production})_{Channel} \times TaggingRatio_{Channel} . \quad (4.8)$$

Figure 4.21 shows the tagging ratio over the entire physical tagger measured during a sample TAC run. Lost photons are due to normal Hall B background, Møller events in the bremsstrahlung radiator or the tagger, and cases where a bremsstrahlung photon is produced but is absorbed before reaching the TAC.

Photon flux can therefore be determined by counting the number of post bremsstrahlung in each E or T Channel:

$$N_{\gamma}^{tagged}(\pi^0 \text{ production}) = N_e(\pi^0 \text{ production}) \times \frac{N_{\gamma}^{tagged}(calibration)}{N_e(calibration)} . \quad (4.9)$$

Extracted, tagged π^0 yields are then defined as:

$$TaggedYield = \frac{d\sigma}{d\Omega} \times t \times \Delta\Omega \times N_e(\pi^0 \text{ production}) \times \frac{N_{\gamma}^{tagged}(calibration)}{N_e(calibration)} . \quad (4.10)$$

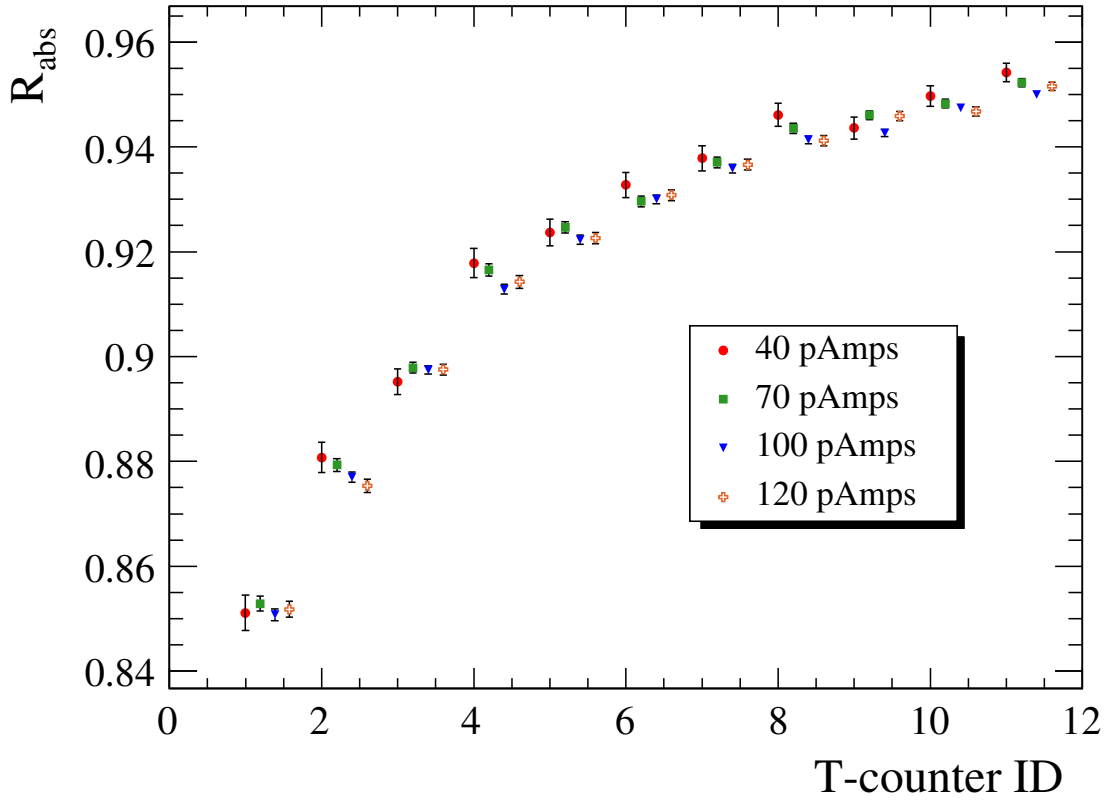


Figure 4.21: Tagging Ratios (R_{abs}) as a function of T-Counter for various calibration currents

4.2.7 The Pair Spectrometer and Relative Photon Flux

Since the TAC could only take data at roughly 0.75 pA of beam current, a pair spectrometer has been built and commissioned by the PrimEx collaboration for the experiment and general Hall B use. The Pair Spectrometer provided a relative measure of photon flux through the whole range of π^0 production beam current the collaboration had planned. The Primakoff targets served double duty as e^+e^- pair producers, and the commissioned 15 kilogauss PrimEx dipole magnet swept the pairs into the Pair Spectrometer. The Pair Spectrometer itself must have a relatively flat and continuous acceptance over the entire E_γ range. The two arms of the pair spectrometer consist of

eight telescopes each made of plastic scintillating material. They are placed symmetrically about the beam with overlapping momentum acceptance (Figure 4.2 and 4.22).

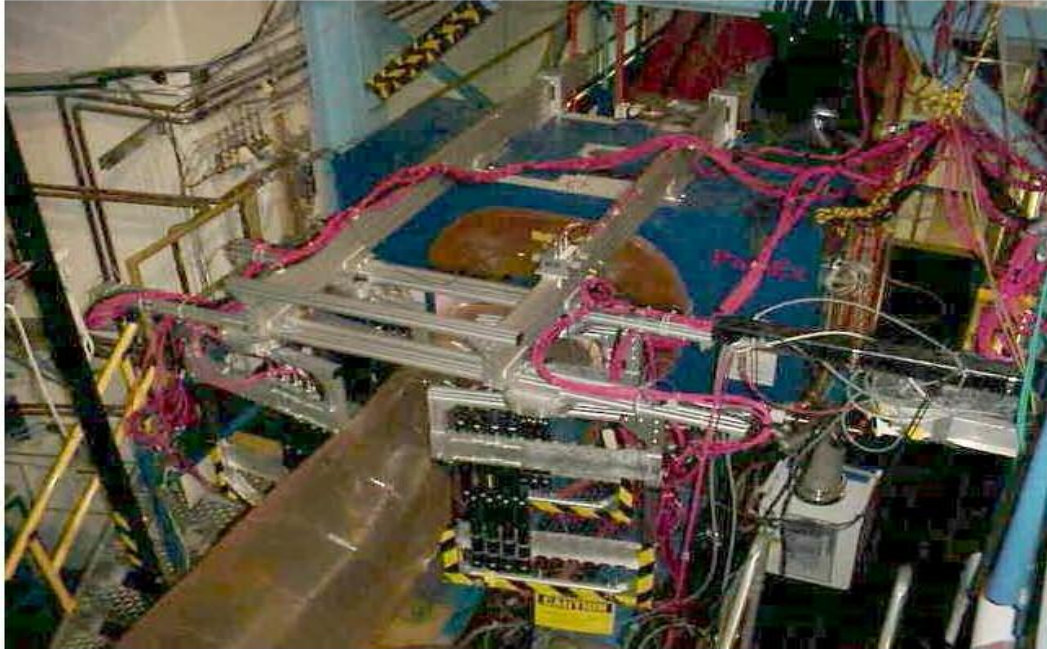


Figure 4.22: The Pair Spectrometer telescopes and helium bag (foreground) and the blue PS magnet. Beam direction points along aperture of PS magnet through helium bag

Prior to the Fall 2004 data run, this Pair Spectrometer's magnetic field was extensively mapped out. The magnet is on loan from Brookhaven National Laboratory and Jefferson Lab purchased the associated power supply. After refurbishing and installation into Hall B, three Hall probes were placed on or in the Pair Spectrometer magnet. One was located in the median plane of the magnet, and the other two at 2cm above and below the median plane. Field maps were taken at 0.5, 0.9, 1.0 (Figure 4.23), 1.3, 1.5, and 1.6 Tesla in May 2001. A Nuclear Magnetic Resonance (NMR) probe

allowed the collaboration to measure the central field vs. input current, i.e. the excitation curve. With this study, $[Bdl]$ was measured to better than 0.1%.

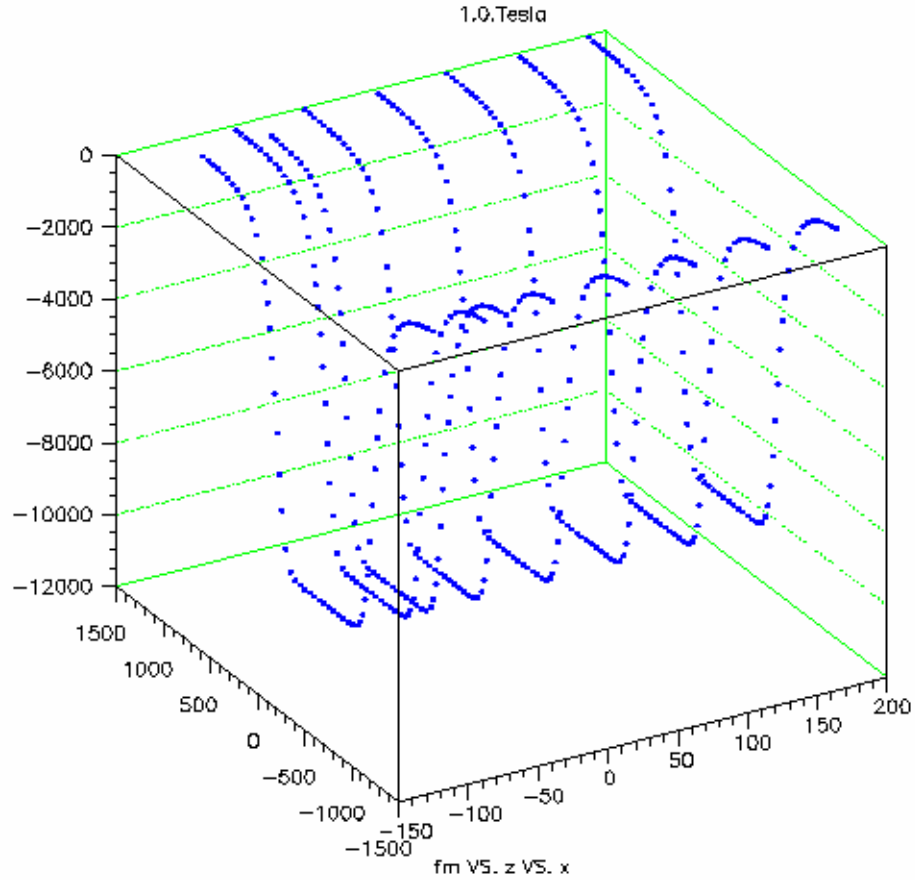


Figure 4.23: B-field map of the Pair Spectrometer dipole at a central field of 1 Tesla

The telescopes themselves are divided into two sections. The 16 front telescopes are $2.4 \times 7.5 \text{ cm}^2 \times 0.5 \text{ cm}$ thick and are coupled to Hamamatsu R6427 photomultiplier tubes, while the 16 rear telescopes are $9.3 \times 3.1 \text{ cm}^2 \times 2.0 \text{ cm}$ thick and are coupled to Hamamatsu R580-17 photomultiplier tubes. The photomultiplier tubes are μ metal shielded and the voltage dividers are modified to accept an extra power supply, enabling high rate capability for the last three dynodes. The 16 telescopes in the Front and Back sections are also symmetrically placed about the nominal beam in the

deflected charged particle plane. Thus there are 8 Front-Left, 8 Front-Right, 8 Back-Left, and 8 Back-Right telescopes. Single arm charged particles can be easily identified with a Front-Back in time telescope co-incidence. Charged particle pairs require in time, Front-Back, and Left-Right co-incidence. In order to ensure a good operating voltage for each telescope, each telescope had the applied voltage on the photomultiplier tube ramped up until a discernable plateau in count rate was seen. This procedure ensured that each telescope had an appropriate voltage on the photomultiplier tube for proper charge particle detection (Figure 4.24).

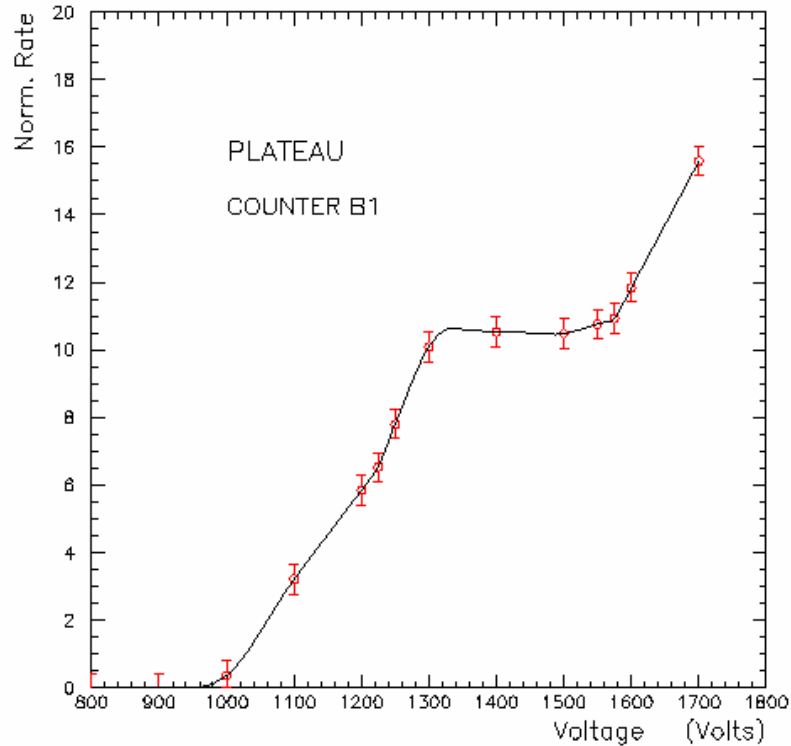


Figure 4.24: Sample Pair Spectrometer telescope high voltage plateau

In order to monitor photon flux at physics beam current, the number of electrons in the tagger must be counted and compared to the pair production rate detected in the Pair Spectrometer. Pairs from the ^{12}C physics target are counted and pair production rates are calculated on an experimental run by run basis. An ‘experimental run’ is

simply a two hour or less section of recorded physics beam time. By normalizing pair production rates to the number of electrons counted in the Tagger, the stability of the photon flux over the entire data collection time can be determined and any potential systematic shifts in flux evaluated. Using this methodology, current leakage and/or contamination effects from an unknown source were identified in some of our runs. This contamination caused extra events in the Tagger without correlated photons downstream in the Pair Spectrometer, thus causing a visually detectable drop off in the ratio of electrons counted in the Tagger vs. pair detection rate. The net effect of this contamination is to increase the uncertainty on the photon flux measurement (Figure 4.25).

Since this effect was noticed during the data run, a quick investigation during the experiment confirmed that this contamination was only present when either Hall A or Hall C were also receiving beam. When beam to the other Halls was turned off, the contamination disappeared. It re-appeared as soon as either or both other Halls started receiving beam again. While the source of this contamination in the accelerator is not known, the effect can be quantified and subtracted if the beam current in the other Halls is known. Fortunately, BPM current values for the other Halls are archived at 4.5 minute intervals a database and can be retrieved with minimal effort. Effort is being made to correct for the contamination. After correction, photon flux is projected to be known to approximately 1.0% or better, meeting the requirement of the proposed error budget

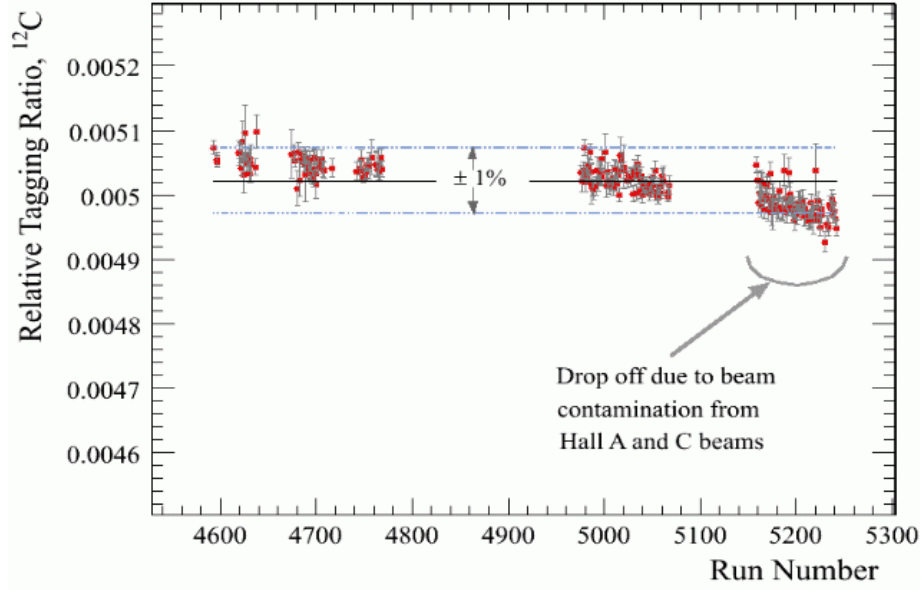


Figure 4.25: Relative tagging ratios (with contamination) vs. run number

4.2.8 PrimEx Hybrid Calorimeter (HYCAL)

The HyCal (Figure 7) is a highly segmented array of lead glass and lead tungstate (PbWO_4) crystals. The collaboration is quite frank in admitting that a calorimeter composed completely of lead tungstate would be optimal, but budgetary constraints have forced this compromise on the collaboration. In fact, the final number of lead tungstate modules was increased by more than a factor of two over the original proposal due to a fortuitous combination of lead tungstate crystal quality, and able negotiation on the part of our Chinese collaborators. The inner array of lead tungstate, centered about the nominal beam path, is constructed of 1152 modules of lead tungstate covering an area of roughly $70.38 \times 70.38 \text{ cm}^2$. Each lead tungstate crystal (Figure 4.26) is $2.05 \times 2.05 \times 18 \text{ cm}^3$ ($20 X_0$) and PbWO_4 has a radiation length of 0.89 cm and a Moliere radius of 2.0 cm. The Moliere radius is best defined as the transverse

radiation length for electromagnetic showers. The lead tungstate is wrapped in 100 micron thick TYVEK foil for individual optical isolation. A small brass faceplate and thin brass strips running along the length of each module guarantees mechanical coupling of the crystal to the Hamamatsu R4125A PMT and optical grease ensures good light coupling. The final average lead tungstate module cross sectional area is $2.076 \times 2.076 \text{ cm}^2$ (Figure 4.27). A 2x2 block section of lead tungstate crystal was removed from the array immediately around the beam path to allow the primary photon beam to pass through. Surrounding the lead tungstate is an exterior array of lead glass providing additional coverage in π^0 production angle.

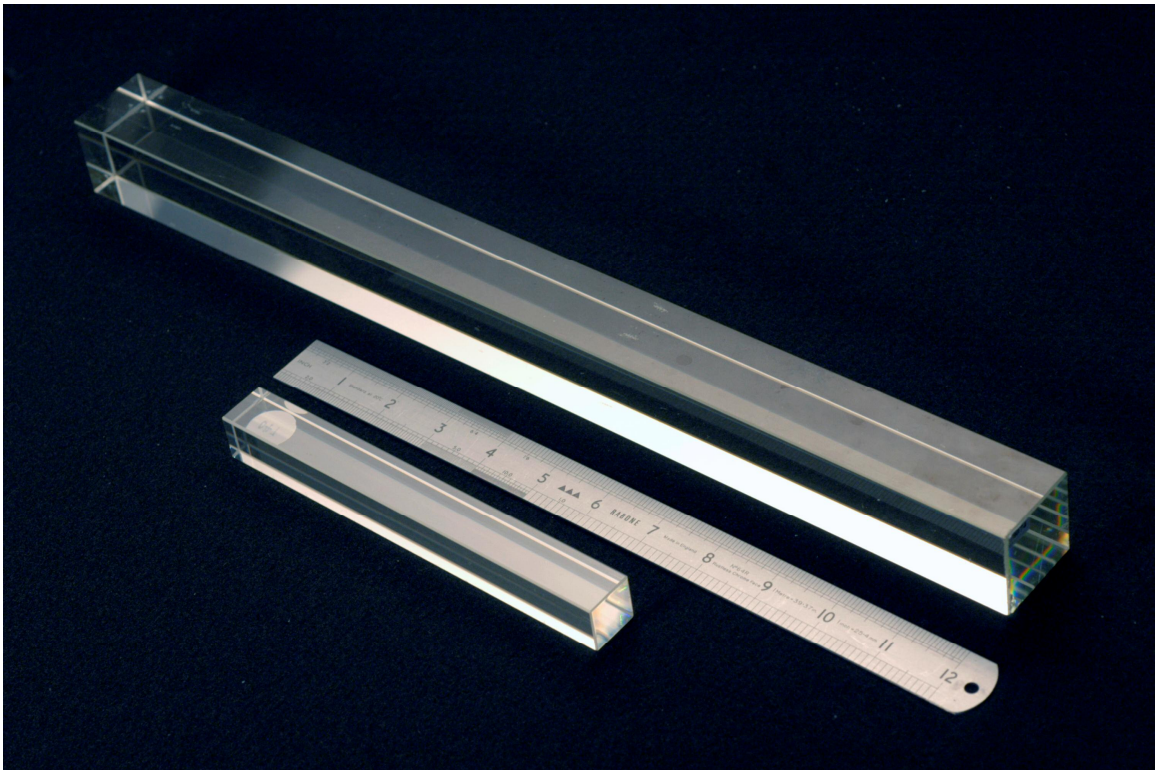


Figure 4.26: Sample Lead Tungstate (smaller) and Lead Glass blocks used in HyCal

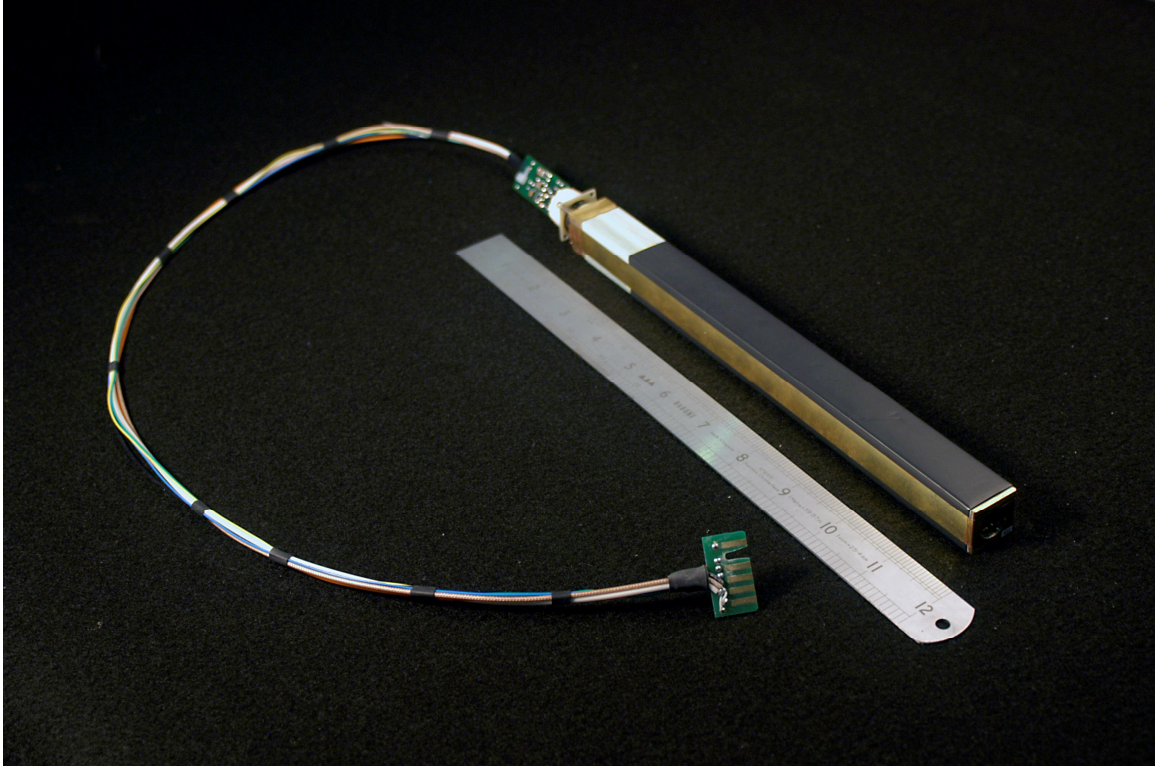


Figure 4.27: Sample Lead Tungstate module

The lead glass blocks are $3.80 \times 3.80 \times 45 \text{ cm}^3$ and has a X_0 of 2.7 cm (total 12 X_0). A thin wrapping of in 25 μm aluminized mylar optically isolated each individual lead glass block. Each detector is optically and mechanically coupled to Russian made FEU-84-3 PMT in a similar fashion as the tungstate (Figure 4.28). The total average cross sectional size of the Lead Glass module (wrapped and assembled) is $3.815 \times 3.815 \text{ cm}^2$. It was also necessary to maintain the whole array of lead glass and lead tungstate at a constant temperature of $\sim 5^\circ\text{C}$ because the optical properties of lead tungstate are very temperature dependent. The lower the temperature, the higher the light yield per shower for lead tungstate. A temperature of 5°C was optimal given available beam time, refrigeration equipment, and mechanical constraints.



Figure 4.28: Sample Lead Glass module

Each lead glass and lead tungstate is a stand-alone detector, and each is supplied with its own high voltage channel, anode, and dynode signal cables. This was accomplished with a minimum of connectors via custom designed and built mass circuit board and terminal connectors for the signal channels (Figure 4.29) and commercially manufactured mass termination blocks for the 2000+ channels of high voltage. Space constraints simply would not allow the required 5000 or more RG-58 and SHV BNC style connectors required. The bundling and shielding of these power and signal cables in addition to the tightly stacked and grouped detectors made it unfeasible to swap out a bad module for a new module. Extensive testing of each module before installation into the HyCal chassis minimized module failure. For all data presented in this dissertation, none of the lead tungstate modules experienced operational problems. Only 4 lead glass modules experienced total or partial failure during the same run time. Simulation

studies presented later quantify the effect of losing these channels in the data stream. Simulation can also be used to model these dead channels and provide acceptance corrected response functions.

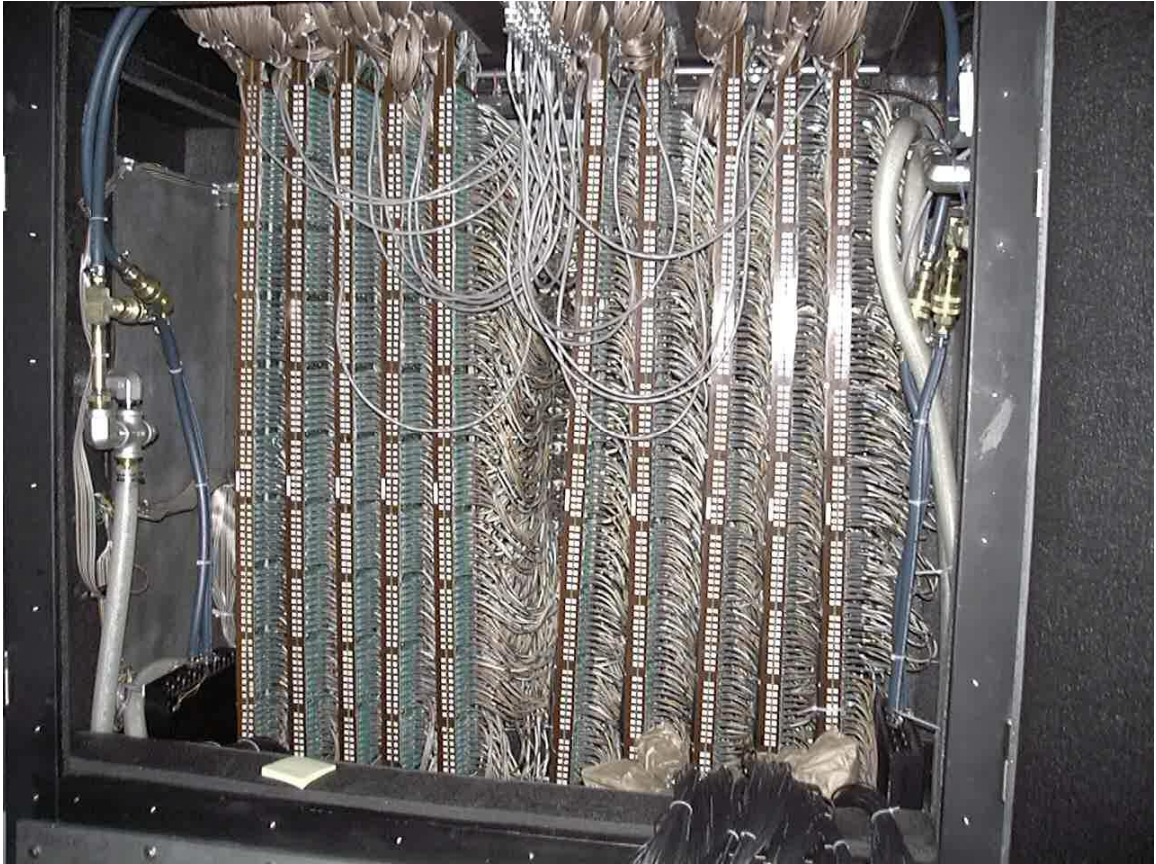


Figure 4.29: Back view of HyCal chassis showing custom printed circuit boards handling ~5000 data channels from HyCal.

HyCal was placed such that the lead glass detector face was 7.32 meters downstream of the photo-nuclear production targets. The lead tungstate face was inset an additional 15 cm downstream (Figure 4.30 and 4.31) to optimize energy sharing and minimize energy leakage. The distance of 732 cm from target to the face of the lead tungstate was optimal given small angle resolution concerns and space limitations in Hall B.

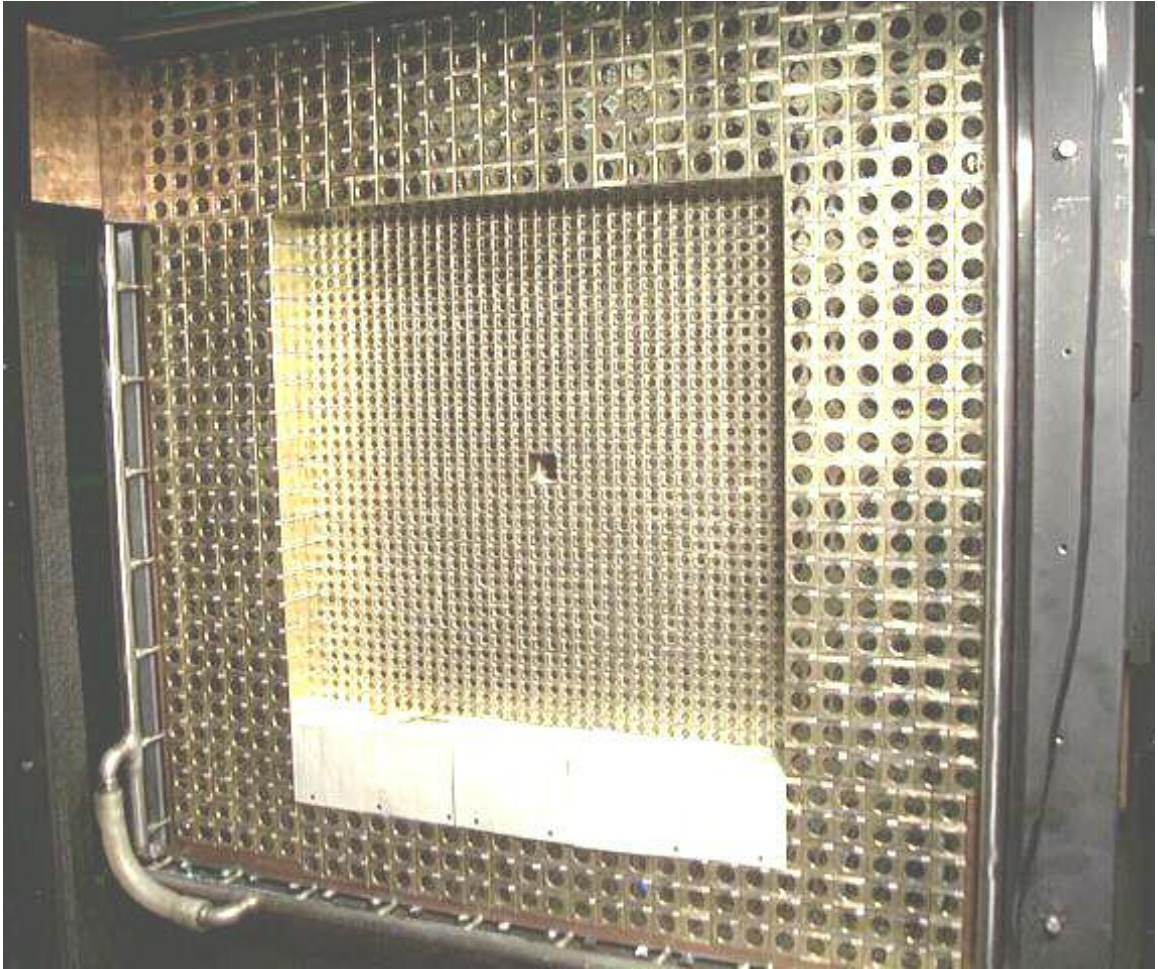


Figure 4.30: Front view of HyCal, fully stacked with inset Tungstate

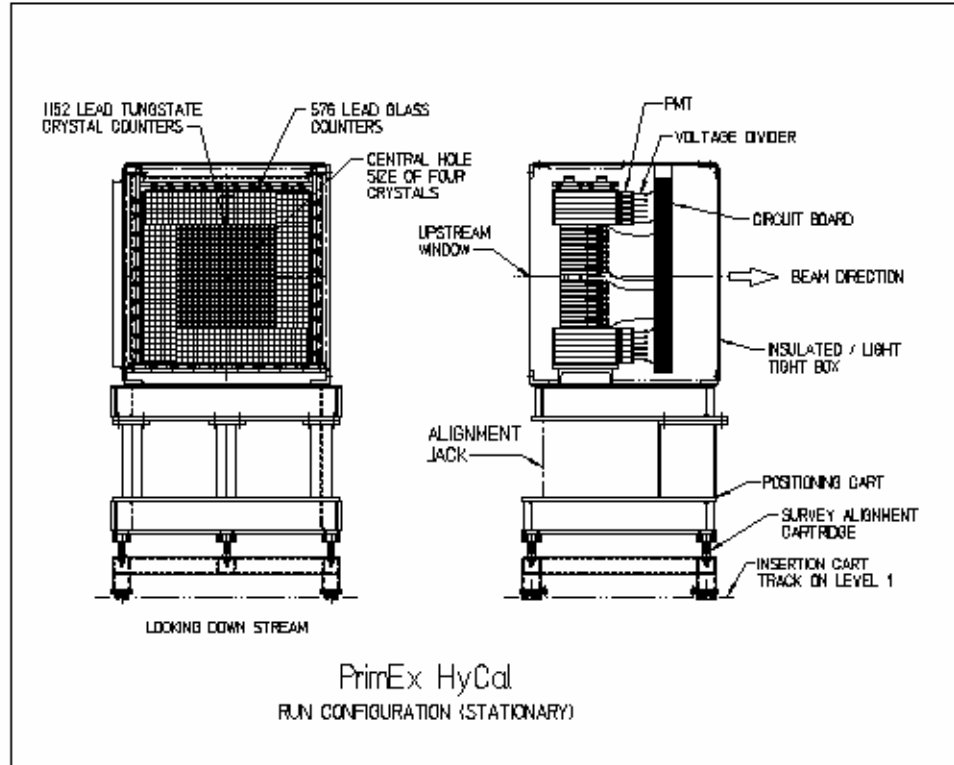


Figure 4.31: Front and view of HyCal and chassis in “run configuration”

Prior to taking any production π^0 data, HyCal was commissioned and calibrated. For this procedure, HyCal was placed on the HyCal Transporter (Figure 4.32). This is essentially a large 2-D stepper motor platform that could precisely position (within 2 mm) or move HyCal at constant velocities in the beam. The transporter was located at a fixed ‘z’ location such that the faces of the HyCal lead glass detectors were 582 cm from the Tagger target. In order to roughly calibrate the energy gain of the photomultiplier tubes, the collaboration irradiated the center of each detector with a low intensity (~ 100 pA) photon beam. Only one T Channel (T Channel 1, accessing the highest energy photons) was active, allowing a very limited energy range of photons. This gave a relatively narrow energy signal to timing co-incidence match in the selected HyCal detector. Adjusting the photomultiplier tube voltage until the reconstructed

energy was close to the requested beam energy yielded a reasonably gain calibrated detector. Additionally, so called “snake scans” were performed with a low intensity (~ 100 pA) photon beam and single active T Channel. These “snake scans” would start at the center of one detector and HyCal would be moved horizontally through the photon beam at a speed of approximately 2mm/s. At the end of the row of detectors, HyCal would be moved vertically up or down, and swept horizontally through the beam again, but in the reciprocal direction. This would then irradiate the next row of detectors. Each detector type was treated separately such that for a lead tungstate “snake scan” only lead tungstate crystals were irradiated. The same procedure applied to the rows of lead glass. Dedicated scans probed the transition region between lead tungstate and lead glass detectors. In this manner, calibration constants that averaged out finite detector size or energy sharing between detectors could be extracted. These studies commissioned HyCal. A subsequent (and much improved) generation of calibration constants used the π^0 mass as the calibration point. The “snake scan” calibration is referred to as such, and the second calibration is commonly referred to as the “ π^0 gain” calibration.

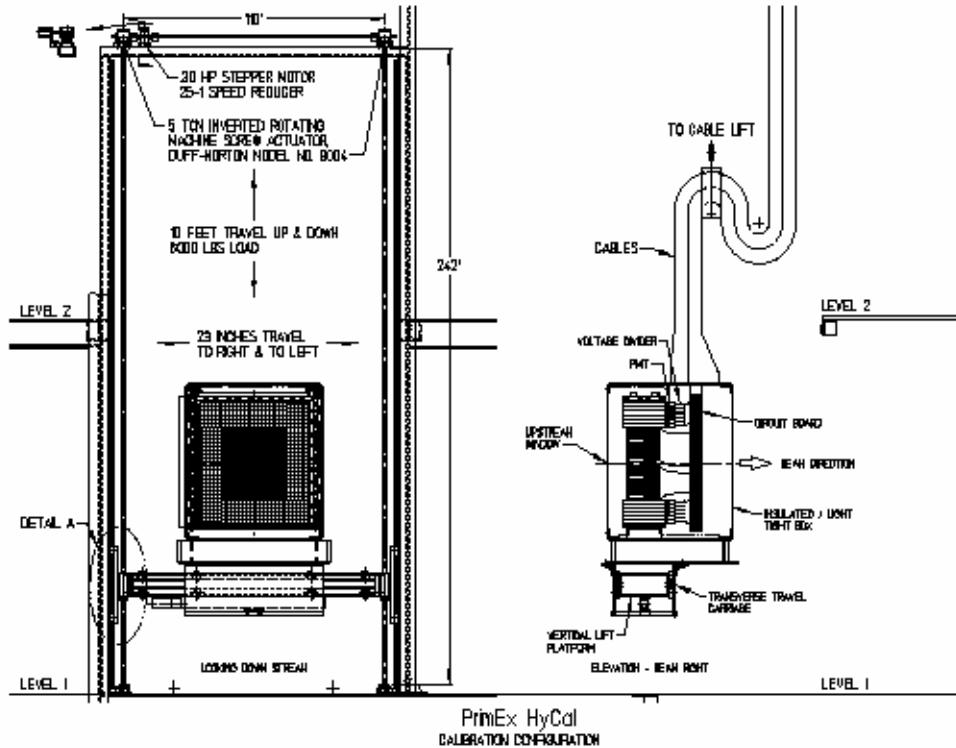


Figure 4.32: Views of HyCal, chassis, and cable handling while on the HyCal Transporter

As a final note, lead glass is a workhorse of nuclear and particle physics for decades. Its optical properties, Cherenkov shower development, and temperature dependent light transmission are well known. Lead tungstate, however, is a relative newcomer to photon calorimetry at the energies that PrimEx uses. In particular, lead tungstate's performance is well understood at energies greater than 10 GeV and less than 1 GeV [Citation??]. HyCal measured photons ranging from 0.5 GeV to roughly 5.5 GeV. For this reason, the collaboration made an extensive examination of the lead tungstate modules in an experimental beam prior to the Fall 2004 run time [23]. The collaboration tested lead tungstate crystals from two different manufacturers, Bogoroditsk (BTCP), Russia and Shanghai (SIC), China. From this beam test of roughly 4GeV electrons, the collaboration determined the SIC crystals had slightly

better energy resolution, 20% larger light yield, no difference in cluster position resolution over BTCP (~ 1.3 mm), and an improved light output with increasing radiation dose versus a worsen light output with BTCP with a 6x6 tungstate cluster size. Additionally, this beam test showed that the collaboration could get upwards of 1.2% energy resolution with 4 GeV electrons and a 6x6 lead tungstate cluster [citation proposal update]. The collaboration therefore purchased the SIC lead tungstate crystals.

4.2.9 HyCal Charge Particle Veto Counters

Peripheral equipment to the HyCal includes the Veto Counters and a Light Monitoring System. The Veto Counters are meant to mark any charged particle events that may enter HyCal for later filtering in offline analysis. A single veto counter is a $10 \times 0.5 \times 120 \text{ cm}^3$ organically doped scintillating plastic capped at both ends with an adiabatic lightguide and a Photonis XP2262/B photomultiplier tube. They were placed just outside the carbon fiber face of the HyCal chassis. They were oriented with the flat 10cm face normal to the beam line and vertically aligned such that the photomultiplier housing bore the weight load (Figure 4.33). This provided full charged particle veto to the entire fiducial face of HyCal. The design goal of the veto counters was nearly 100% charged particle detection efficiency and 1% photon conversion (charge particle mis-identification). The 0.5 cm thickness of the veto counters corresponds to a 1.2% radiation length to minimize photon conversion in the veto counter. Each veto counter was identical in construction to the next, save for the two interior veto counters. A single ply of 100 μm thick B1059B uncoated TYVEK enhanced light collection and two layers of black (25 μm thick) Tedlar optically isolated each veto counter.

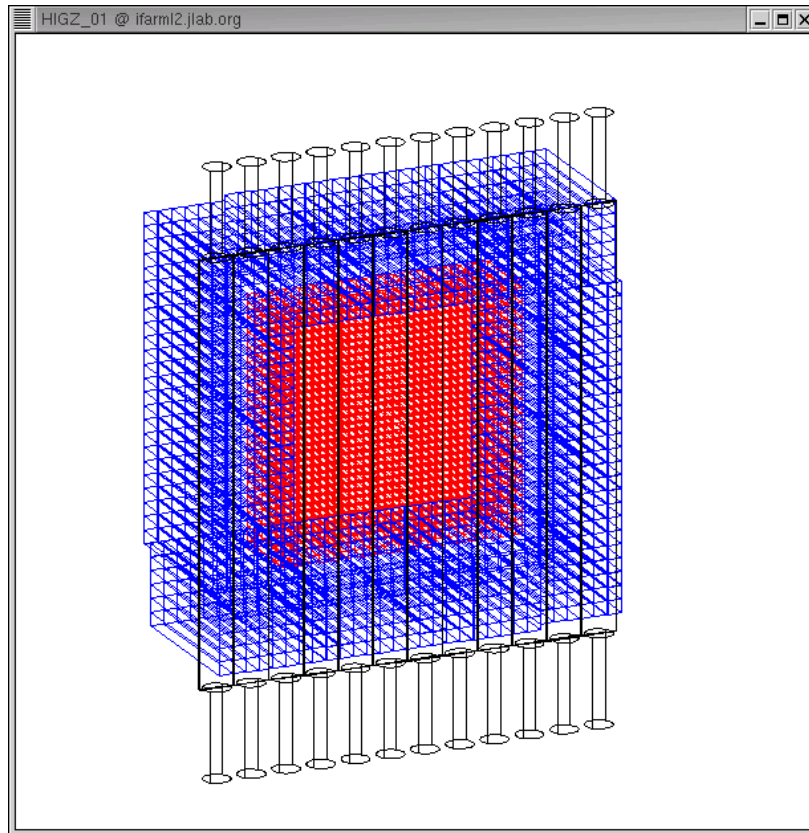


Figure 4.33: Placement of the Veto Counters in from of HyCal

Simulation of a bremsstrahlung photon beam incident on the two interior paddles suggested that a 2.26 cm semicircular cut-away on each interior paddle would minimize light loss, sufficiently minimize count rates from the bulk photon beam, and allow the bulk photon beam to pass through to HyCal and ultimately to the Sci-Fi (Figure 4.34 and 4.35). The full circular cut-away allowed the bulk of the bulk photon beam to avoid unreasonably high count rates in the interior paddles. This cut-away geometry also had the added symmetry of equaling the square area of the missing 4 fiducial central hole lead tungstate detectors.

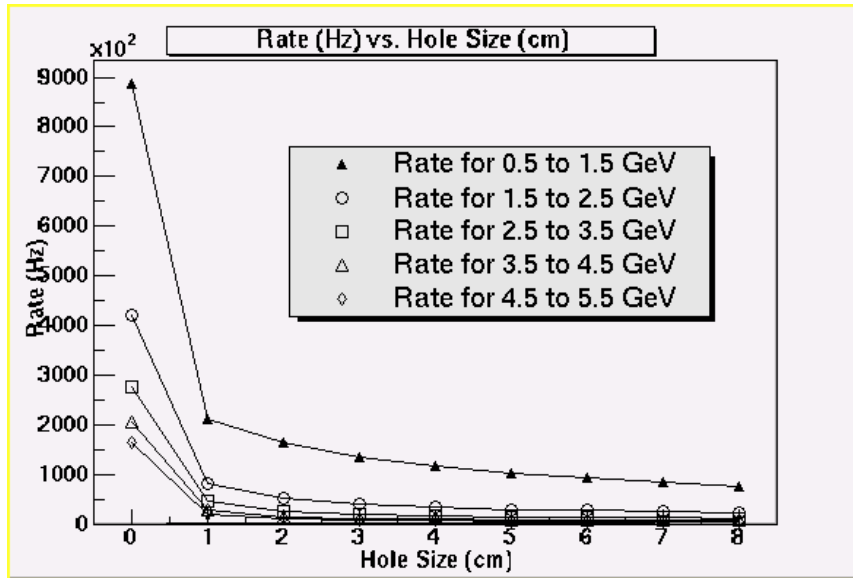


Figure 4.34: Veto Counter Rate vs. Central Hole size Simulation study

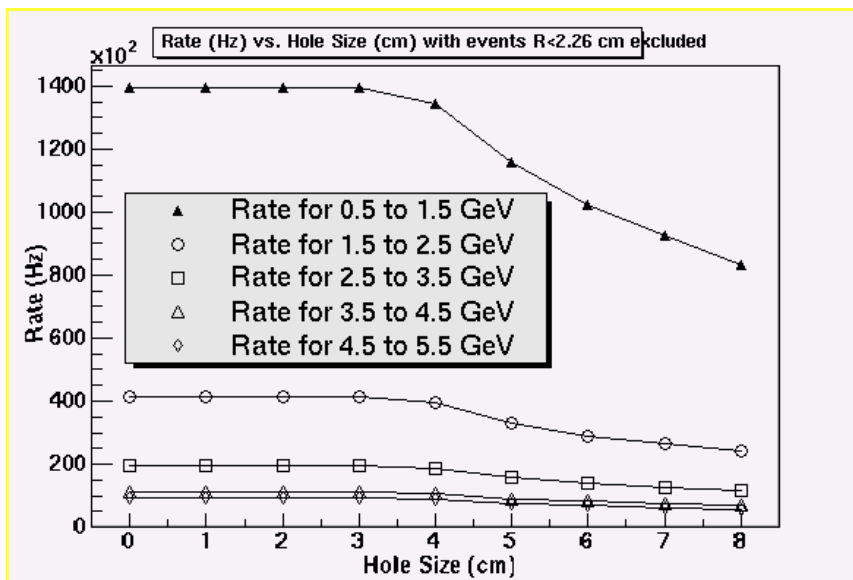


Figure 4.35: Rate versus Hole Size, all events less than 2.26 cm from Beam Center excluded, simulated.

Each veto counter photomultiplier tube was set to an appropriate voltage in a nearly identical manner as the Pair Spectrometer telescopes. The veto counters, being newly constructed, had not yet been commissioned by the start of the Fall 2004 data

run. Commissioning the veto counters involved illuminating them with low current photon beam and pair production runs. Some of this data was already present in the mentioned HyCal “snake scans”. The “snake scans” sampled the entire face of HyCal with horizontal sweeps across multiple veto counters and detectors in roughly 2.0 cm or 3.0 cm vertical steps. This meant that photon conversion efficiency could be evaluated at varying distances from beam center (and the center of the veto counters). For each veto counter, (a 10 cm bin in the horizontal direction), an appropriate ADC cut was determined to eliminate ADC pedestal events. Event (charged or photon) identification depended on a co-incidence between the top and bottom photomultiplier tubes of a veto counter. Additionally, “time walk” corrections provided improved timing resolution and charged particle identification. “Time walk” corrections are required, in the absence of constant fraction discriminators, to account for asymmetric light attenuation losses in a veto counter from an event that does not happen in mid-way between the photomultiplier tubes. Since the “snake scans” created events over the entire face HyCal and the total coverage of the veto counter array, “time walk” could be evaluated. From this data, an experimental photon conversion efficiency of $\sim 1.0\%$ was confirmed (Figure 4.36). To determine charge particle detection efficiency, pair production runs swept electrons through most of the veto counters at the mid-line of the detectors. The innermost paddles (with the central 2.26 cm) saw no charged particles due to the minimal magnetic field from the Pair Spectrometer dipole. With ADC offline sparsification known for each photomultiplier tube and “time walk” corrections implemented, charge particle detection efficiency was evaluated as nearly 100% (Figure 4.37). The resulting vertical spatial resolution for events in the veto counters is $\sim \pm 4\text{cm}$,

and the horizontal resolution (limited by the width of the counters) is ± 5 cm. This spatial resolution is sufficient to correlate with (and potentially veto) clusters reconstructed in HyCal.

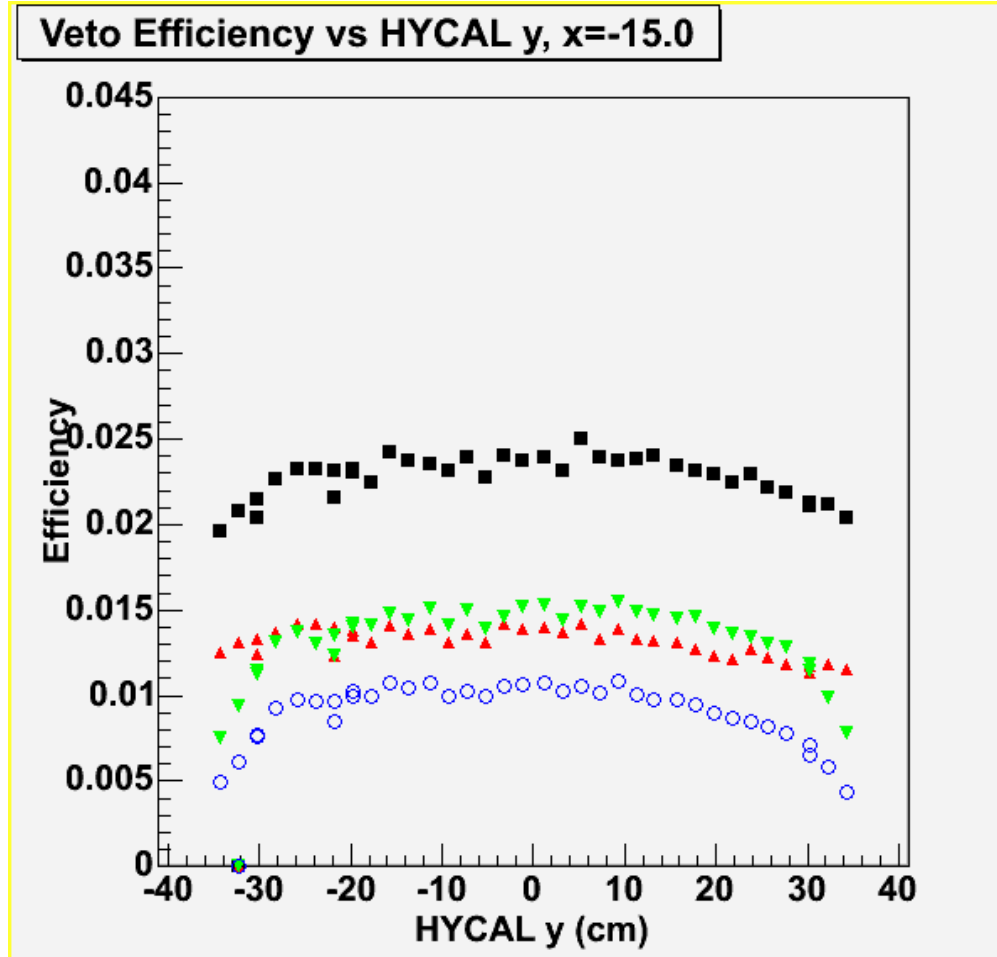


Figure 4.36: Photon Conversion efficiency for a typical veto counter. Conversion efficiency is sampled across the length of the veto. The black squares have no cuts applied. Red triangles have ADC sparsification, green triangles have 'y'-position matching, and the blue circles have ADC sparsification and 'y' matching applied.

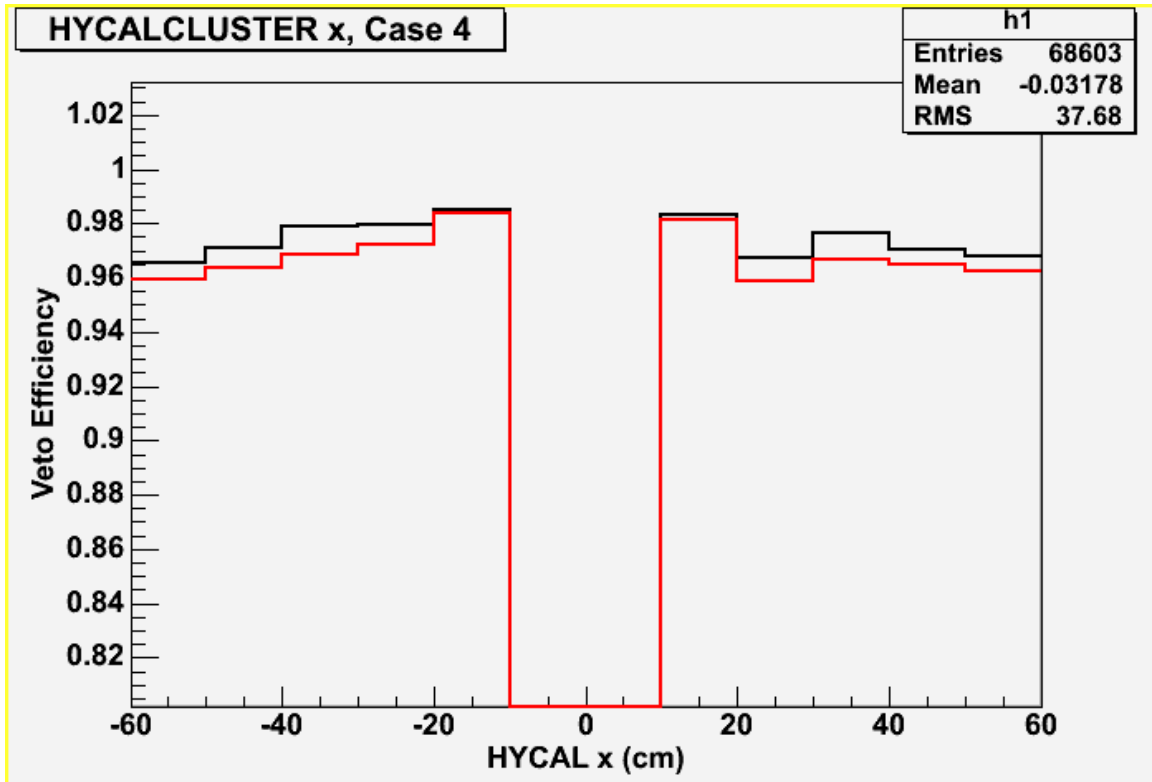


Figure 4.37: Charged particle detection efficiency midline along HyCal and veto counters

4.2.10 The Light Monitoring System

A Light Monitoring System (LMS) was installed to provide on and off line monitoring of the stability of all photomultipliers in the HyCal as well as control over any gain fluctuations in the ADCs. This removed the need for time consuming calibration of HyCal with the tagged photon beam. The LMS is comprised of a light source, light mixing and distribution systems, and reference detectors. The light source is an assembly of 31 NICKIA (NSBP 500S) super bright blue LEDs (peak wavelength of 470 nm, 40ns pulse length). This light source was stable to within 0.5% over a 5 minute period. The LED light was then mixed in a 6 in diameter OREIL integrating sphere, providing the required 2000 channel output to the 3 meter long, 265 μm diameter fiber optic cables. Three HAMAMATSU 580-15 (coupled to an Am^{241} α -

source and Yttrium Aluminum Perovskite (YAP) scintillator) and two PIN photo-diodes (Hamatsu S6468-05) provide stable calibration points for gain monitoring. Each HyCal detector has been coupled to a fiber optic cable with soft UV glue (DYMAX OP-4-20655 bulk modulus 200). The LMS data output was incorporated in the PrimEx data acquisition system. In order to ensure that the light from the LMS did not enter the physics data stream, each separate data run only collected LMS data during the first few (2-3) minutes of the data run. A filter wheel then blocked all light output from the LMS to HyCal.

4.2.11 PrimEx Data Acquisition, Trigger Design, and Event Rate

The effective collection of over 2200 ADC and TDC signals from the HyCal, the Veto Counters, Pair Spectrometer, Tagger, Total Absorption Counter necessitated the use of a high speed data acquisition system (DAQ). The PrimEx DAQ (Figure 4.38) utilized 3 Fastbus crates with power supplies, 28 Lecroy 1881M ADC's, 2 Lecroy 1877 TDC's, 52 slightly modified UVA 120A Linear Fan-In NIM modules (both outputs were inverting), 6 UVA 125A Fan-in Discriminator modules, 2 VXI/VMA JLab designed Trigger Supervisors, one CAMAC crate, one VME crate, and one hybrid VME/VXI crate. A CODA based software platform and a JLab designed Trigger Supervisor handled the final bundling of data and throughput to high speed Ethernet connection for storage on non-volatile memory.

The main PrimEx π^0 trigger was formed from any single or multiple cluster HyCal events with a total energy greater than 2 GeV in timing coincidence with an event in the Tagger. Blocks of like detectors, i.e. PbWO_4 or lead glass, were summed

Figure 1: Electronics Racks on Level 2 of Space Frame

57

separately (Figure 4.39), and fanned into a UVA 120 summing module from the custom printed circuit boards in the back of the HyCal chassis. From these fan-in modules built directly into the chassis containing HyCal, the signals went into a low impedance, fast RG-58 signal cable ($\beta=0.84$). These fast signal cables went directly to the UVA 125A fan-in/discriminator modules. Here, any HyCal event with greater the 2.0 GeV (summed over all clusters) of energy formed the first $\frac{1}{2}$ of the PrimEx π^0 trigger. A logical AND with any event in the Tagger in CAEN C542 Memory Look-up Unit (MLU) module formed the final physics trigger with an approximately 200 ns gate width. A second set of photomultiplier signals were sent through 200 ns of $\beta=2/3$ RG-58 signal cable. This delayed signal went into Lecroy 1818A ADC modules for integration (Figure 4.40).

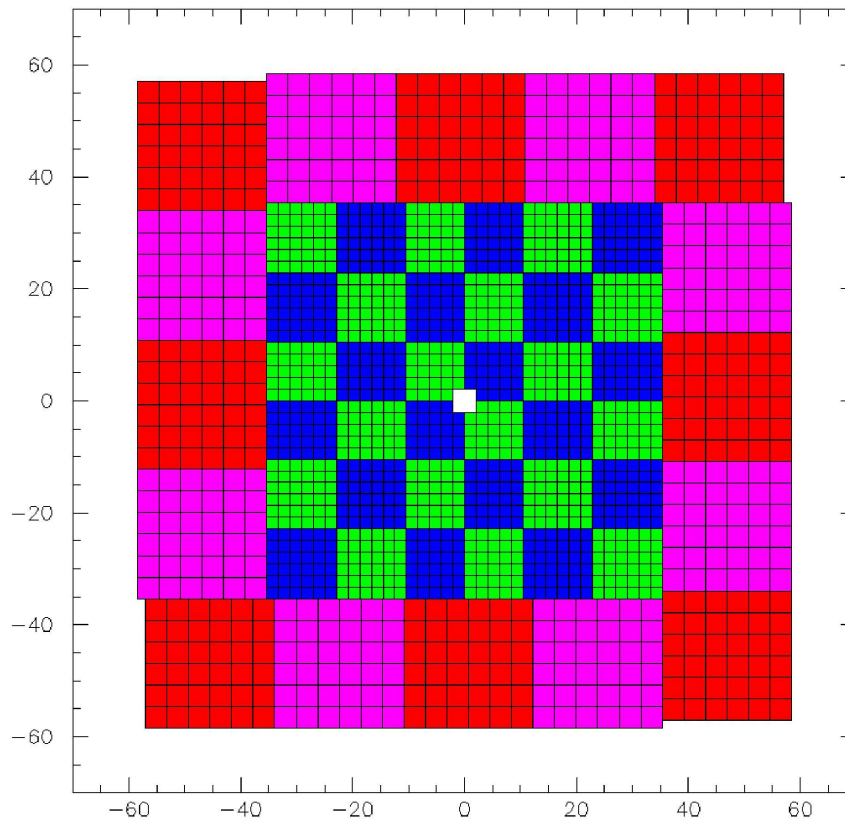


Figure 4.39: Blocks of like detectors going to individual UVA 120 modules

During physics running, the DAQ went through three separate “phases” where the list of triggers and pre-scale changed. During first phase (~1 minute) of the each data run, the DAQ collected 2000 pedestal count for all HyCal channels with no other triggers allowed. The second phase (~2 minutes) collected LMS data and no other triggers. The third and final phase initiated the physics triggers and any pre-scale on those triggers. The main π^0 trigger (~2 KHz) was not pre-scaled. The 200 KHz clock was pre-scaled to a 200 Hz rate. The Master ‘Or’ (MOR) trigger, a logical ‘Or’ of all active Tagger T-Counters, was pre-scaled (from ~12 MHz) to ~100 Hz. Both the clock and MOR triggers were used for photon flux accounting. The Pair Spectrometer coincidence with a Tagger event was pre-scaled (from ~90 KHz) to 10Hz.

CHAPTER 5

BACKGROUND SUBTRACTED NEUTRAL PION ANGULAR DISTRIBUTION

5.1 Data Source

The list of runs used in this analysis is over two hundred long. The queries to the PrimEx MySQL database

```
”mysql -h primexdb -u primex_user book_keeping -b --execute="select run from  
run_list where radiator='A' and target='carbon' and type='pi0' and  
production='good';" > run_list.example”
```

and

```
”mysql -h primexdb -u primex_user book_keeping -b --execute="select run from  
run_list where radiator='B' and target='carbon' and type='pi0' and  
production='good';" > run_list.example”
```

creates files with a list of runs taken with tagger radiator ‘A’ and ‘B’ respectively, PrimEx target ‘carbon’, the run type was π^0 production, and good production quality (no obvious defects). This run list is then compared with what has been cached to the Data Silo in the directory “/mss/hallb/primex/skim/october_2004/pi0_pass1/”. Any runs in the range 5060 to 5114 have been excluded due to proximity to the radiation accident affecting HyCal during PrimEx beam time. Any runs past 5242 are also excluded due to different HyCal location in Hall B. Appendix A has a complete listing of the data runs used in this analysis in the event that the production status of included or excluded run changes.

It is currently understood that skim1 data files are subject to the following 9 cuts/restrictions using the snake scan calibration constants. Additional cuts follow.

- 1.) Two or more clusters/event.
- 2.) Minimum three (3) (PbWO₄ or lead glass) detectors to define a “cluster”.
- 3.) 50 MeV or greater central (PbWO₄ or lead glass) crystal detector energy in cluster.
- 4.) 10 MeV or greater minimum deposited energy in (PbWO₄ or lead glass) detector.
- 5.) Max cluster energy 8 GeV.
- 6.) $\gamma\gamma$ invariant mass greater than 0.085 GeV in at least one of the cluster pairs.
- 7.) Elasticity (cluster pair energy sum/tagger energy) greater than 0.70.
- 8.) Cluster energy greater than 0.5 GeV.
- 9.) Cluster X or Y position must be greater than 3.8 cm.
- 10.) Cluster pair energy sum between 3.5 and 6.5 GeV -- additional software cut not imposed on the skim, but imposed later:
- 11.) Timing cut of -15 ns to +5ns.
- 12.) PrimEx veto counters are used to suppress charge particle background. Veto “Photon Misidentification Efficiency”, extracted in Chapter 5.6.
- 13.) Diffuse background cut, described in 5.3.1.

The HyCal calibration constants used in this analysis are the “pi0gain” values in the PrimEx calibration database.

Two slightly differing analyses will be presented owing to the hybrid nature of the calorimeter. We have extended our analysis over the entire HyCal fiducial volume, allowing us to access information about the shape and size of the nuclear incoherent cross section. However, the lead glass detectors do not have as good energy and position resolution as the tungstate detectors. Some systematic effects are not well understood when including these detectors in the analysis, and a radiative width extraction using the entire HyCal acceptance cannot be trusted. A reliable result can be obtained from the tungstate detector fiducial, where only tungstate-tungstate cluster pairs are considered. Also, other analysis groups in the collaboration have only analyzed data from the fiducial HyCal tungstate and thus have limited information regarding the nuclear incoherent background. Yields and systematics investigation using the HyCal *tungstate* fiducial will be presented first. This will be followed by a yield extraction and systematics investigation for the entire HyCal acceptance.

5.2 Method of event selection and evaluation of selection misidentification

Event selection is done via calculation of the likelihood of the event entry. We define likelihood as the value of the normalized probability density function (PDF) at a given location, i.e. $\text{Likelihood} = \text{PDF}(x = x_0)$. Cluster pairs were first subdivided into four categories: Tungstate-Tungstate, Tungstate-Glass, Glass-Tungstate, and Glass-Glass. The first detector type listed in each pair indicates which cluster measured the highest energy photon. Timing, elasticity, and mass spectrums are fit to polynomial background and to a signal PDF's called a skewed gaussian lineshape (Figures 5.1, 5.2 and 5.3 respectively). A single tail skewed gaussian, outlined by the Equation 2, characterized the signal shape while a polynomial (up to cubic order) lineshape was

used to understand the background. A skewed gaussian, for the purposes of this note, is defined as an exponential function convolved with a normal gaussian. It has skewness ‘ a ’, a width parameter “ σ ”, and a centroid of “ x_0 ”.

$$G(x) = \int_0^{\infty} \left(\frac{1}{a} e^{-y/a} \right) \frac{1}{\sigma\sqrt{2\pi}} e^{-\frac{(y-(x-x_0))^2}{2\sigma^2}} dy$$

$$G(x) = \frac{1}{a} e^{\sigma^2/2\sigma^2} e^{-(x-x_0)/a} \frac{1}{2} \left[1 + \operatorname{erf} \left(\frac{(x-x_0) - \sigma^2}{\sigma\sqrt{2}} \right) \right] \quad (5.1)$$

By switching signs on $(x-x_0)$, one can choose which side/tail of the gaussian to skew.

Charge particle veto was turned off (cut 12 in 5.1) for extracting PDF’s.

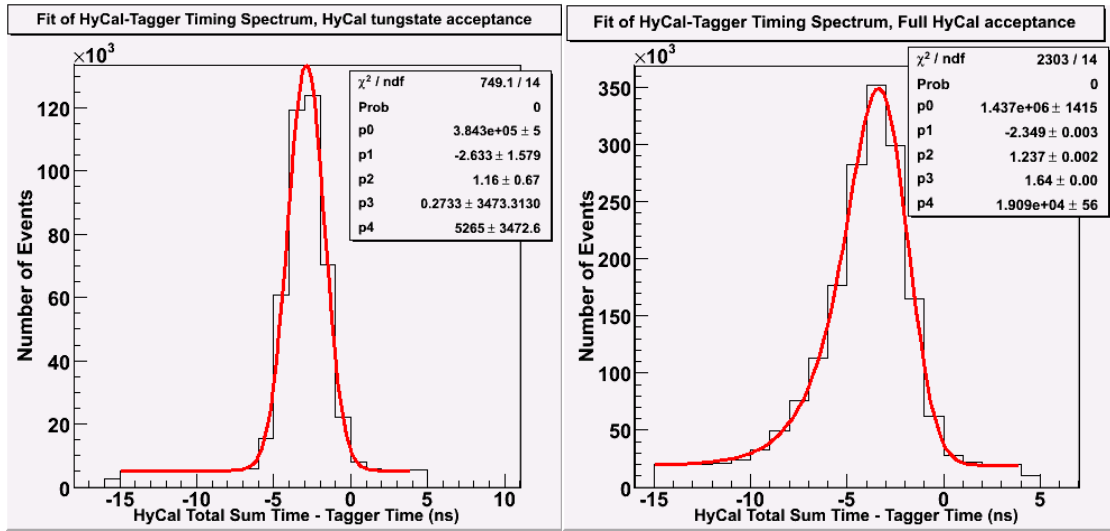


Figure 5.1: Sample skewed Gaussian fit of Tagger-HyCal total Sum co-incidence after Likelihood selection. Parameter p0 is amplitude analog, p1 is mean analog, p2 is width analog, and p3 is ‘skewness’. Parameter p4 is a zero-eth order polynomial term.

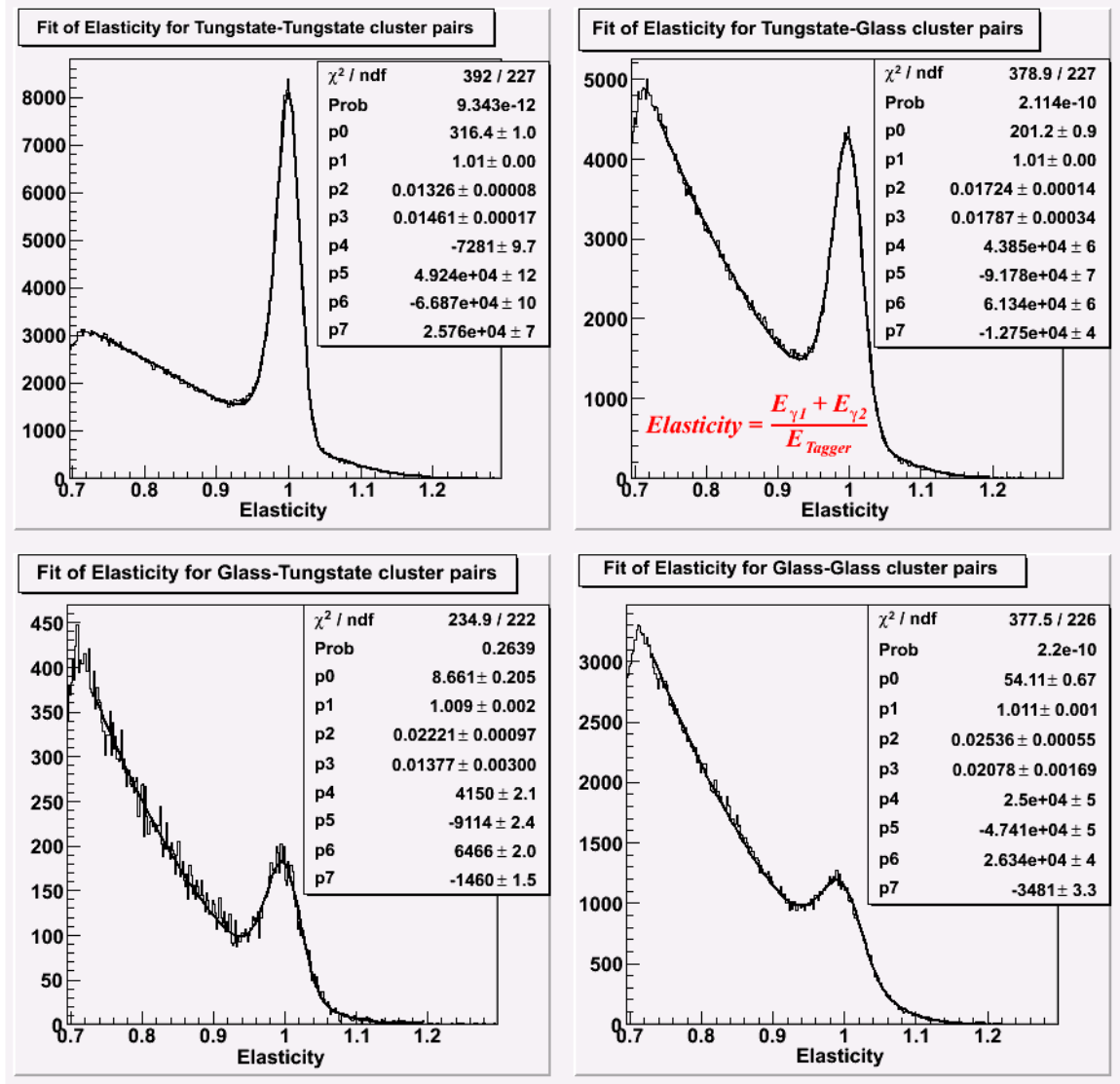


Figure 5.2: Skewed Gaussian with cubic background fit of elasticity for all cluster pair types. Parameter p0 is amplitude analog, p1 is mean analog, p2 is width analog, and p3 is ‘skewness’. Parameter p4 is a zero-eth order polynomial term.

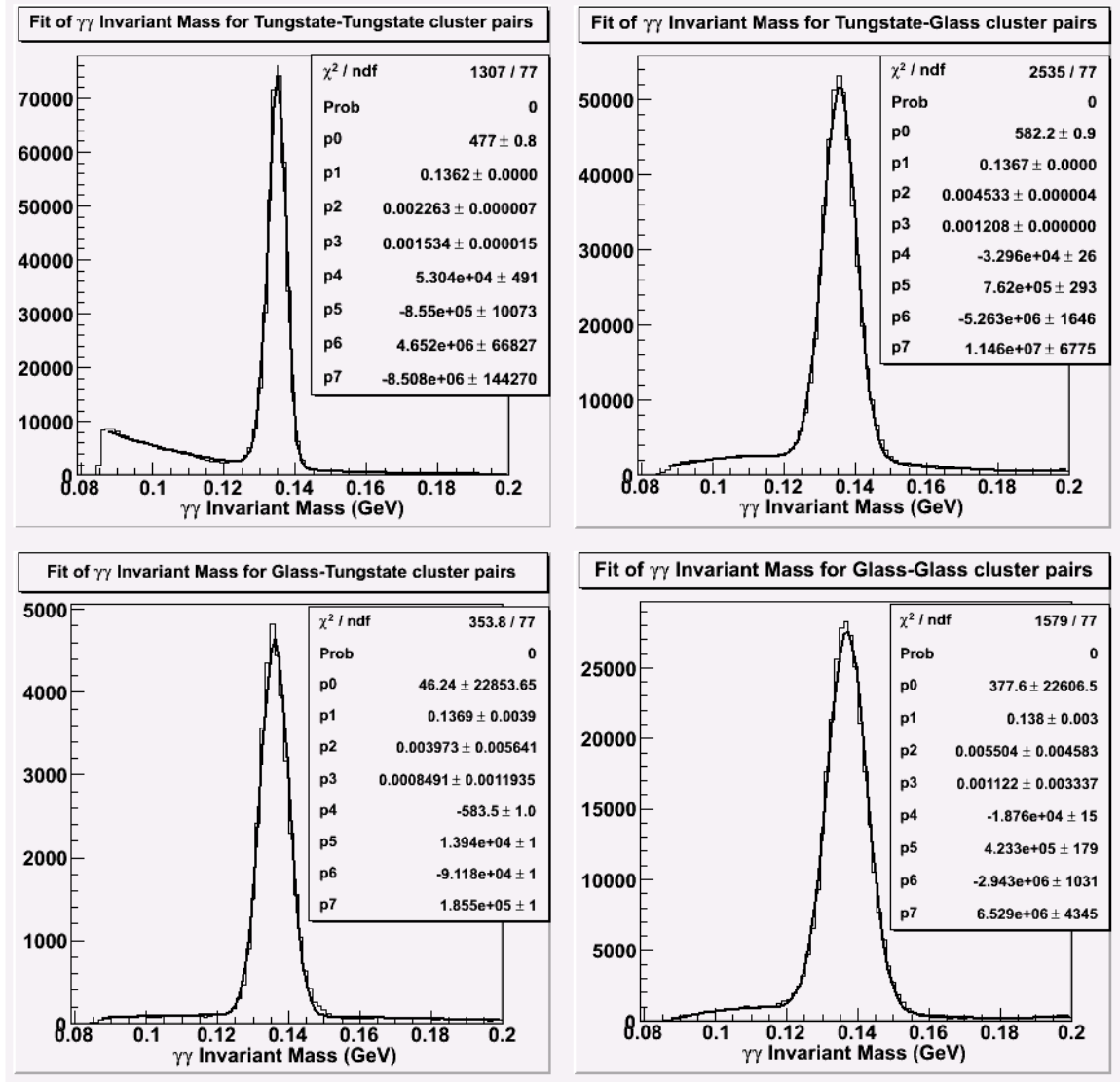


Figure 5.3: Skewed Gaussian with cubic background fit of reconstructed mass for all cluster pair types. Parameter p0 is amplitude analog, p1 is ‘mean’ analog, p2 is width analog, and p3 is ‘skewness’. Parameter p4 is a zero-eth order polynomial term.

Evaluating the PDF (normalized skewed gaussian lineshape) for each entry’s timing, elasticity, and mass values returns a likelihood value for each parameter. The final likelihood is calculated by multiplying these three parameter likelihoods (Figure 5.4). This final number ranges from 0 (most unlikely) to 1 (most likely). This sort of event selection eliminates the need for timing and statistical/combinatorial background

subtraction. It is possible that two entries in an event could evaluate to very similar likelihoods. The ability to choose the “wrong” entry is a worst case scenario. Such misidentification should hopefully be a sub-percent level event and randomly distributed over π^0 production angles. Sub-percent level misidentification suggests that our kinematic requirements and event selection are appropriate (Figure 5.5). If the misidentification of entries is random on an event by event basis, this event selection method will not contribute to any systematic error. For instance, a misidentification may de-populate the “correct” bin but another misidentified event could populate the initial bin, washing out any systematic mistakes in Most Likely event selection. From Figure 5.6 it is obvious that the event selection misidentification is random. It also tends to select event entries at slightly smaller π^0 production angles, minimizing inelastic background. Worst case misidentification (with charge particle veto and the diffuse background cut applied, cuts 12 and 13 in 5.1) of the most likely event is 0.28% (Figure 5.5) if one considers only the next-most-likely candidate and 0.30% if *all* not-most-likely candidates are considered. The misidentification percentages if one uses the full HyCal acceptance are 0.47% and 0.50% respectively. These misidentification percentages are calculated by counting the number of next most likely entries in an event that reconstruct to a *different* π^0 production angle. Multiple entries with the same production angle would increment the same bin, resulting in double counting. Additionally, multiple entries in an event are almost exclusively dominated by tagger multiplicity and not multiple cluster pairs in HyCal.

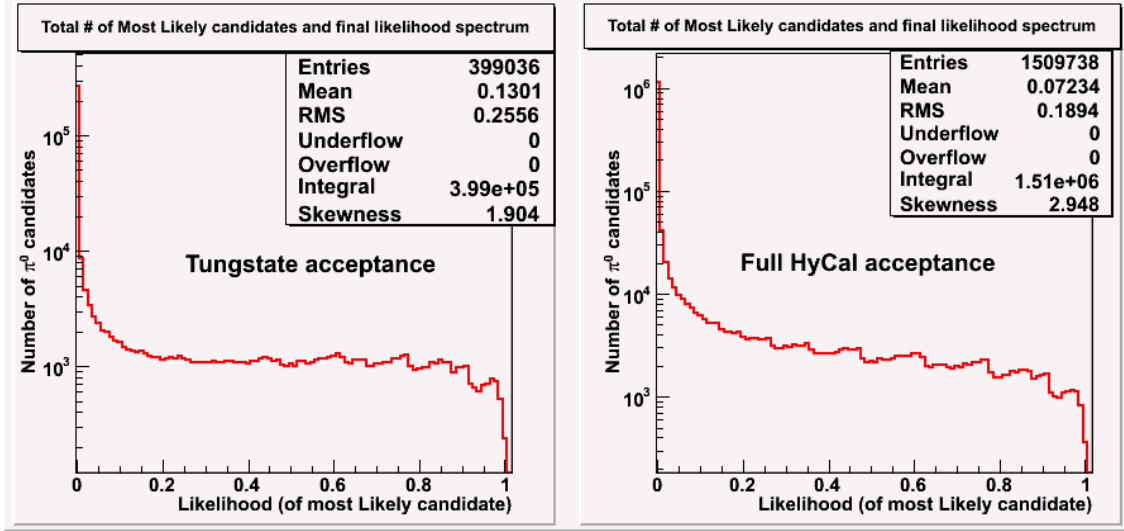


Figure 5.4: Final likelihood for most likely entries with time cut from 5.3.7. The “choppiness” of the distribution is an artifact of the 0.5 ns tagger timing resolution.

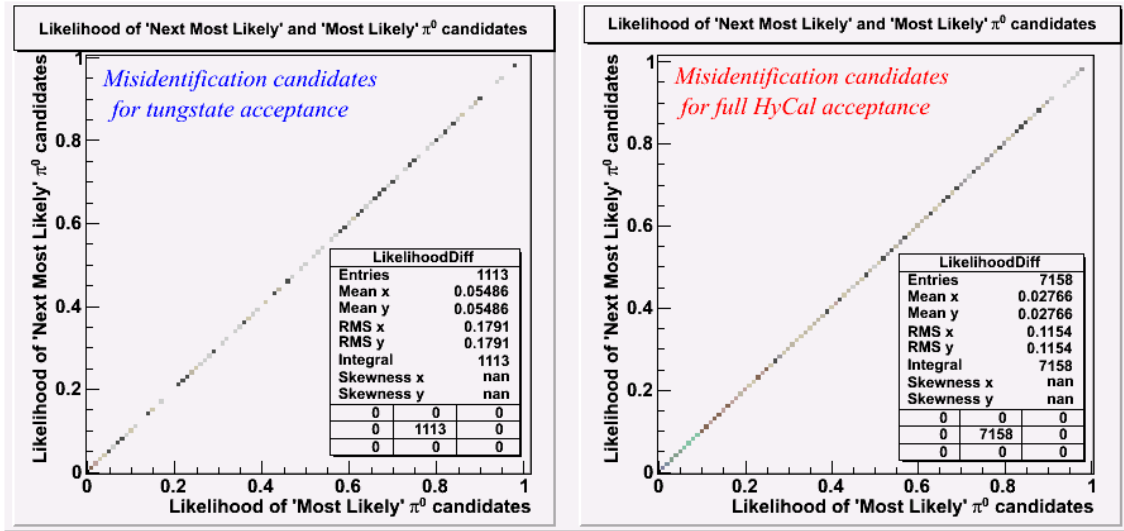


Figure 5.5: Misidentification of events with entries in different angular bins.
Tungstate acceptance Mis-ID = $1113 \div 399036 = 0.0028$

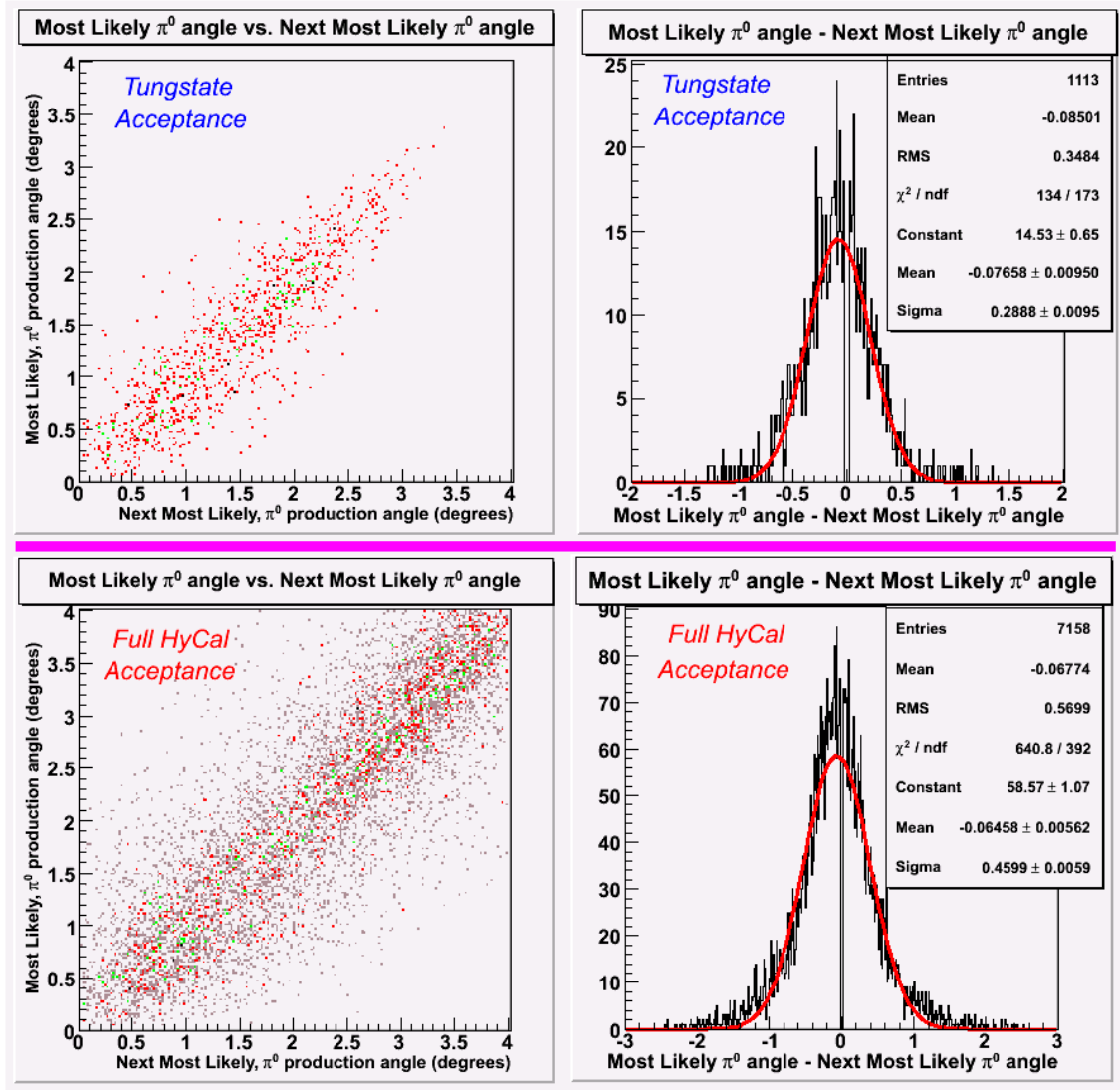


Figure 5.6: Angular distribution of Most Likely vs. Next Most Likely entries and “Most Likely π^0 production angle - Next Most Likely π^0 production angle”.

5.3 Yield extraction from HyCal Tungstate. Mass and Elasticity Correlation Enhancement

5.3.1 Mass and Elasticity Correlation Enhancement

With event selection well understood, plotting the Elasticity and invariant mass spectrums on a 2 dimensional histogram reveals a correlation around unit elasticity and the neutral pion mass. This correlation is Elasticity/Mass, represented by ψ (psi) in

Figure 5.7. This correlation is exactly the signal we wish to extract. It is also noted that two correlated (one to unit elasticity, another to the invariant mass) and one low mass and low elasticity diffuse background sources exist.

Defining a line orthogonal to this correlation and projecting all data (signal and backgrounds) onto this new axis clearly enhances the signal peak (Figure 5.8). By design, the equation of the orthogonal axis

$$f(x) = \text{Mass} \times \sin(\psi) - \text{Elasticity} \times \cos(\psi) \quad (5.2)$$

will center events at the origin of the new 1-D co-ordinate system. This rotation of the data is referred to as a “Hybrid Mass” spectrum. We believe that this technique will allow us to obtain mass resolutions comparable to what can be obtained by kinematic fitting, but without some of the issues that go along with that signal enhancement methodology. For example, in kinematic fitting when events far from the elastic peak are “pushed into” the elastic peak, it isn’t obvious (at least to us) where these events will end up in the $M_{\gamma\gamma}$ distribution. Does kinematic fitting introduce structures, cusps, etc. where there was formerly a smoothly varying background? We believe our technique avoids this uncertainty. Additionally, we are able to make another cut on the low mass and elasticity background. We define another line orthogonal to Equation 5.2

$$d(x) = -\text{Mass} \times \cos(\alpha) - \text{Elasticity} \times \sin(\alpha) + 0.215 \quad (5.3)$$

where $\alpha = 1/\psi$ and place the y-intercept of that line such that we can cut away significant amounts of the diffuse background but still preserve the elastic and inelastic invariant mass backgrounds (Figure 5.9). Figure 5.10 shows the pion candidates in the diffuse background at sample angular bins. There is no elastic peak in these spectra,

and any structure in these spectra is an artifact of rotating the 2-D data (with pre-existing cuts) onto 1-D, additional confirmation of a background source.

5.3.2 Signal and Background Lineshape and Integration Range

The peak signal was characterized by double normal gaussians. Background subtraction is accomplished by fitting a simple second order polynomial to the background. Figure 5.11 shows sample fits of the Primakoff peak, Interference region, and Coherent process region, respectively. *Please note, all π^0 production angles presented in this note are reported in degrees unless specifically indicated otherwise.* There is an elastic background shown in Figures 5.8 and 5.11 that dominates at very small angles. Above roughly 0.1° the inelastic background becomes much more pronounced. Any lineshape will need to characterize these two backgrounds sufficiently well at all angles

A double Gaussian lineshape was preferred over skewed or a single Gaussian lineshape due to its consistent and sharply defined characterization of the elastic yield over the entire π^0 angular spectrum. A second order polynomial possesses enough degrees of freedom to properly characterize elastic and inelastic background sources across the entire π^0 angular range. The yield for each 0.02° slice of π^0 production angle (Figure 5.12) was calculated by subtracting the background lineshape yield from the counts over a fixed range for the entire angular range. Uncorrected differential cross sections are trivial to calculate from Figure 5.12, and will be presented in Chapter 7.

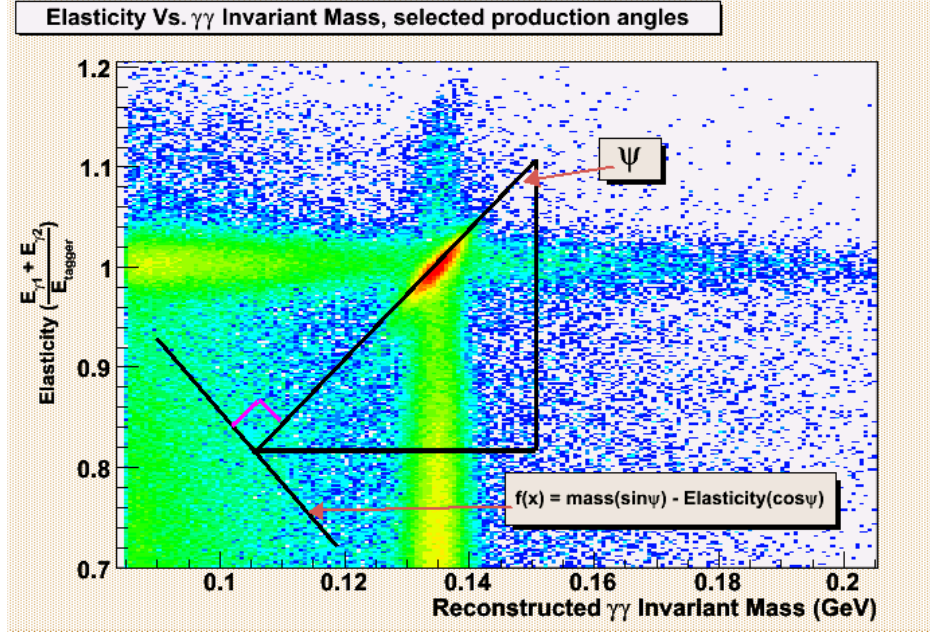


Figure 5.7: Correlation of Mass and Elasticity for selected angles

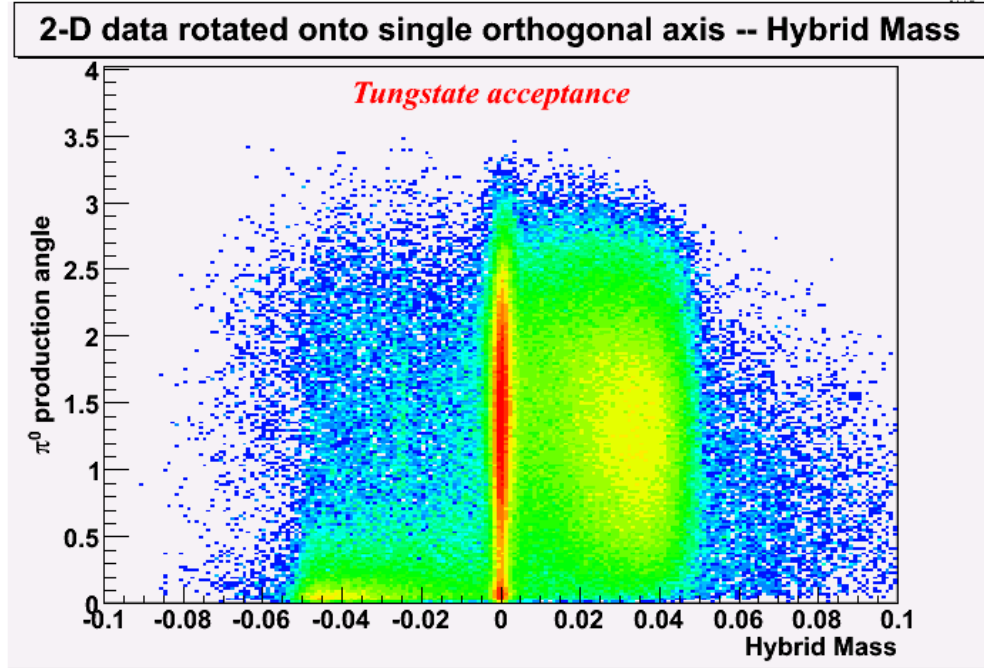


Figure 5.8: Projection of (HyCal tungstate acceptance) data onto the Orthogonal axis

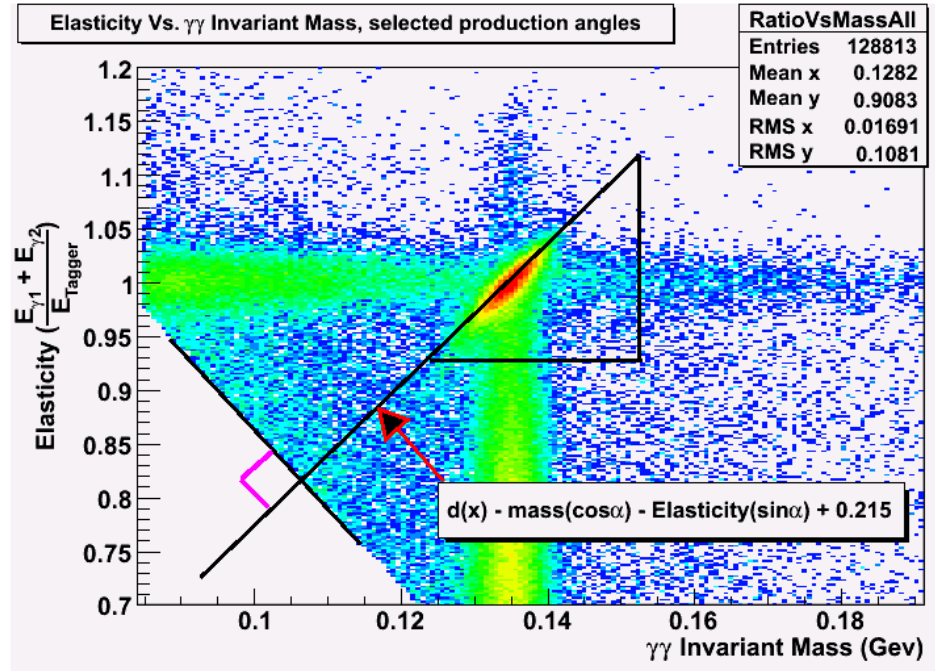


Figure 5.9: Correlation of Mass and Elasticity for selected angles with diffuse background cut away

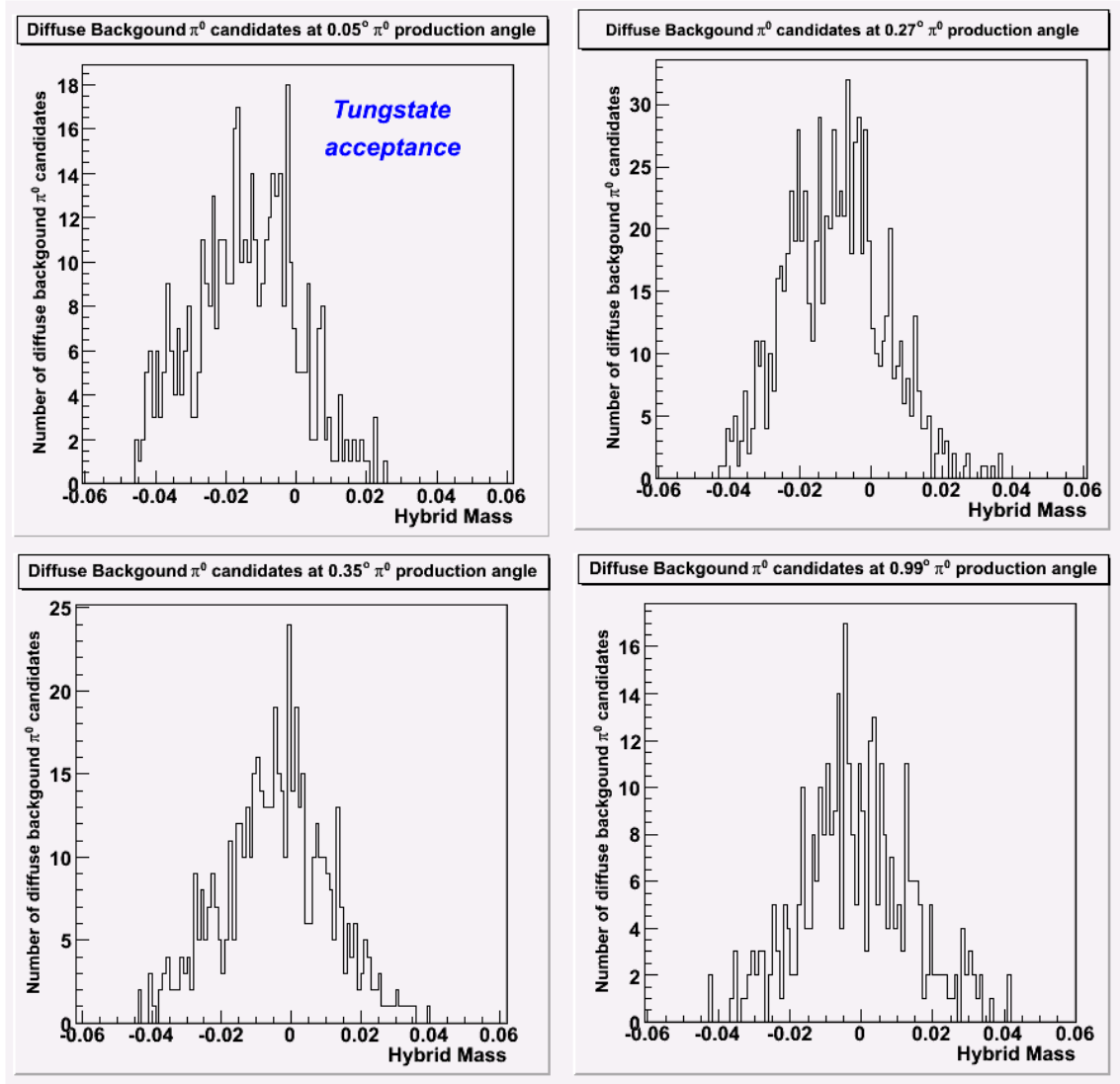


Figure 5.10: Pion candidates removed by the “diffuse cut”

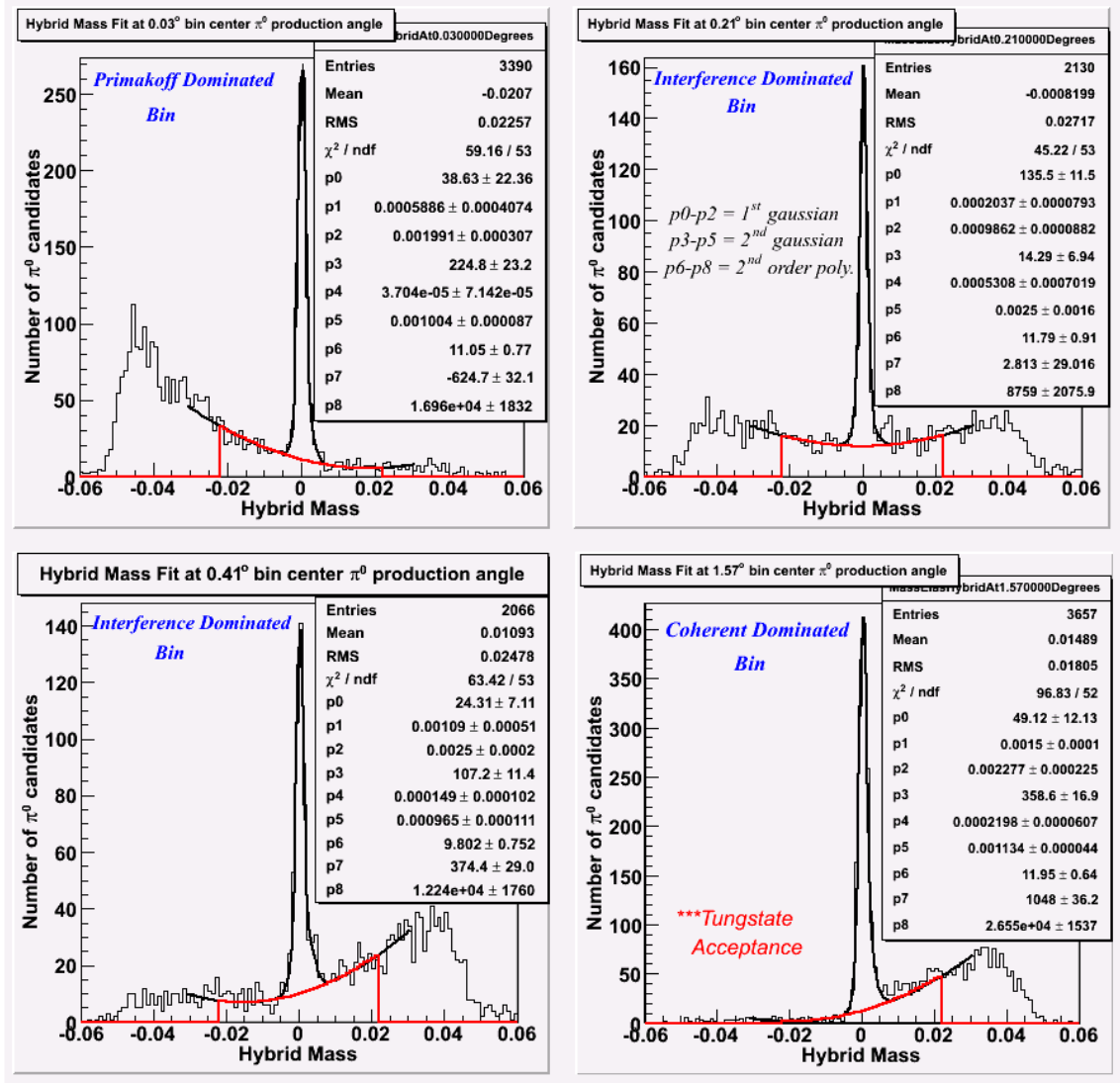


Figure 5.11: Sample Fits at selected π^0 production angle bins, HyCal tungstate acceptance.

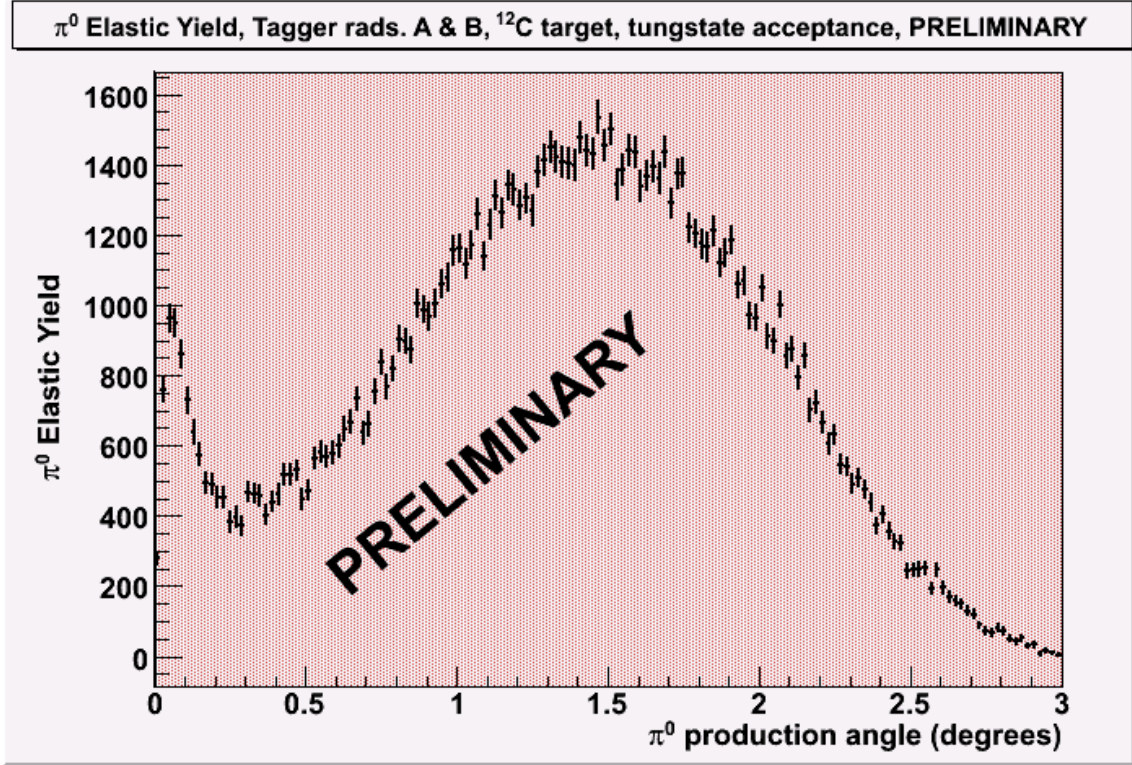


Figure 5.12: π^0 Yield as a Function of Angle, HyCal tungstate acceptance

5.3.3 Maximizing pion signal to noise

Software cuts on the data have been very generous for fitting Likelihood PDF's. However, a great deal of background that was eliminated before final yield extraction in Figure 5.12. In order to understand what additional cuts or constraints we put on the data in Figure 5.8 and Figure 5.12, we searched for plateaus in the elastic pion signal as a function of timing window, background subtraction range, and lineshape and background fit range.

5.3.3.1 Elastic Pion Yield Versus Timing Window.

The cut time window cut placed on the data was originally set to 20ns, ± 10 roughly centered on the timing peak (Figure 5.1). We performed the likelihood event selection and extracted yields using the nominal signal and background lineshape (discussed in 5.3.2) for the various timing windows (Figure 5.13). A time window of 6 ns (± 3 ns) appears to be the start of the plateau of the elastic pion yield, and rejects significant background. It is noted that there is an accidental background suppression on the elastic yield. By fitting a 1st order polynomial to the slope (where there should be a plateau), we calculate a $1.01\% \pm 0.2\%$ correction to the final radiative width.

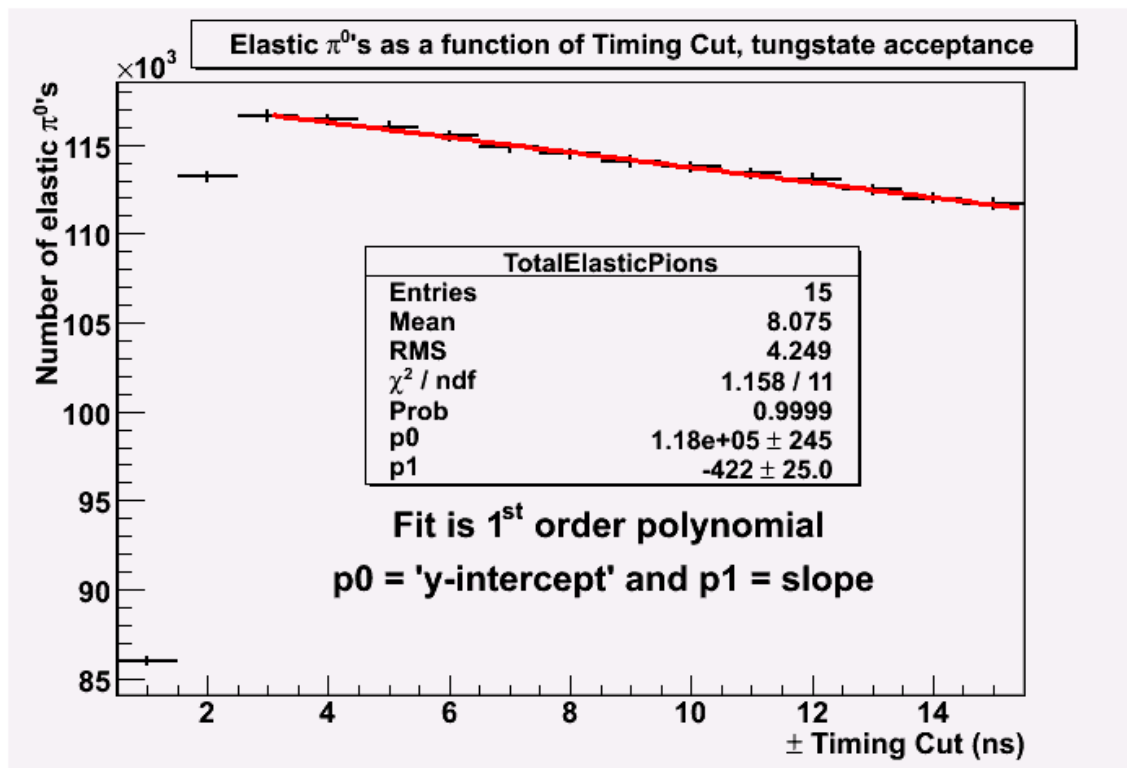


Figure 5.13: Elastic pion yield as a function of the timing window, HyCal tungstate acceptance

5.3.3.2 Elastic Pion Yield Versus Fit Range.

The unique backgrounds in this analysis pose a particular challenge regarding background subtraction. Care should be taken to ensure that elastic pion yield does not depend on the range over which the fits are determined. The purpose of this investigation is to ensure that the yields do not vary when changing the number of data bins in the fit. It is not clear where exactly a plateau may exist in Figure 5.14 below. However, we can plot extracted radiative widths as a function of the Fit Range (with in Integration range of 0.022 HMU's). There is a clear plateau from 0.028 to 0.034 HMU's (Figure 5.15). We use 0.031 HMU's as the nominal Fit Range.

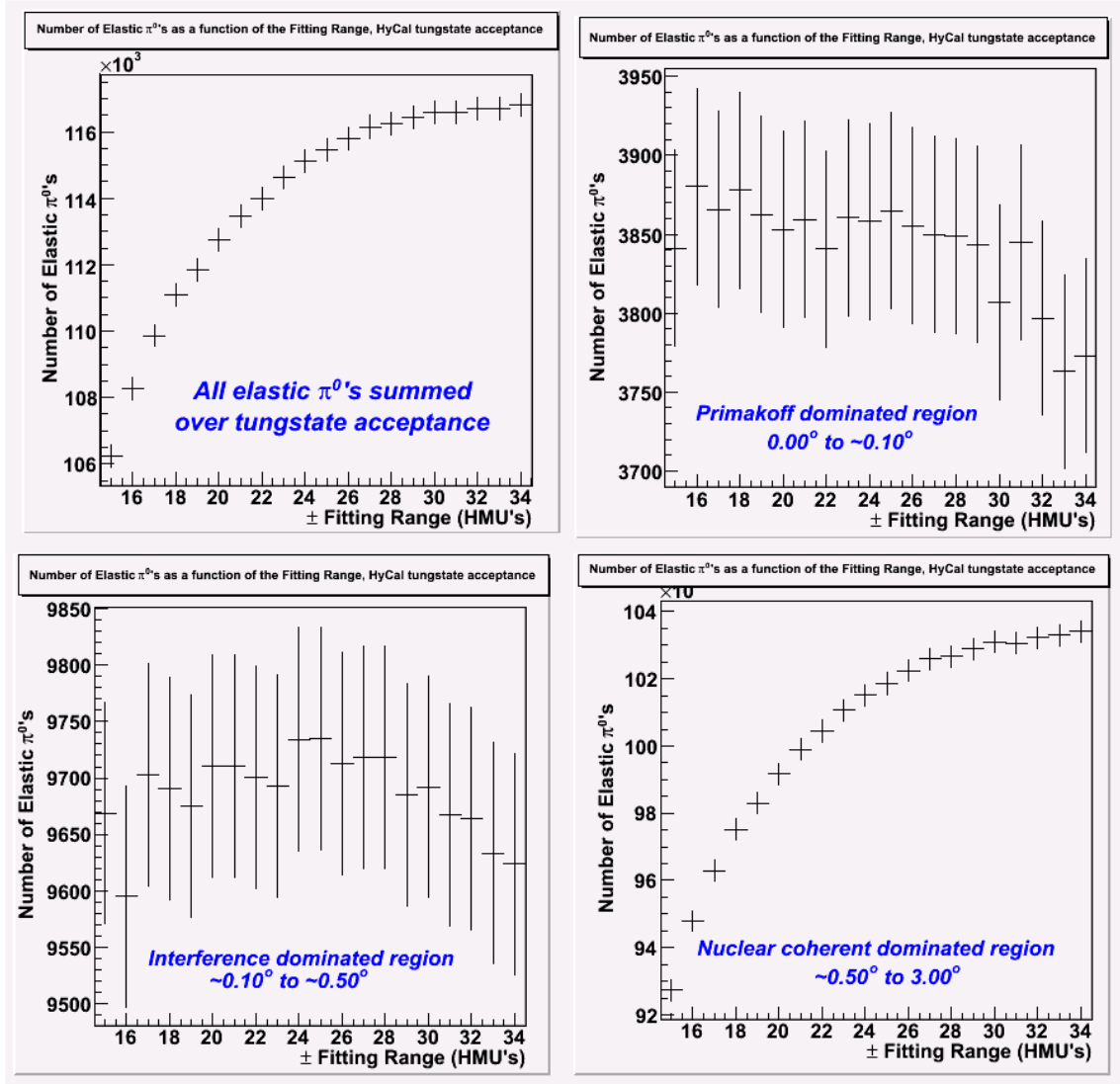


Figure 5.14: Elastic pion yield as a function of photonuclear process dominated angular regions and the fitting range, integration range = 0.022 HMU's, HyCal tungstate acceptance

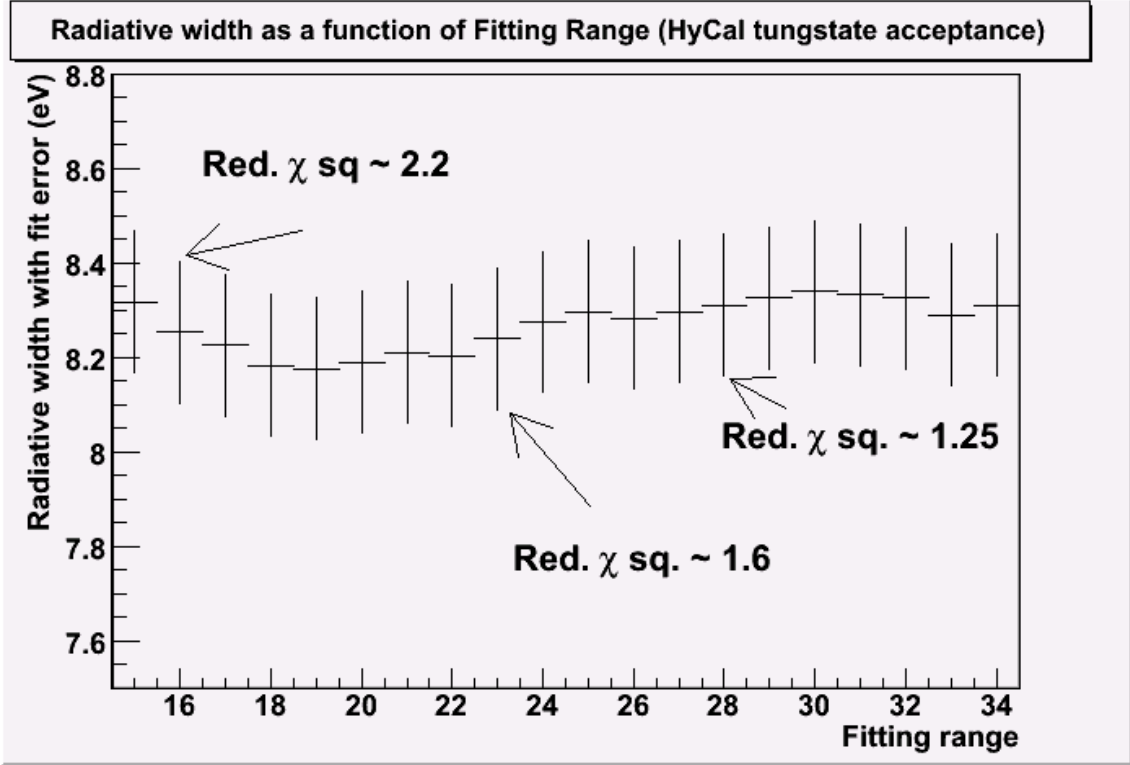


Figure 5.15: Radiative width as a function the fitting range, integration range = 0.022 HMU's, HyCal tungstate acceptance.

5.3.3.3 Elastic Pion Yield Versus Background subtraction range.

We again employ the method of finding a plateau in the elastic pion signal to determine the background subtraction range we will employ for all π^0 angle bins (Figure 5.16). Again, it is not clear where any plateau may exist, but if we plot the extracted radiative width as a function of the integration range, a plateau emerges (Figure 5.17). From this study, we have chosen 0.022 Hybrid Mass Units (HMU's) as the background subtraction range.

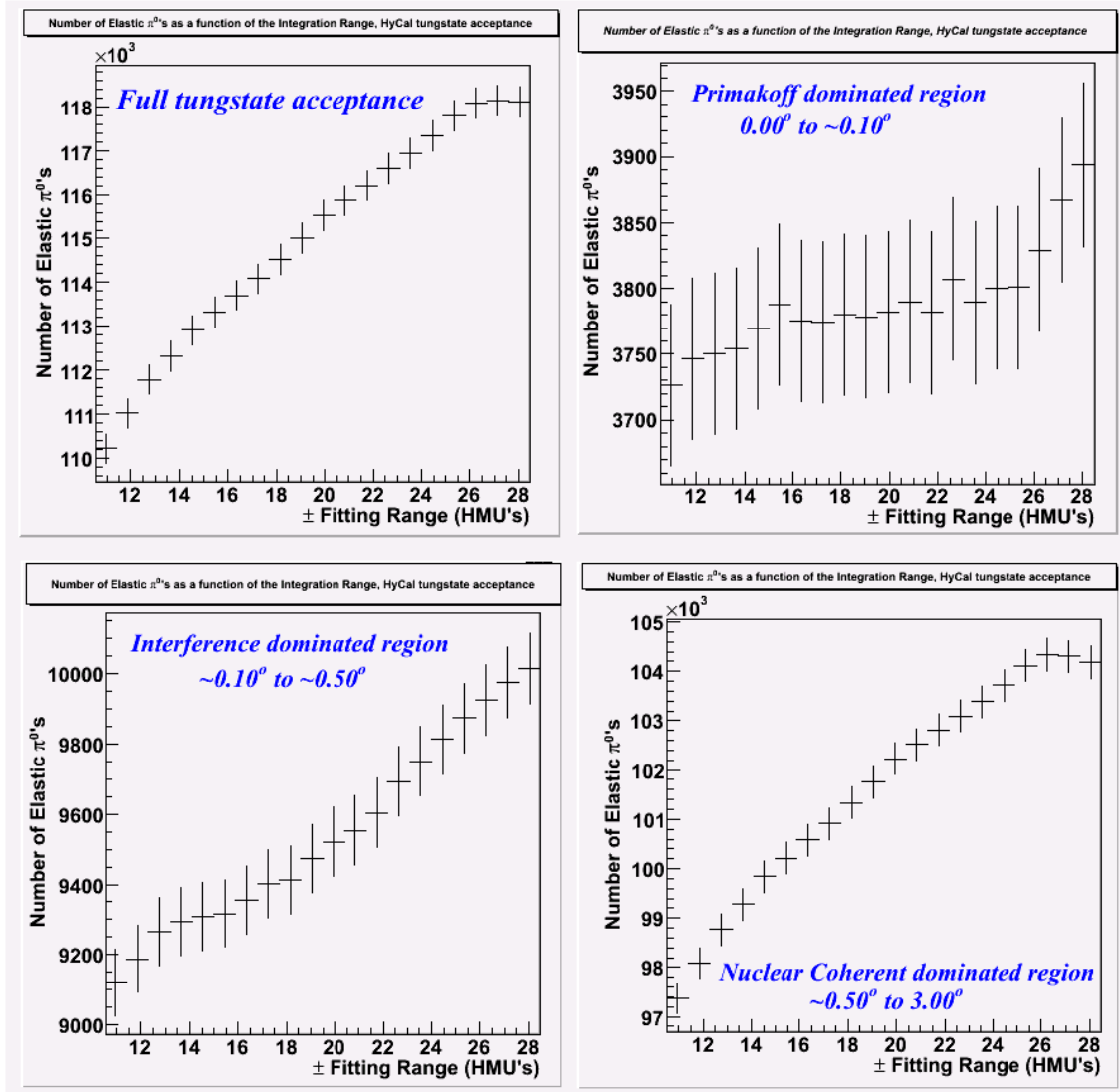


Figure 5.16: Elastic pion yield as a function of photonuclear process dominated angular regions and integration range

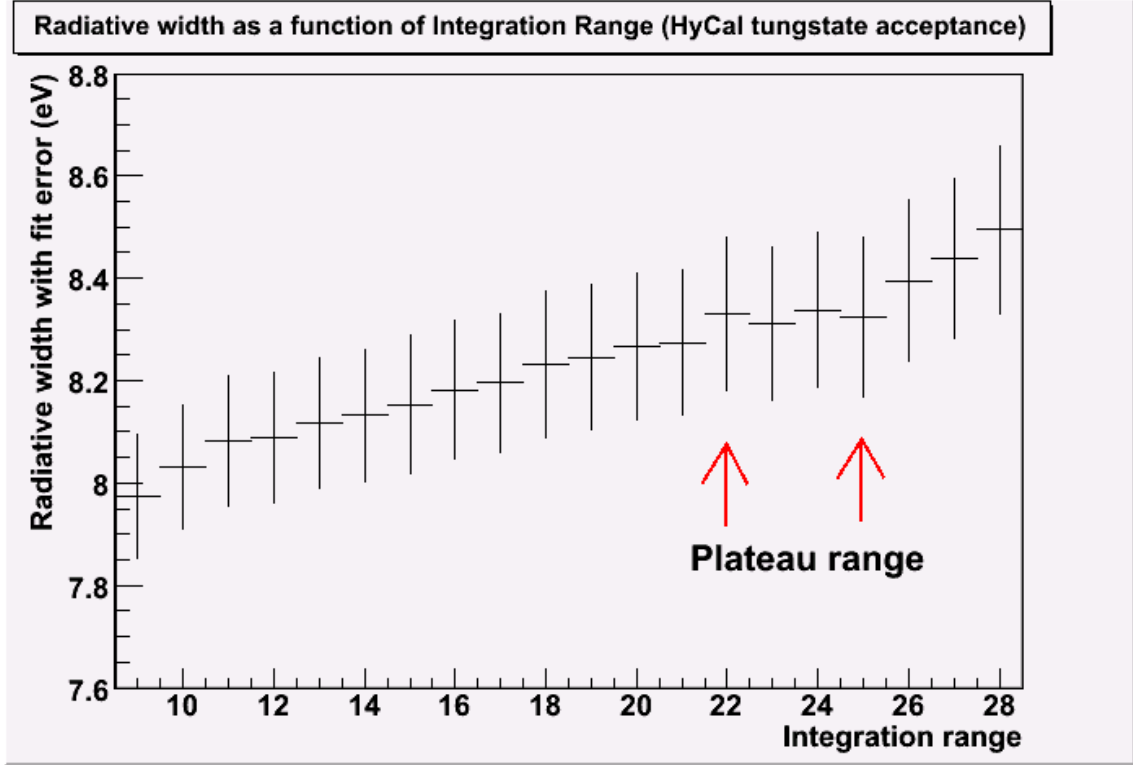


Figure 5.17: Radiative width as versus integration range

5.3.3.4 Background subtracted, in-time, elastic π^0 yields.

The state of the analysis is such that the π^0 candidate spectrums have been pared down to maximize signal and reject as much background as is feasible. Figure 5.11 showed sample fits in various photo-pion process dominated regions using the nominal signal and background lineshapes. Background subtracted yields as a function of π^0 angle, produced from the background reduced π^0 candidates spectrum, were also shown. The elastic yields in Figure 5.12 are not corrected for charge particle veto photon misidentification (see 5.6) or timing accidental suppression (5.3.3.1).

5.4 Systematic error in yield extraction method

An obvious concern regarding the yield extraction methodology is the amount of any systematic reconstruction software effects, signal enhancement, and model

dependence of the signal and background fitting. In order to gain an understanding of these issues, several studies were completed (Figure 5.18).

5.4.1 Systematic error in signal and background lineshape choice

To investigate any systematic effects in our method of yield extraction, various alternative lineshapes for both signal and background were considered (Figure 5.19).

Please note that the error bars for all “percent difference” plots is derived purely from the statistical error of the “nominal” value, unless otherwise noted. These error bars are included only to provide a context to the relative “strength” of the evaluated differences and how they may affect the radiative width extraction systematics. The following signal lineshapes and background models were used to investigate the yield extraction reliability.

- 1.) Double regular gaussians with a second order polynomial background (Nominal)
- 2.) Double regular gaussians with a third order polynomial background (Figure 5.19, upper left)
- 3.) Triple regular gaussians with a second order polynomial background (Figure 5.19, upper right)
- 4.) Triple regular gaussians with a third order background (Figure 5.19, lower right)

The purpose of this investigation is to ensure that enough degrees of freedom are employed in both the signal and background lineshapes. It is obvious from the behavior of the backgrounds (Figures 5.8 and 5.11) that at minimum a second order polynomial is required. A pair of normal gaussians has one more degree of freedom than a double tail skewed gaussian. By comparing the percent difference between the calculated

yields in each angular bin normalized to the first option above (double gaussian, third order polynomial), information regarding the required number of degrees of freedom for both the signal and background lineshapes emerged. The result of this study suggested that the first option (double gaussians with a 2nd order polynomial) does possess the fewest degrees of freedom required to model the signal and background spectrums.

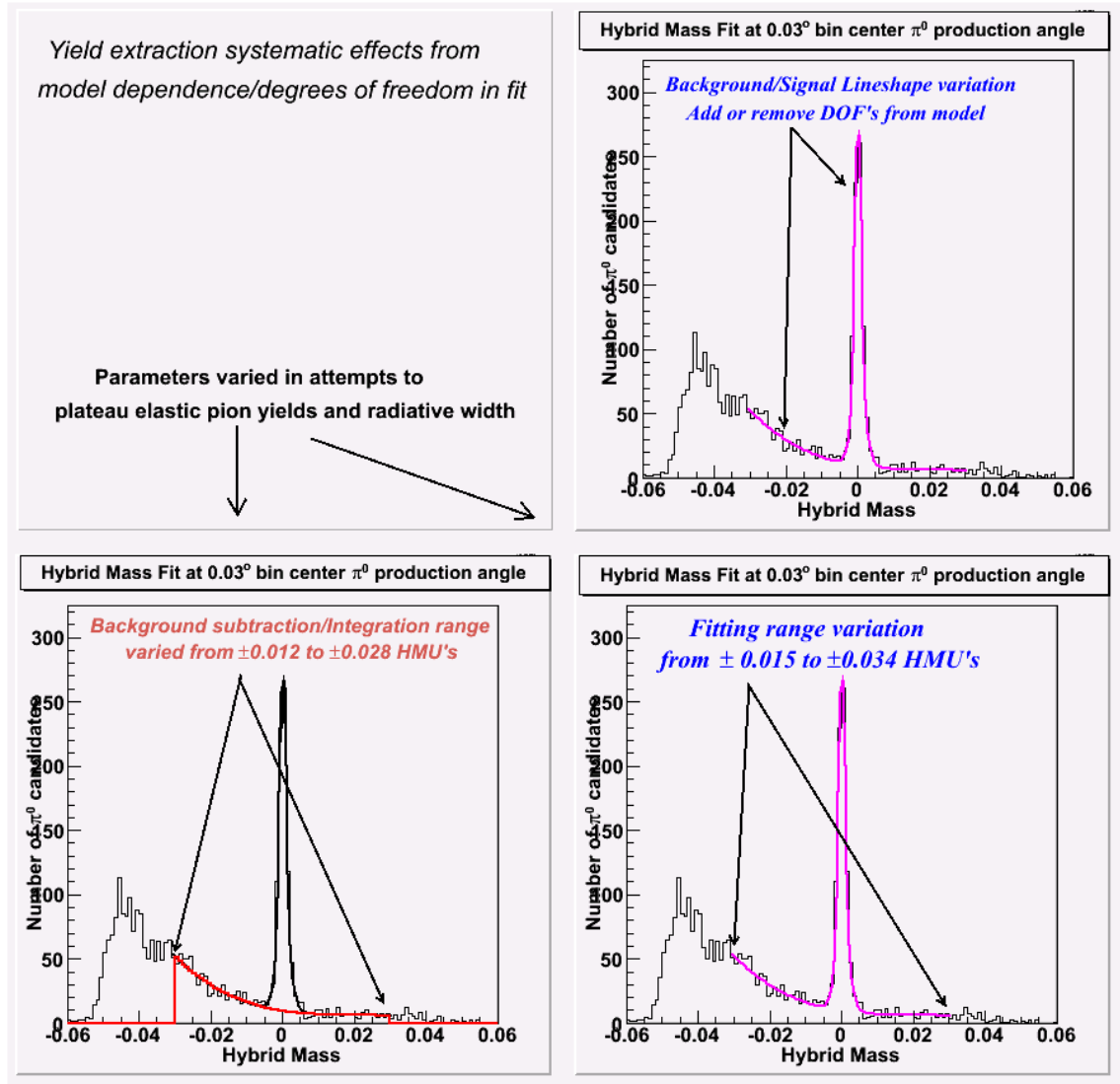


Figure 5.18. Graphical explanation of the parameters varied for elastic yield plateauing studies and the contributor to systematic effects in yield extraction methodology.

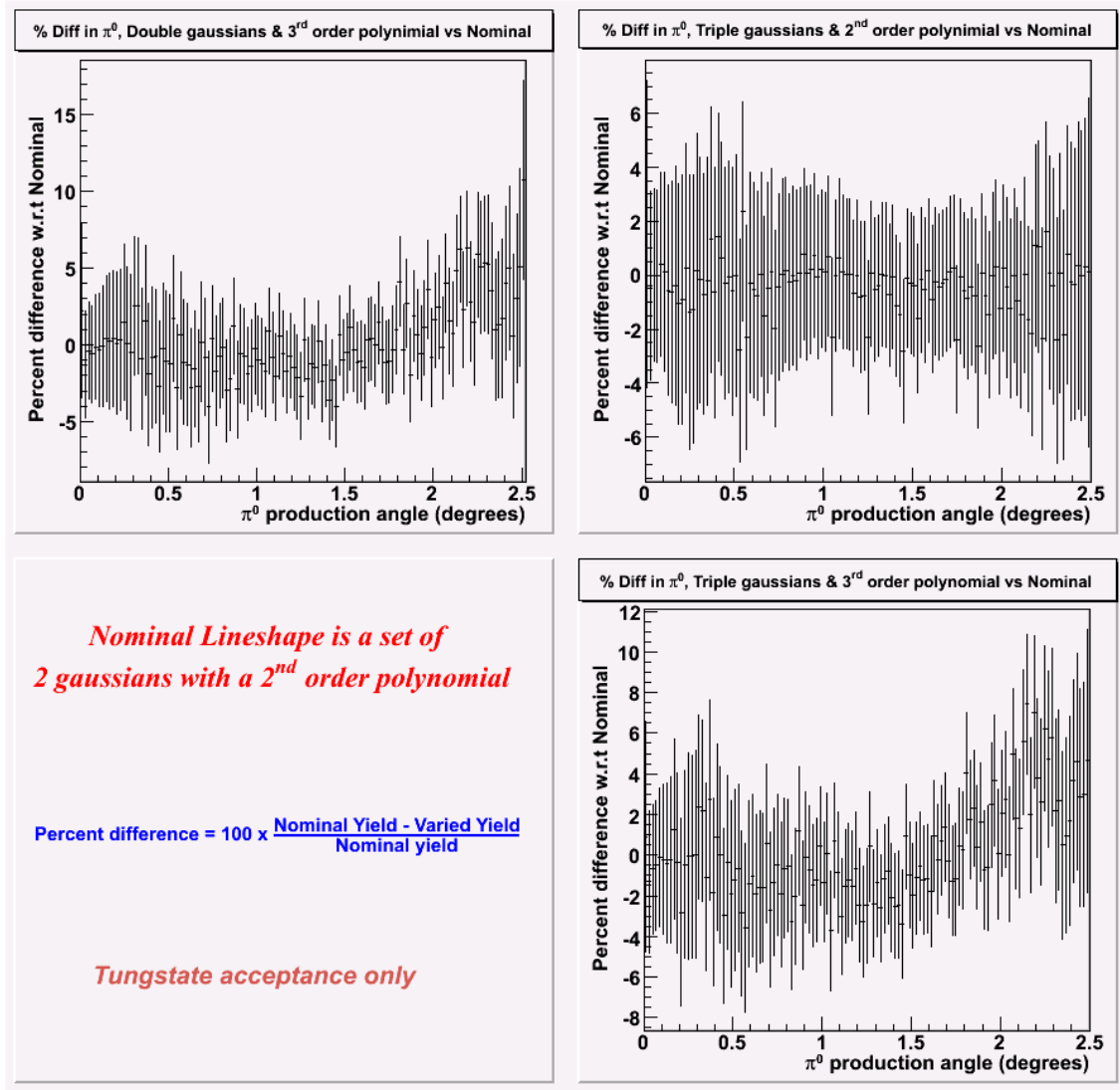


Figure 5.19: Comparing various lineshapes, all normed to double regular gaussians with a cubic background, HyCal tungstate acceptance

5.4.2 Systematic error from Hybrid Mass spectrum construction

We do not feel that the use of a Hybrid Mass or a rotation of the data introduces any additional systematic error in the analysis. Since the spectrums themselves are not altered in any way that changes the kinematics of the event, well understood background subtraction ranges and a solid understanding of background fitting

systematics can fully characterize systematic error in extracting yields from the Hybrid Mass spectrum.

5.4.3 Systematic error in cluster position finding algorithm.

Another source of systematic error can come from the cluster position finding algorithms. There are four main algorithms in PrimEx reconstruction software to reconstruct the location of the cluster center. The “Method 0” is a simple linear weighting of deposited energy in each detector to find the center of the cluster. The next, “Method 1” is a logarithmic weighting of the deposited energy. Method 2 is another linear weighting function that attempts to correct reconstruction effects due to finite cluster size and point of photon impact on the face of a detector. Method 3 is another improvement over Method 2. Method 4 is the averaging of Methods 1 and 3. This analysis has presented results using Method 3 exclusively. However, in order to evaluate systematic error due to cluster position finding methodology, extracted yields and radiative widths will be presented. In order to evaluate any systematic contributions due to differing cluster position finding methods, a well developed and understood simulation must be presented (see Chapter 6). Comparisons of the differing cluster position finding algorithms will be presented in Chapter 6, and systematic effects will be quantified in Chapter 7.

5.5 Yield extraction with full HyCal acceptance

While the lead glass detectors give a less precise result, their coverage of larger pion angles means we have a much improved access to the shape and size of the nuclear incoherent background. Hybrid mass spectra (Figure 5.20 and Figure 5.21) were of

similar shape and behavior to these constructed from the HyCal tungstate acceptance. While the elastic yields show a plateau (and accidental suppression = $3.60\% \pm 0.25\%$ of the elastic pion signal) as a function of the timing window (Figure 5.22), there are severe systematics present in the choice of background lineshape model (Figure 5.25). This renders any further consideration of the full HyCal acceptance for a precision measurement impossible. Significant detector upgrades, calibration improvement, and/or an alternative elastic pion yield extraction are required in order to incorporate the lead glass detectors. Sample elastic yields using the full HyCal acceptance (Figure 5.26) are presented only for qualitative purposes only. Nuclear incoherent photo-pion production becomes the dominant process at larger pion angle ($\sim 3.0^\circ$) and a substantial effort within the PrimEx collaboration is being made to better understand the nuclear incoherent cross section seen in HyCal. Yield extraction with the full HyCal acceptance provides solid physics input to this effort.

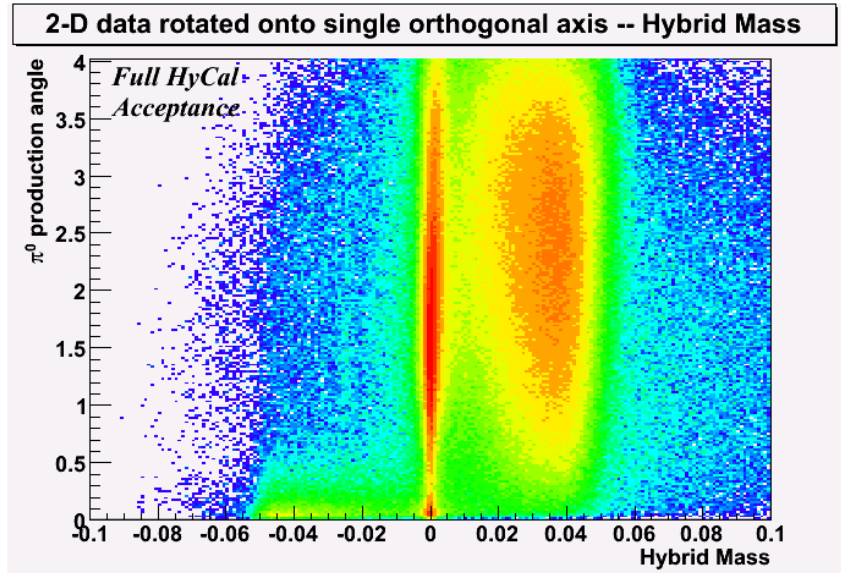


Figure 5.20: Projection of (entire HyCal acceptance) data onto the Orthogonal axis

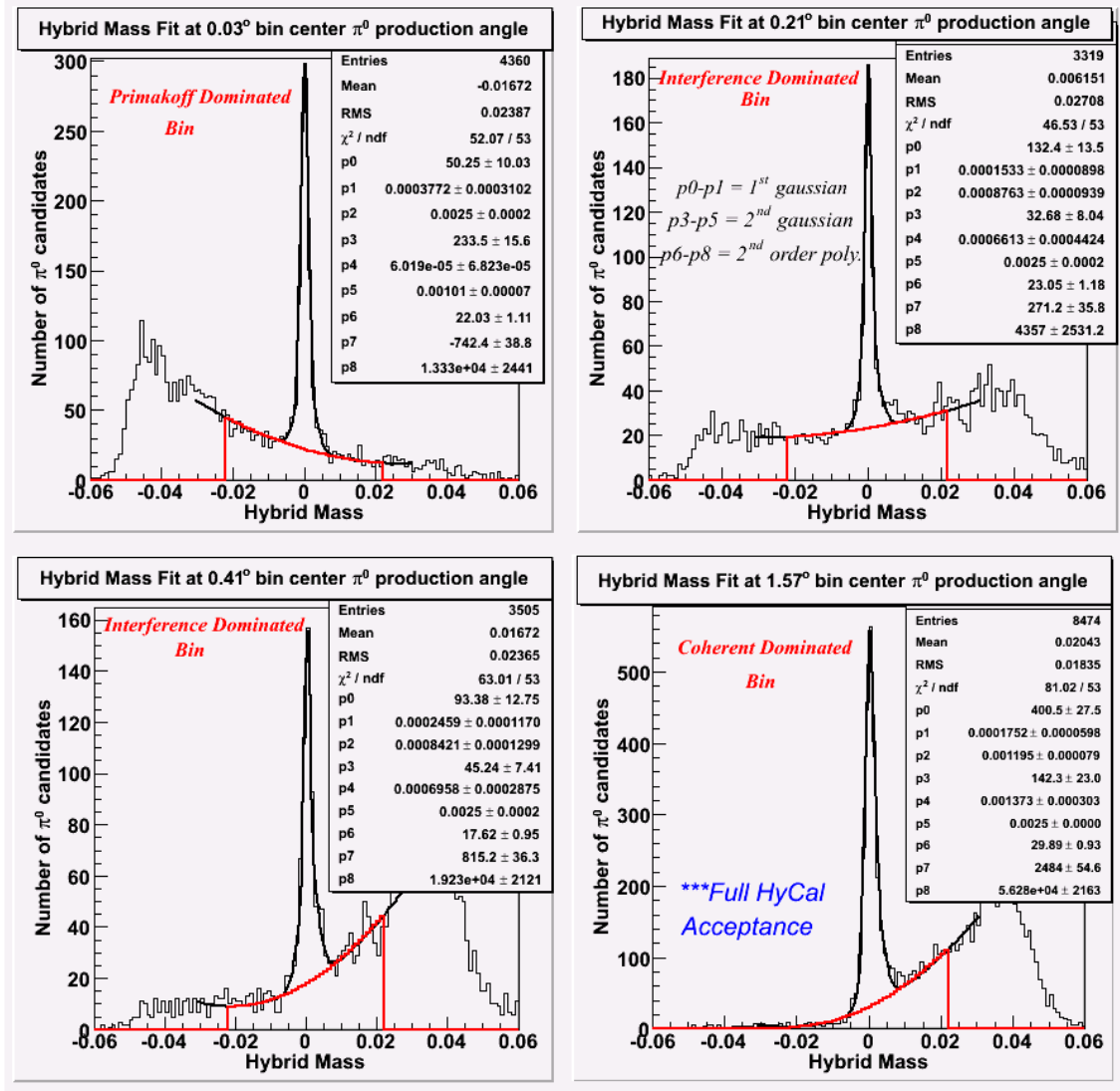


Figure 5.21: Sample Hybrid Mass fits using entire HyCal acceptance

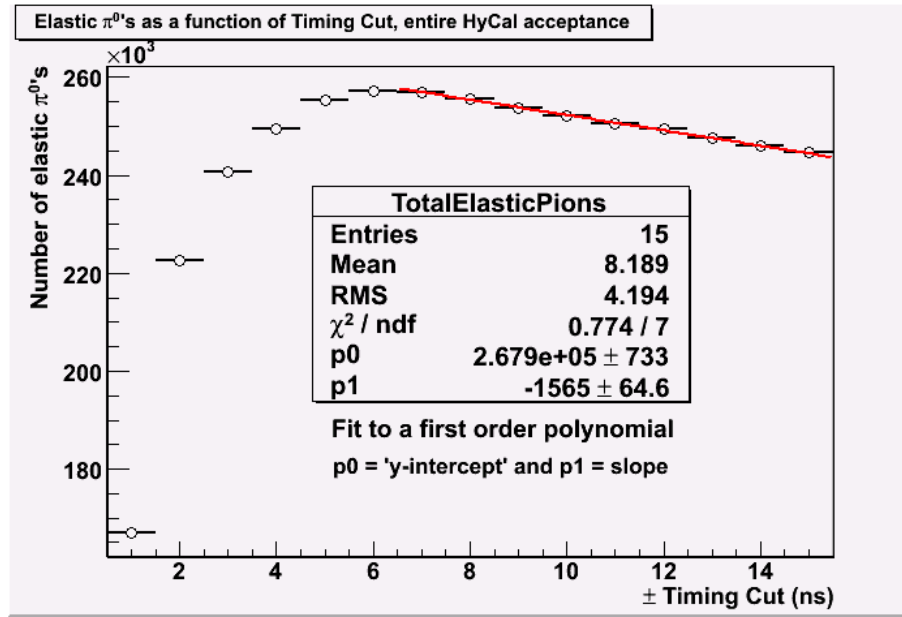


Figure 5.22: Elastic pion yield as a function of the timing window, entire HyCal acceptance.

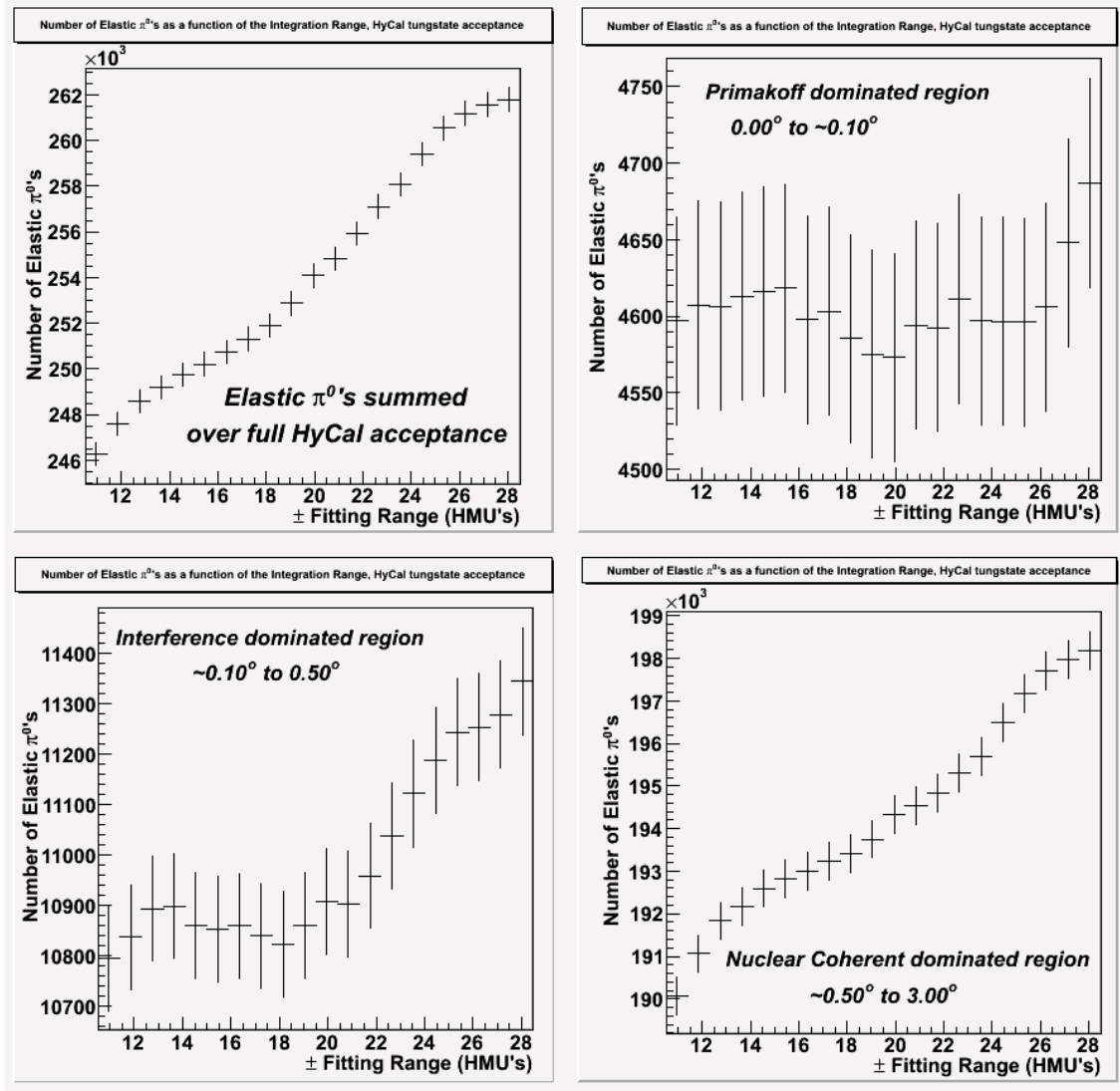


Figure 5.23: Elastic pion yield as a function of photonuclear process dominated angular regions and integration range, entire HyCal acceptance

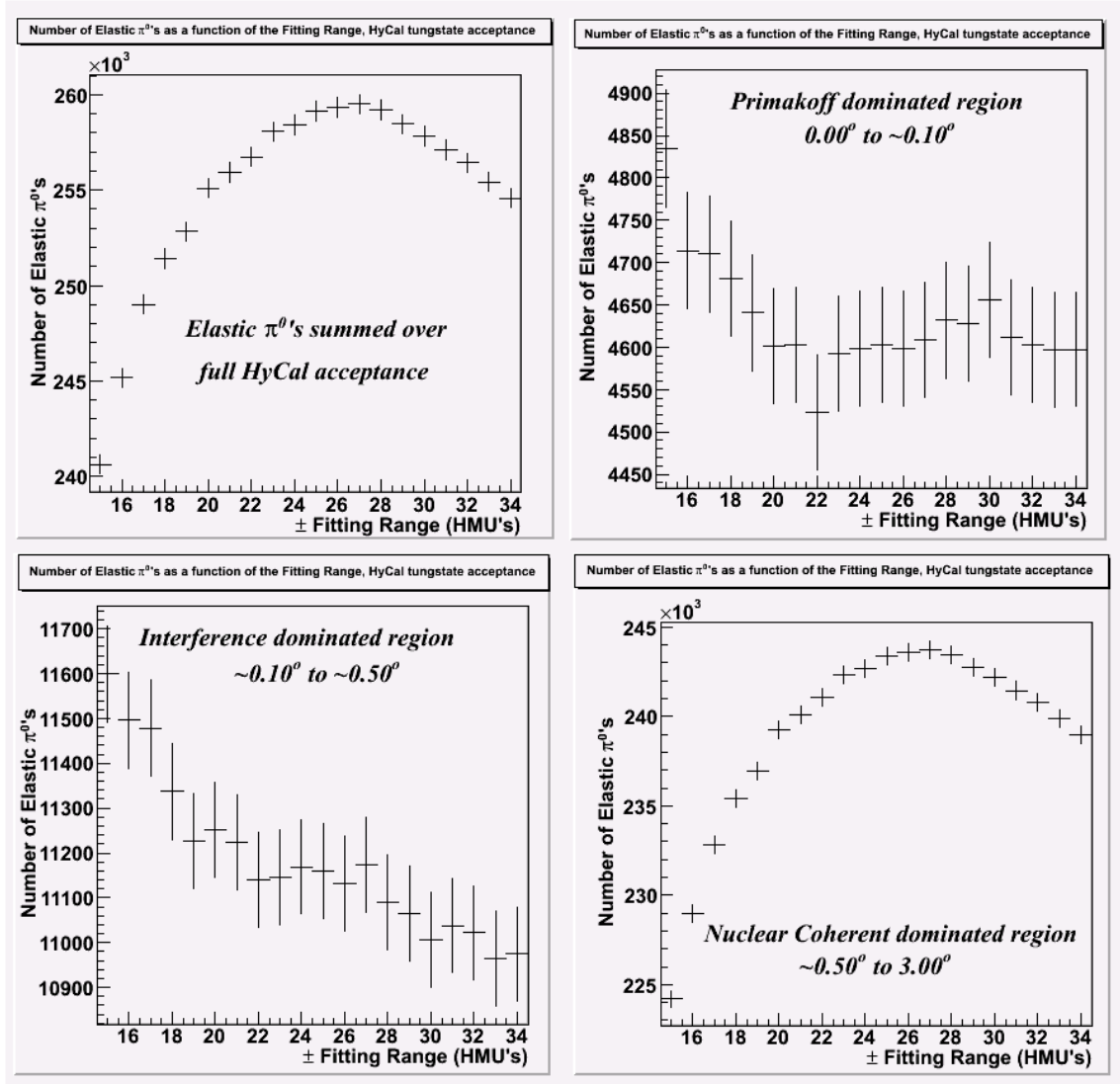


Figure 5.24: Elastic pion yield as a function of photonuclear process dominated angular regions and fitting range, integration range = 0.022 HMU's, entire HyCal acceptance

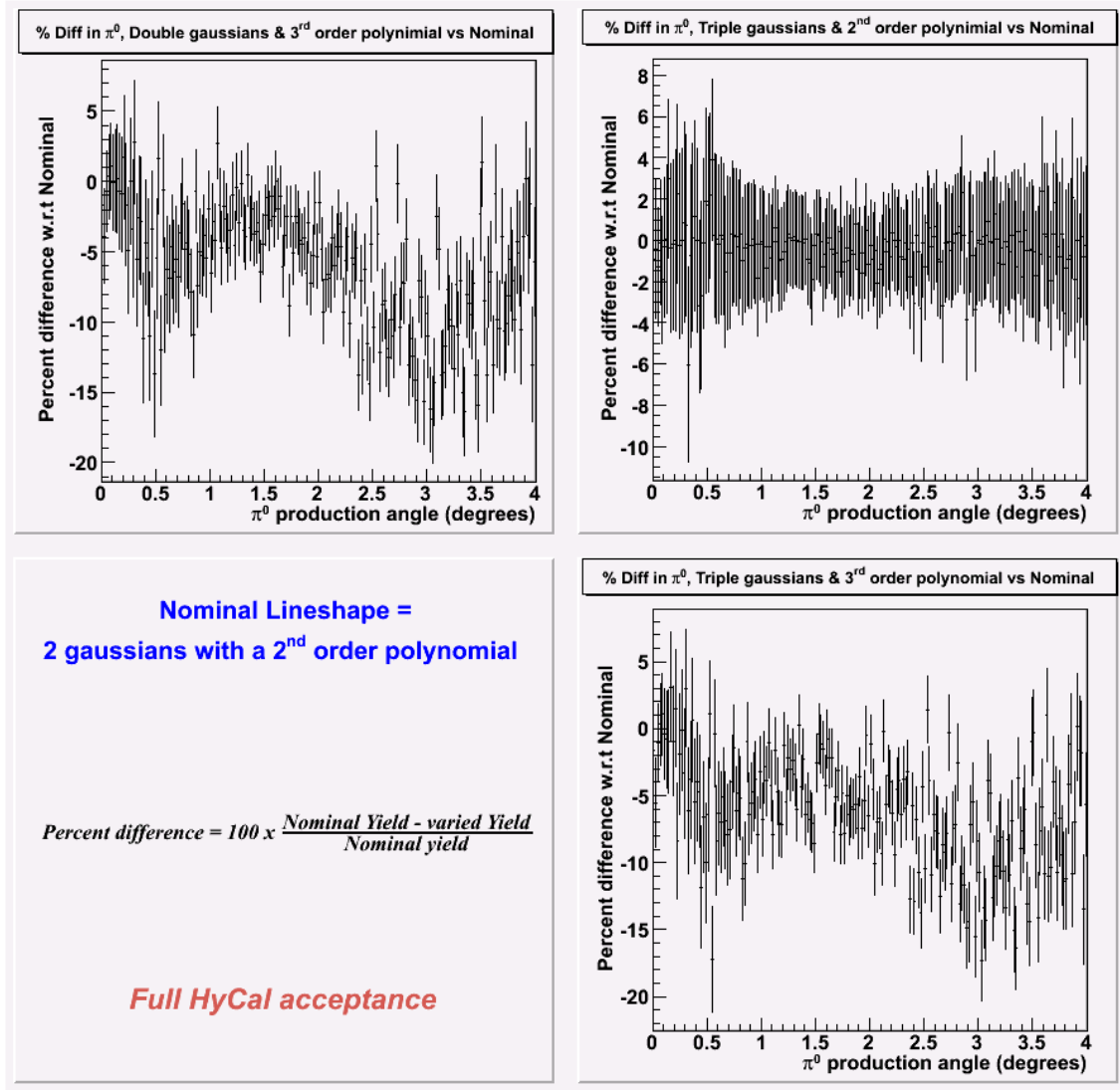


Figure 5.25: Comparing various lineshapes, all normed to double regular gaussians with a cubic background, full HyCal acceptance

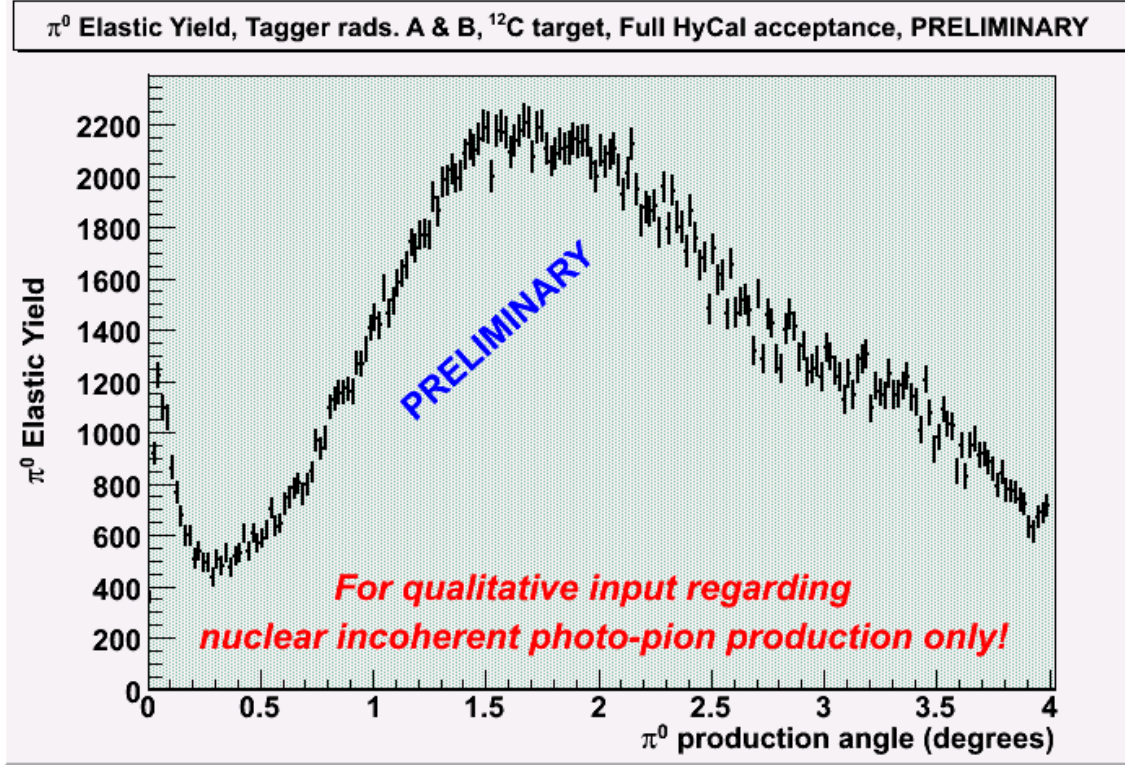


Figure 5.26: Elastic π^0 Yield, full HyCal acceptance

5.6 Yields, charged particle veto applied

Part of the PrimEx experimental set-up included a charge particle veto counters. A flag is available for use in the HYCALCLUSTER bank where any flag value over three (3) denotes a charge particle event. The HYCALCLUSTER bank contains the fully detailed and reconstructed clusters. A veto flag=3 indicates that the veto event has undergone time-walk correction, vertical and horizontal position matching, and ADC pedestal subtraction. The veto counters were constructed to have a roughly 1% photon conversion rate and commissioning of the veto confirmed this. This analysis will now include extracted yields using the HYCALCLUSTER veto flag to suppress some backgrounds. We define “photon misidentification efficiency” as the small chance that

a veto counter wrongly identifies a photon a charge particle during π^0 production data/analysis. We can access the misidentification efficiency two ways. The first method requires integration the π^0 candidate spectrum (before yield extraction) and identifying where the charged particle background is sufficiently small. The second method requires a comparison of the extracted π^0 elastic yields. The full HyCal (tungstate and glass) acceptance and original 20 ns time window is used for this analysis. This is justified because elastic yield extraction systematic effects will divide out in this study. Higher statistics and the ability to cover the entire π^0 angular range are added features to including the entire HyCal acceptance.

Figure 5.27 shows the effect of the charged particle veto on background at select angular bins. A strong suppression of the elastic background is noted. This is consistent with the long standing idea that the elastic background is from Compton events. The upper left corner of Figure 5.28 shows the percent difference of the integrals of the two π^0 candidate spectrums as a function of production angle. It is noted that almost all charge particle accidentals have stopped at roughly 2° . Projecting the data point past 2.0° into a histogram (lower left Figure 5.28) allows us to extract the photon misidentification efficiency (0.771%) during π^0 production, as well as an estimate of the systematic error addition to the extracted radiative width (0.077%) introduced when using the veto. This systematic error is calculated by dividing the mean of the fitted gaussian by the square root of the number of entries in the gaussian. Cluster position systematics divide out in this analysis, and there are no yield extraction systematic to be considered.

Alternatively, given the robustness of the yield extraction methodology, it is possible to extract a photon misidentification efficiency using the extracted yields. In this manner, it is possible to extend the analysis to smaller angles before large fluctuations in the extracted yields become apparent. These fluctuations are simply due to the large charged background at smaller production angles and statistical uncertainty in background subtraction. It should be noted that while the small angle fluctuations are comparatively large, they are almost all within the (non-vetoed) statistical error bars used in Figure 5.28 (upper right). A photon misidentification efficiency of 0.759% was calculated using extracted elastic yield comparisons from both 0° to 4° with an associated final systematic error on the extracted width of 0.054% (Figure 5.28, lower right). The consistency in these two efficiencies and the π^0 candidate method efficiency strongly suggests we can extract a reliable photon misidentification efficiency. Yield extraction systematics divide out in this analysis, as do cluster position systematics.

These photon misidentification efficiencies are smaller than the simple doubling of the single photon conversion efficiency of 1.0% measured during commissioning. This is easily explained. Commissioning occurred under “pristine” beam conditions for extracting single photon conversion efficiency. During π^0 running, there is a strong accidental background and sub-sequent stringent requirements on the kinematics are applied.

There was a concern that the veto counters nearest the beam may have different conversion efficiencies than other beam distant paddles. This would be due to the beam pass-thru notch cut into each veto counter. While a small effect (Figure 5.29) was noted, it is easily explained by higher charged particle statistics at small π^0 production

angles (and small incident angles). The small systematic uncertainty in employing the veto is more than made up by the improvement in the fit error on the radiative width.. Elastic π^0 yields with charge particle veto applied (Figure 5.12) can then be extracted, knowing the veto photon misidentification correction.

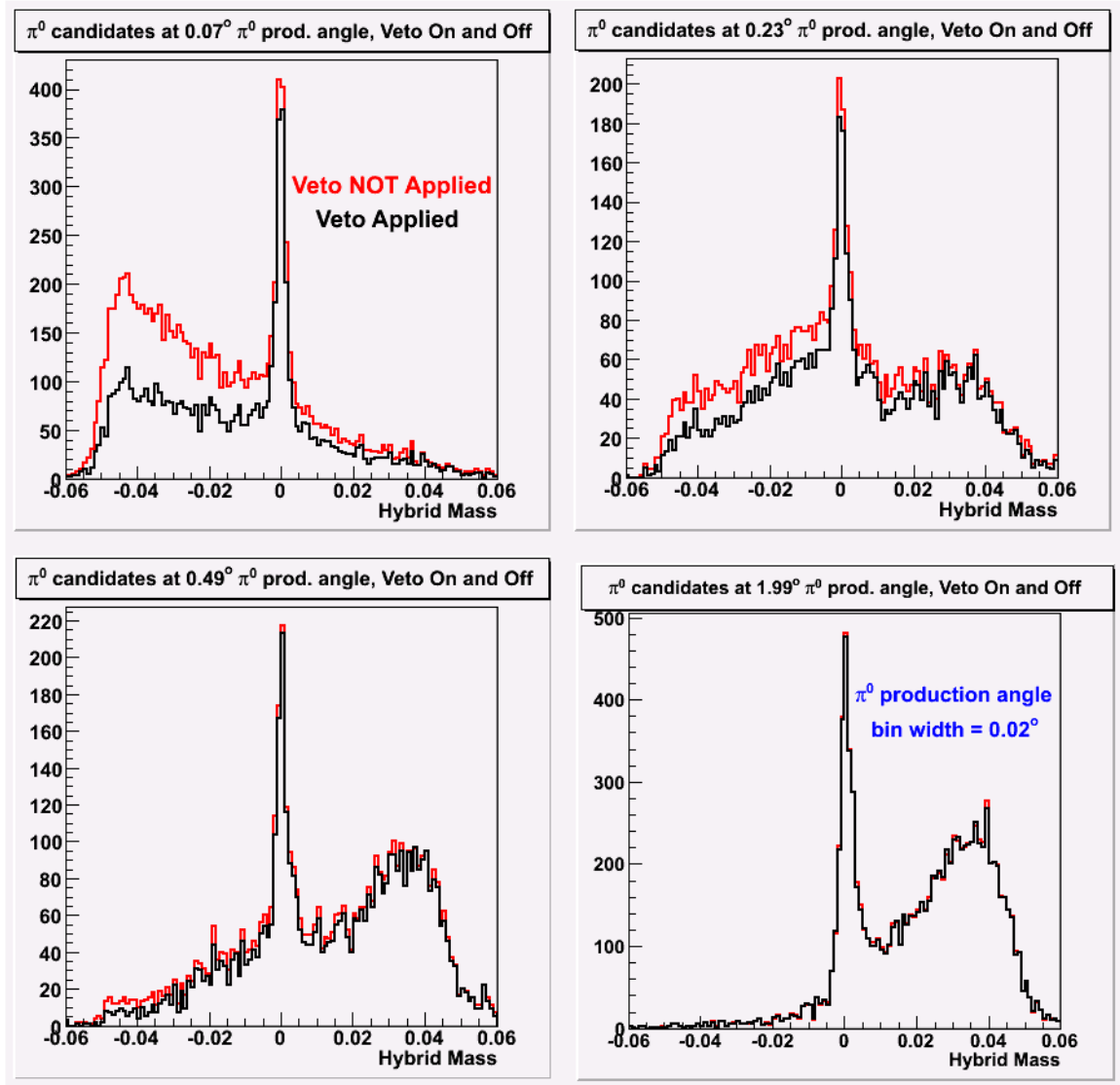


Figure 5.27: Effect of the Veto Counters on PrimEx π^0 candidate spectra.

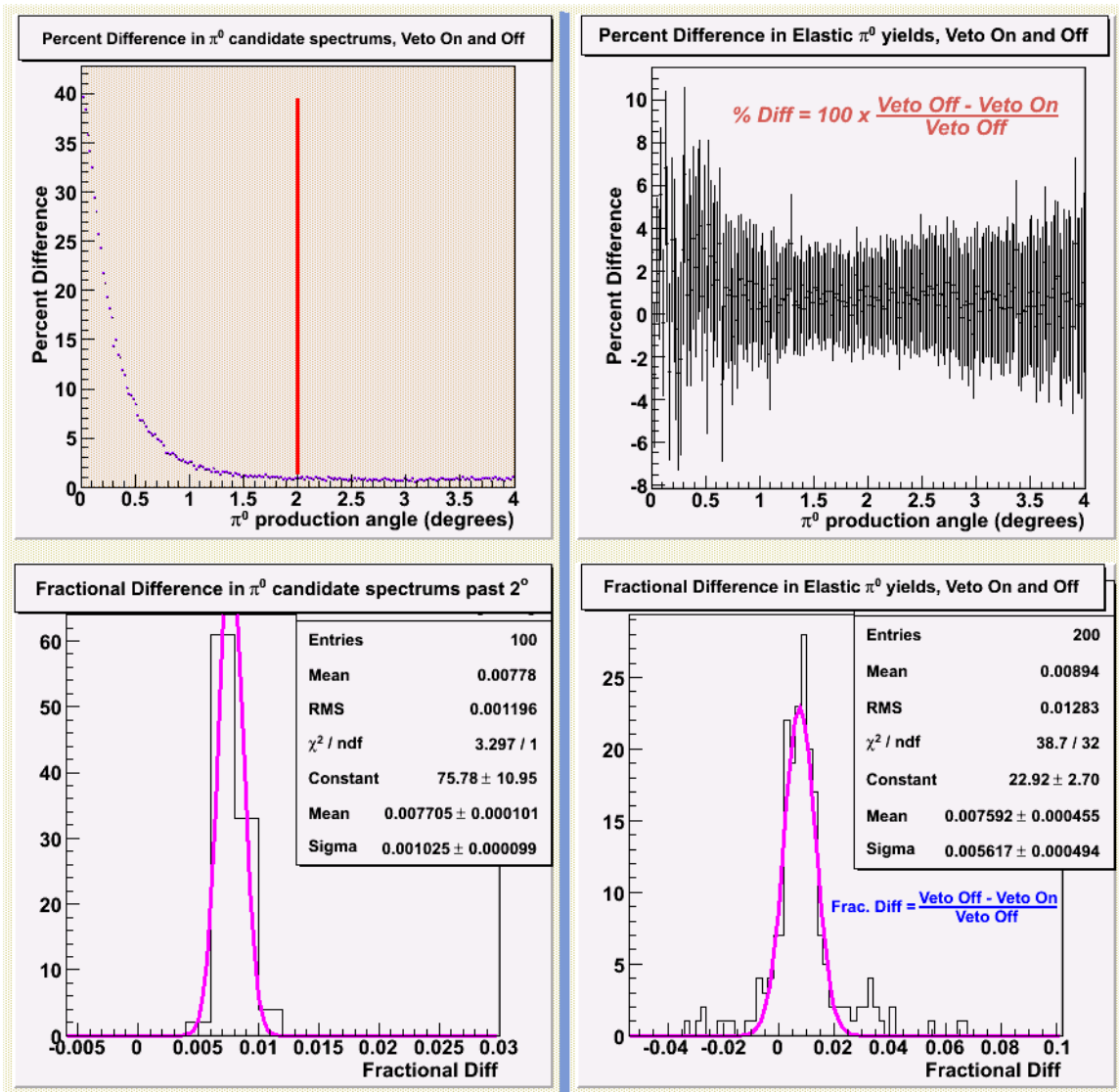


Figure 5.28: Extracting a “photon misidentification efficiency”

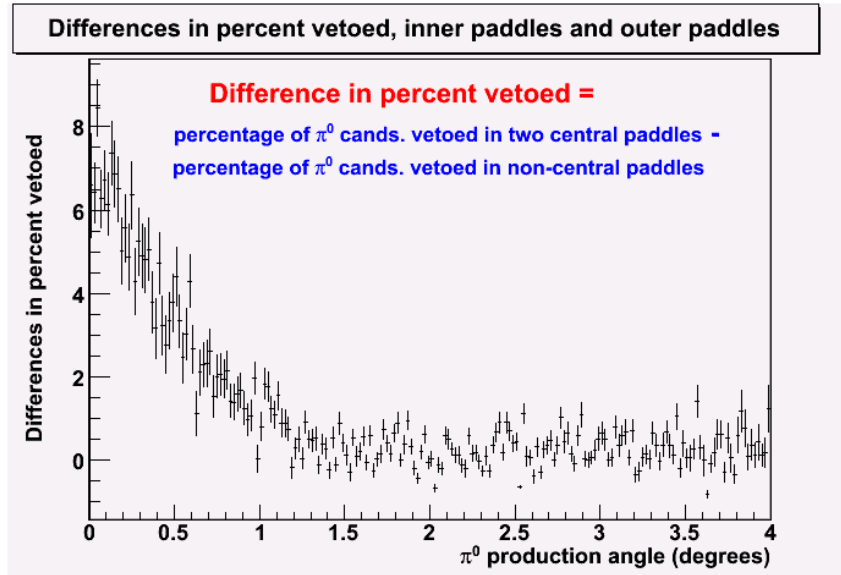


Figure 5.29: Notch effect, full HyCal acceptance

CHAPTER 6

PRIMEX MONTE CARLO SIMULATION DEVELOPMENT, RESULTS, AND OTHER EXPERIMENTAL INEFFICIENCIES

6.1 Monte Carlo location in the PrimEx software release

The standard PrimEx simulation software release has undergone a great deal of development and improvement for this analysis. This section will discuss those changes made specifically for this analysis and present results pertaining to geometric, resolution/reconstruction, and software cut efficiency corrections. A process for verifying the simulation as a valid representation of the experimental set-up has also been developed and will be presented here.

FORTTRAN generators for each neutral pion photo-production process (Primakoff, nuclear coherent, nuclear incoherent, and interference) were integrated into the simulation software. These generators are located in the file *src/programs/primsim/GENERATORS/MODULESpi0_c12_photoprod_roryF.f* and *src/programs/primsim/GENERATORS/MODULESpi0_c12_photoprod_rory.cc* is the C++ code which calls the FORTTRAN generator and channels the output into the rest of the simulation. The generator code also uses photon flux information (Figure 28) to properly scale the number of events thrown in each Tagger E-channel energy bin. The simulation code also models the physical photon beam spot size (Figure 4.***) and models the creation vertex z position based upon the target absorption and radiation lengths.

From Chapter 4, the total differential cross section, from Equation 4.2, can be expressed as

$$\frac{d^3\sigma}{d\Omega_\pi} = \frac{d\sigma_P}{d\Omega} + \frac{d\sigma_C}{d\Omega} + \frac{d\sigma_I}{d\Omega} + 2\sqrt{\frac{d\sigma_P}{d\Omega} \cdot \frac{d\sigma_C}{d\Omega}} \cos(\phi_1 + \phi_2),$$

and the Primakoff (Equation 4.1), Nuclear Coherent (Equation 4.3) and Nuclear Incoherent (Equation 4.4) are

$$\frac{d^3\sigma_P}{d\Omega} = \Gamma_{\gamma\gamma} \frac{8\alpha Z^2}{m^3} \frac{\beta^3 E^4}{Q^4} |F_{e.m.}(Q)|^2 \sin^2 \theta_\pi,$$

$$\frac{d\sigma_C}{d\Omega} = C \cdot A^2 |F_N(Q)|^2 \sin^2 \theta_\pi,$$

$$\frac{d\sigma_I}{d\Omega} = \xi A(1 - G(Q)) \frac{d\sigma_H}{d\Omega},$$

respectively. Final state interactions have been corrected for realistic nuclear charge distributions [19 & 24] and the Glauber theory regarding the Nuclear Incoherent [25, 27 & 27].

6.2 Energy leakage correction, tracking threshold study, resolution tuning

The goal of any simulation is to model the physical experimental set-up as accurately as possible. Several areas of the simulation required tuning. The three “knobs” turned to tune the simulation corrected energy leakage from the simulated detector, the GEANT tracking threshold energy, and the mass resolution. Another study investigated the accuracy of simulation geometry and applicability of the simulation to experimental four vectors from PrimEx data. A final study investigated resolution effects with a non-functioning fiducial detector.

6.2.1 Energy leakage correction

In the physical HyCal and the simulated HyCal total containment of the cluster energy is not perfect. Energy is lost out the back of the crystals and glass blocks, within the airgap and wrapping, and in absorption in the detector material itself (Figure 6.1). Additionally, the clustering algorithm also misses about 2-3% of the deposited energy due to the finite size of the cluster mask. This occurs in both physical data (Figure 6.2) and simulation (Figure 6.3). The physical HyCal has calibration constants which take these energy leakages into effect. The simulated HyCal also needed a global calibration constant to correct for the sources of energy leakage in the simulation. A global multiplicative factor for the simulated energy deposited in HyCal of 1.11 for lead tungstate and 1.10 for lead glass detectors pushed the simulated mass spectrum centroid very close to 0.135 GeV. This calibration also pushed the Elasticity to within 2% of the nominal value of '1'. This global energy loss correction was implemented in

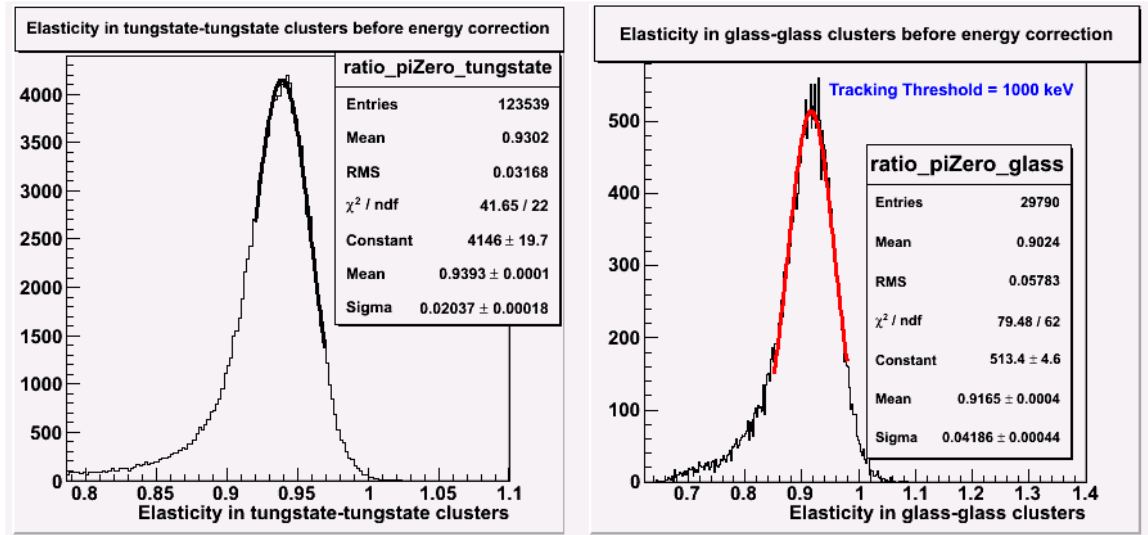


Figure 6.1: Ratio of HyCal Cluster pair energy and Thrown Photon energy -- Simulation

psim_digitize. The justification for using a global energy loss correction is in Figure 6.4, since energy deposition is flat as a function of thrown photon energy, reconstructed cluster position, and reconstructed π^0 production angle.

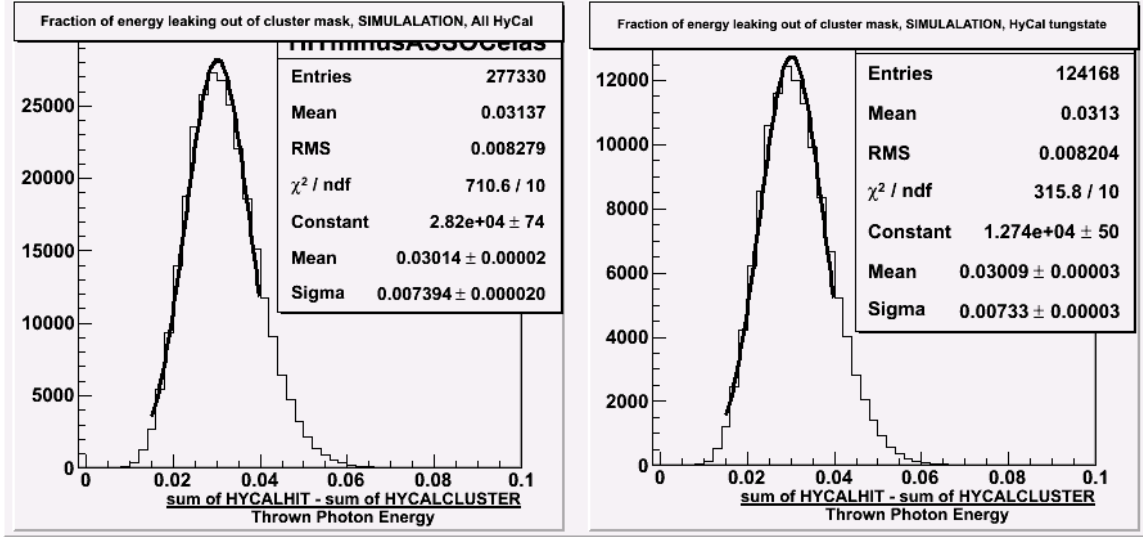


Figure 6.2: Ratio of energy not contained in cluster pair (but deposited in HyCal) and Thrown Photon energy – Simulation, *after energy correction and tracking threshold tuning*, all HyCal (left) Tungstate detectors only (right)

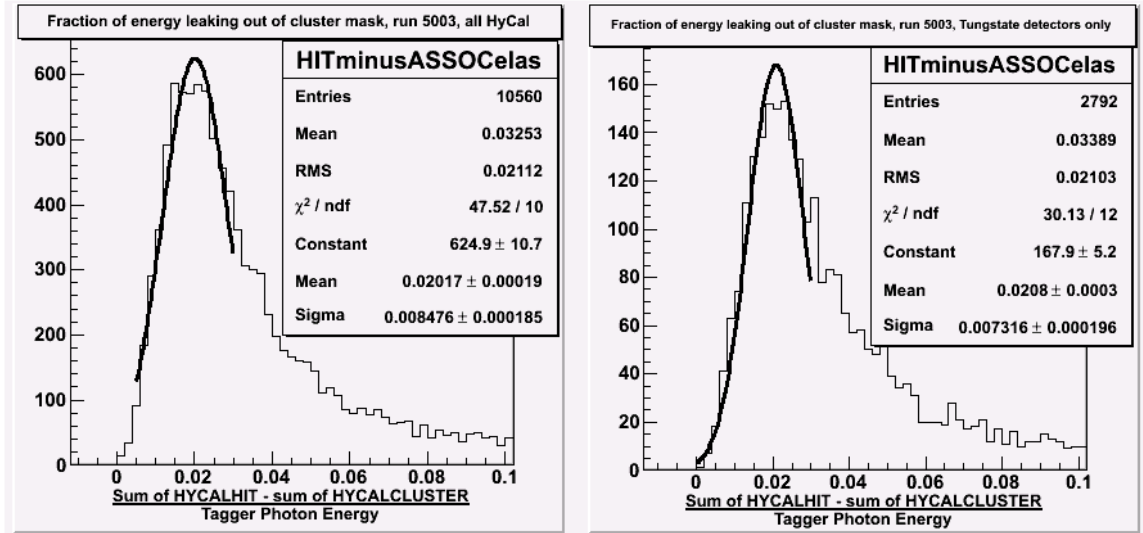


Figure 6.3: Ratio of energy not contained in cluster pair and Thrown Photon energy – Physical Data. Used “most likely” event, only 2 cluster events, All HyCal (left) Tungstate detectors only (right), run 5003

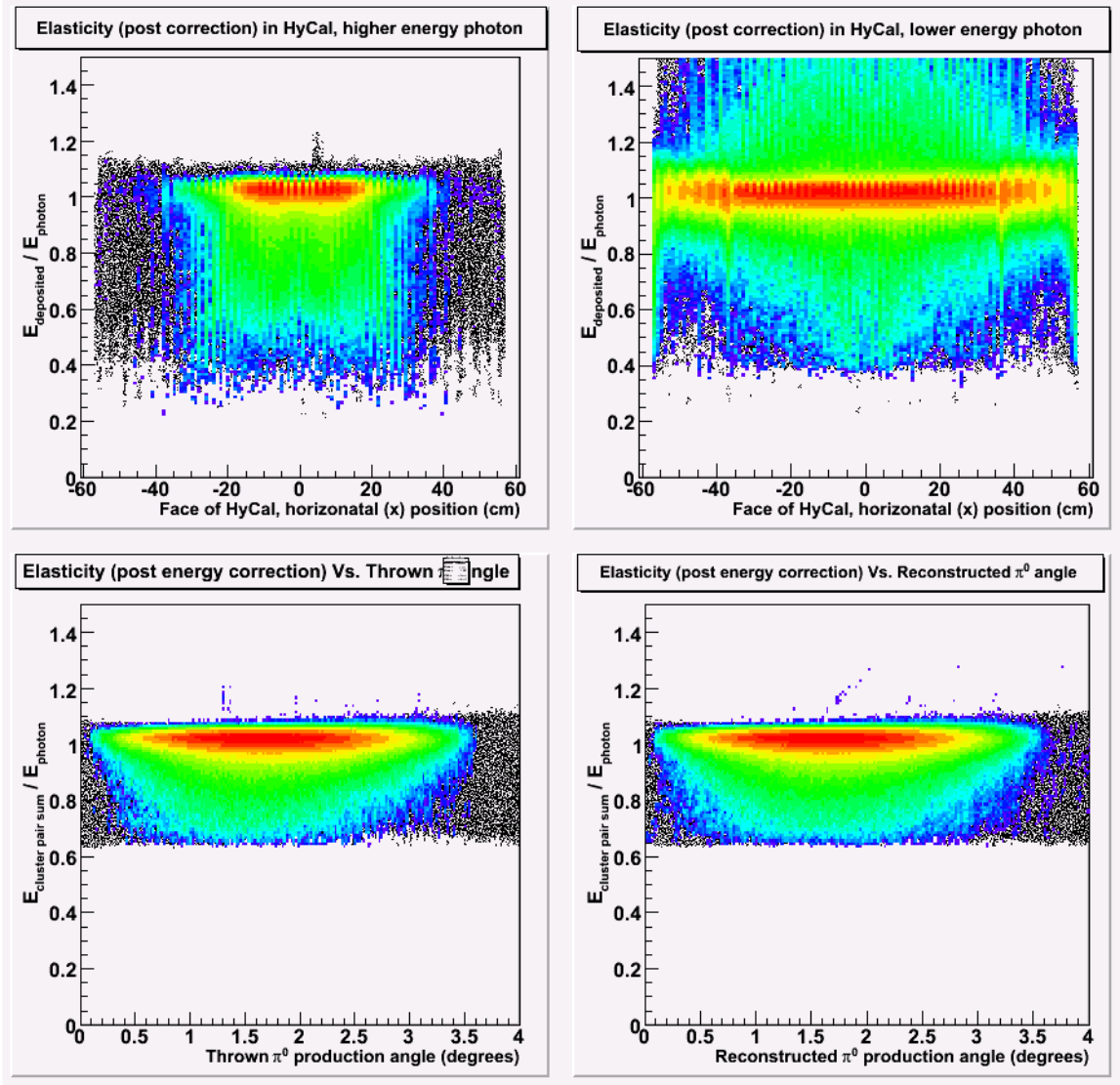


Figure 6.4: Elasticity (post energy correction) as a function of reconstructed ‘X’ position of cluster for both high and low energy decay photons. (Reconstructed ‘Y’ is identical), Thrown production π^0 angle, and reconstructed π^0 production angle.

6.2.2 GEANT tracking threshold in HyCal.

The GEANT tracking threshold energy helps to determine shower size by truncation of the shower development once a secondary particle falls below the threshold. Too large of a threshold and the shower size (i.e. the number of crystals in a shower) is too small. Too small of a threshold and a lot of computer time is wasted.

The default threshold in GEANT is 1 MeV. Comparisons of Figure 6.5 through 6.9 suggest that 100 keV is an appropriate threshold for *primsim* to use given the 1% or better agreement with physical data's reconstructed mass centroid (Figure 6.5 and 6.7). Additionally, the close agreement between physical and simulation data (Figure 6.2 and 6.3) strongly suggests that shower development in simulation is well modeled.

6.2.3 Invariant mass resolution tuning

Lastly, the widths of the mass and elasticity distributions were tuned in *psim_digitize* by hand to within a few percent of the physical data values for mass and elasticity. Figures 6.6 and 6.9 also show the results of tuning the widths of these spectrums.

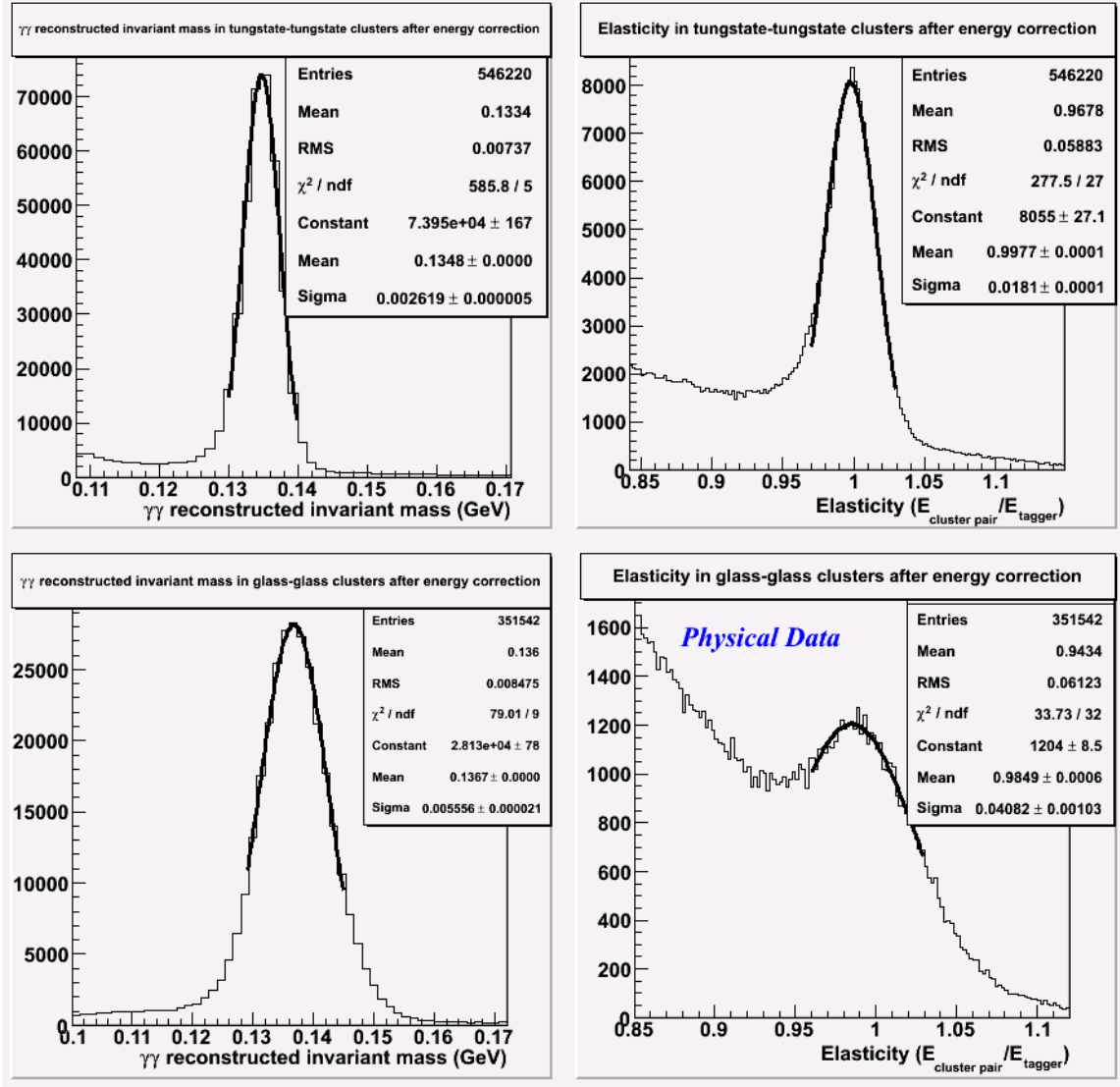


Figure 6.5: Invariant Mass and Elasticity Spectrums for all physical data, no event likelihood selection

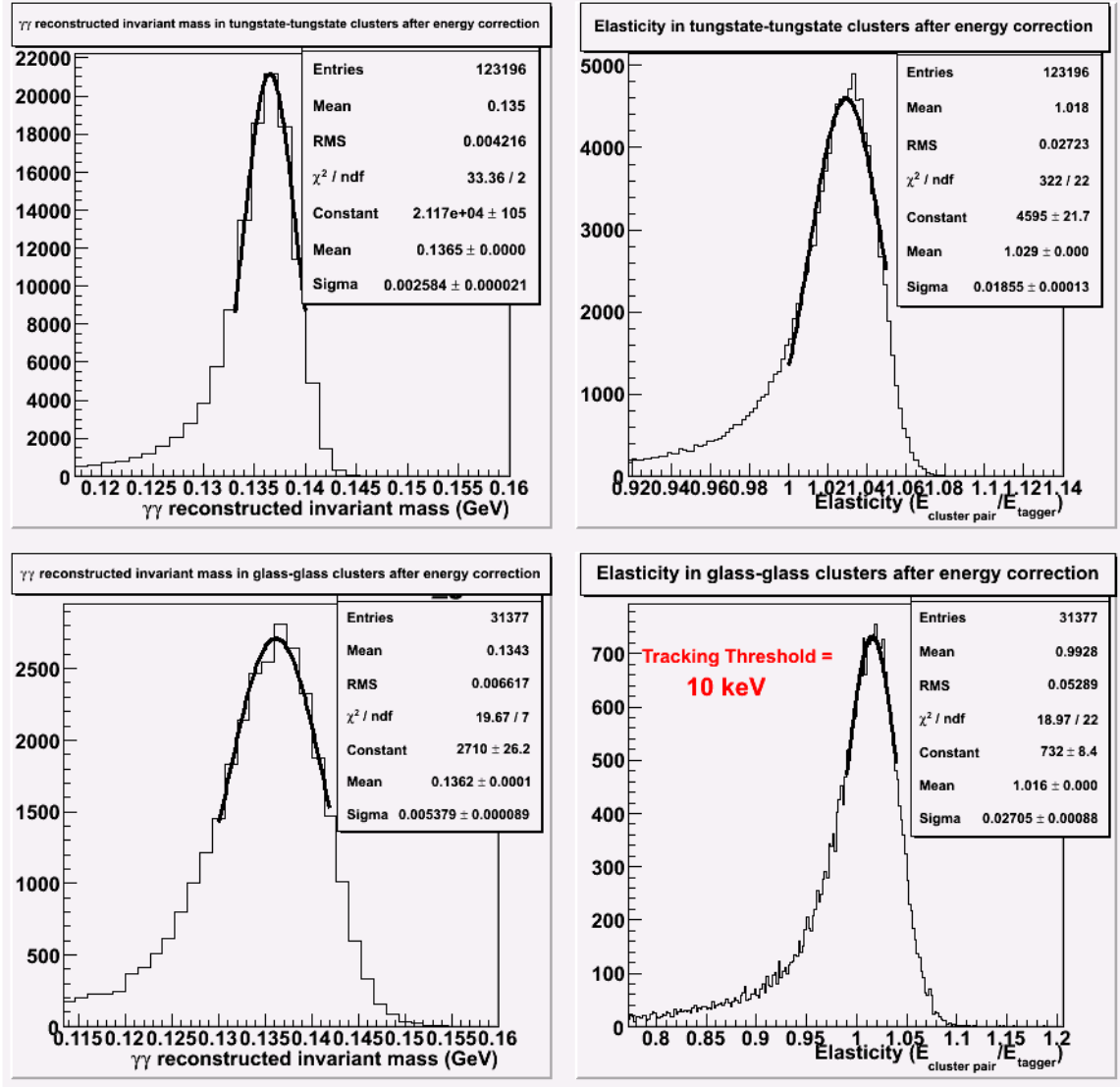


Figure 6.6: Invariant Mass and Elasticity spectrums for tracking threshold of 10 keV. Resolution has also been tuned to physical spectrum

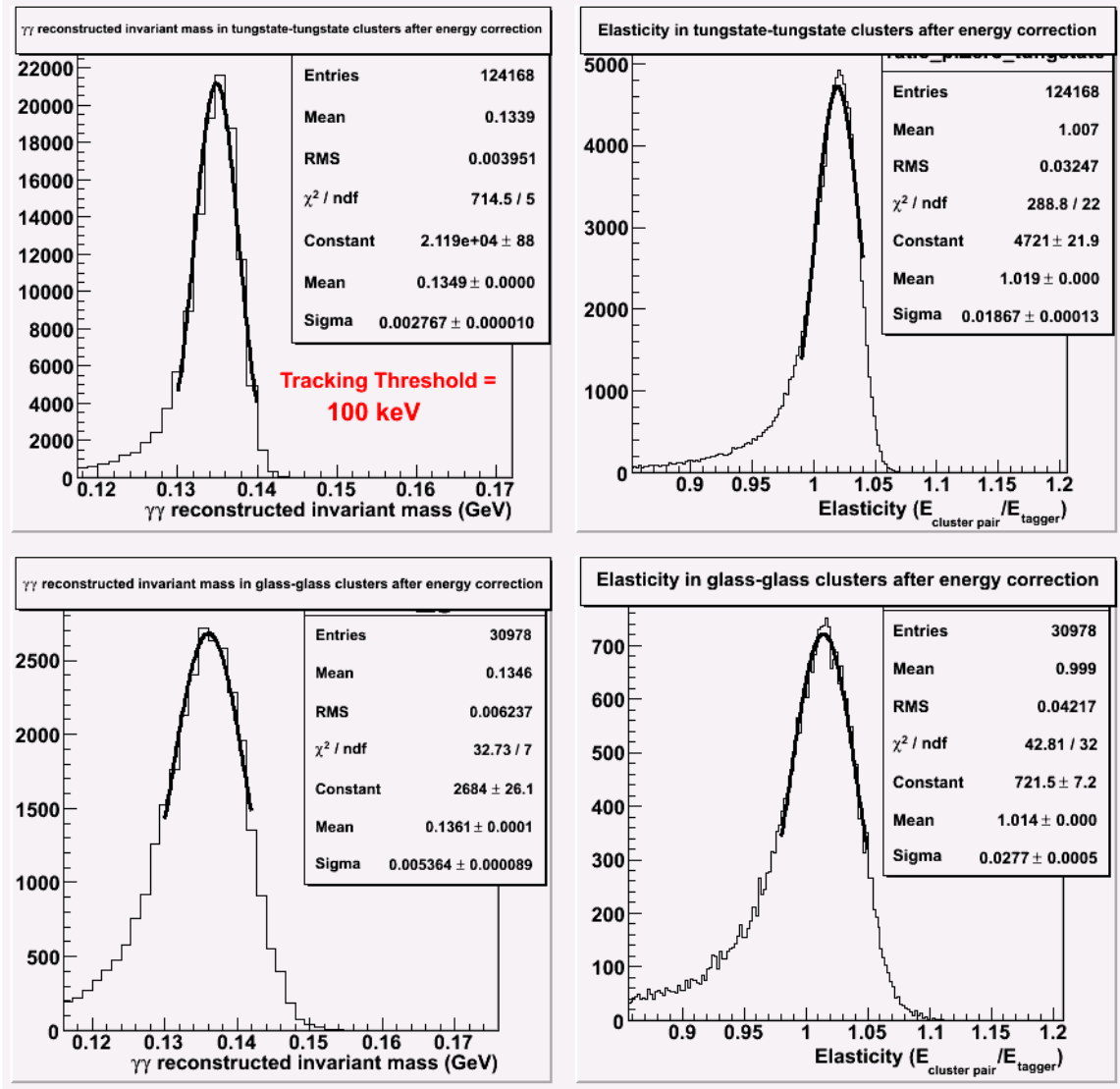


Figure 6.7: Invariant Mass and Elasticity spectrums for tracking threshold of 100 keV. Resolution has also been tuned to physical spectrum

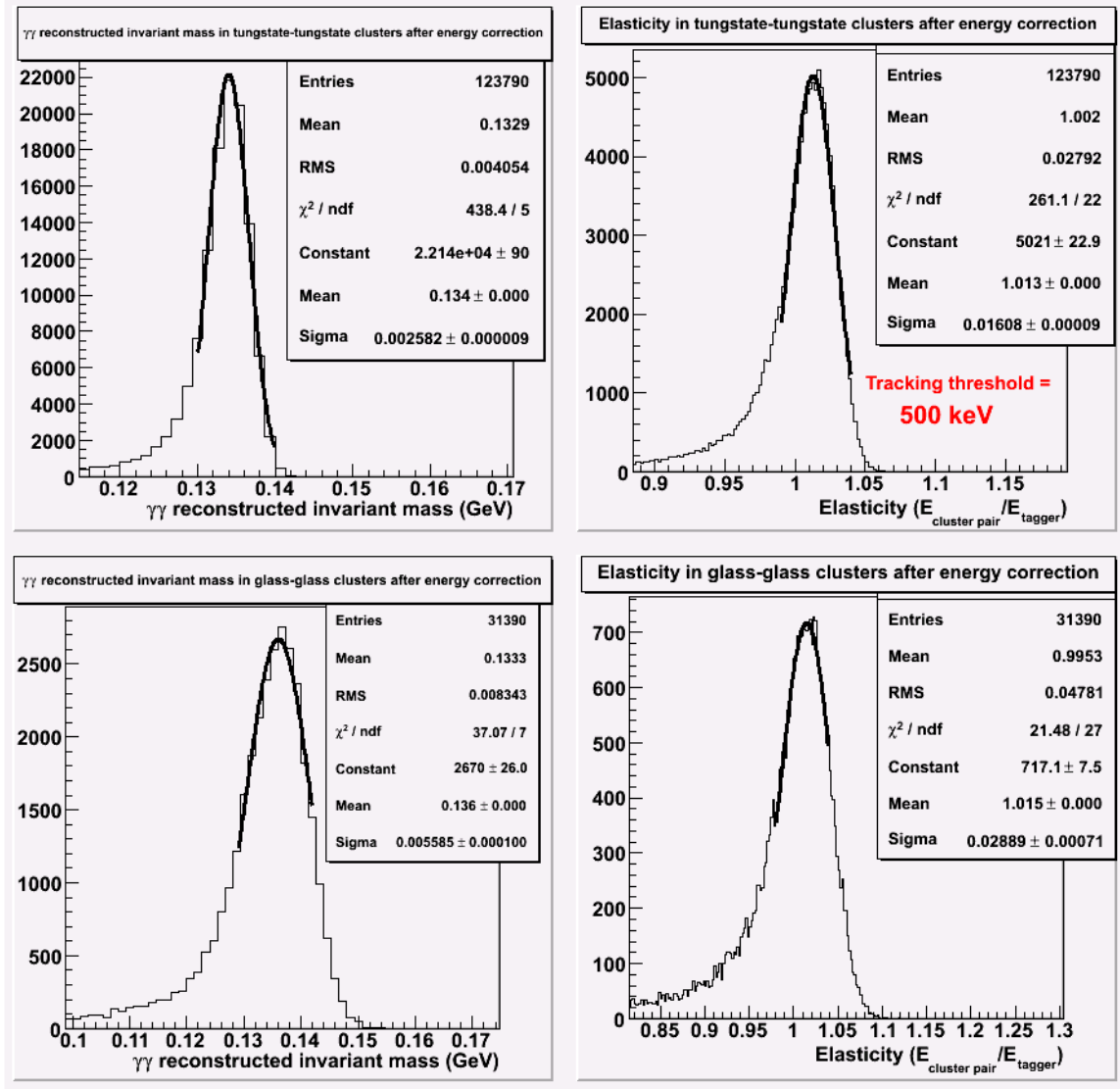


Figure 6.8: Invariant Mass and Elasticity spectrums for tracking threshold of 500 keV. Resolution has also been tuned to physical spectrum

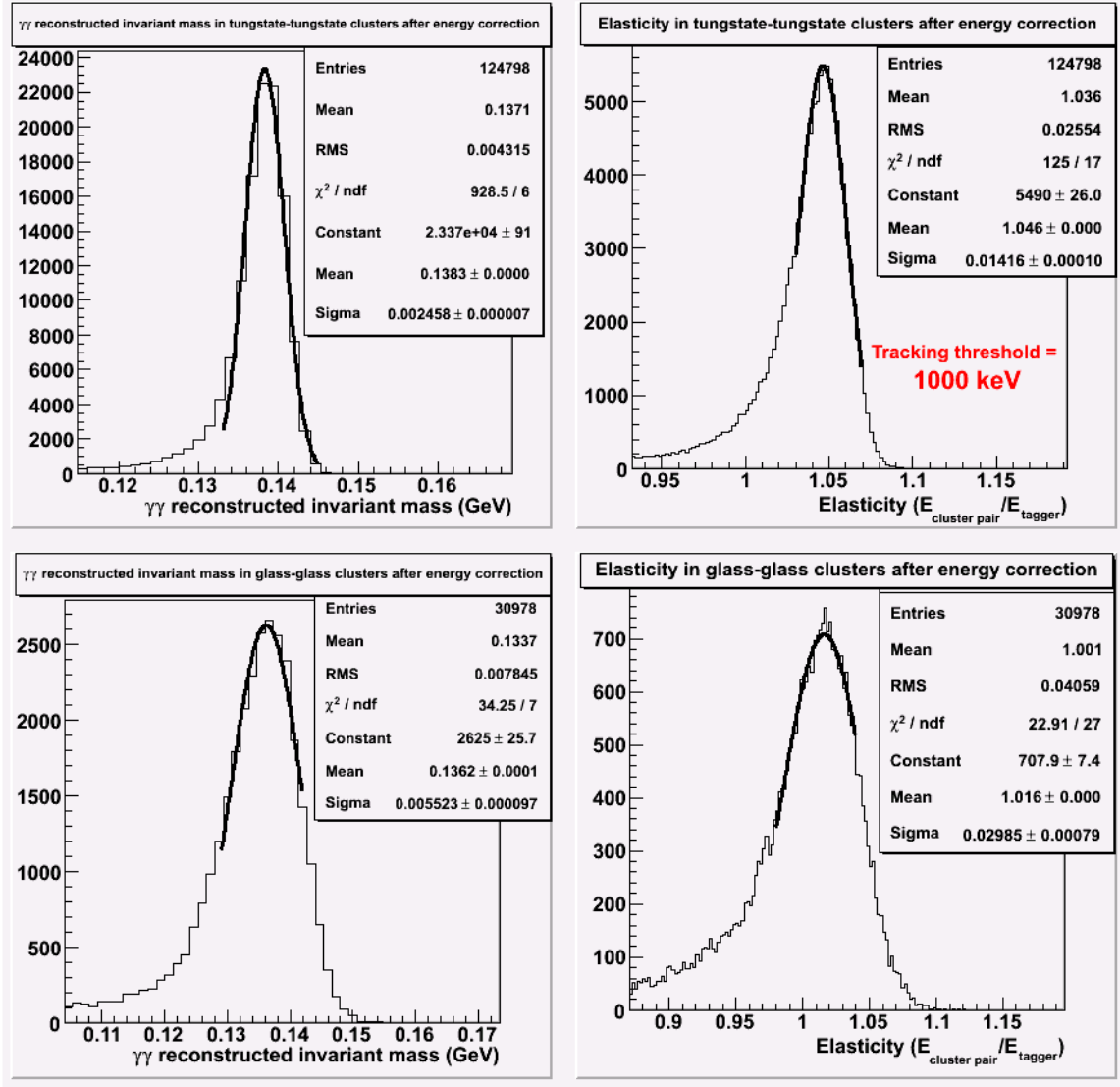


Figure 6.9: Invariant Mass and Elasticity spectrums for tracking threshold of 1000 keV. Resolution has also been tuned to physical spectrum

6.3 Geometric, reconstruction/resolution, and software cut efficiency calculations

The simplest efficiency calculation is to ask if a thrown event reached HyCal.

The only angular information considered is the thrown π^0 production angle.

$$\text{Efficiency (thrown angle)} = \# \text{ of events detected at HyCal} / (\# \text{ thrown in that bin}) \quad (7.1)$$

No information regarding the reconstructed production angle at HyCal is considered.

This is what we call geometric acceptance. We have calculated geometric efficiency

using decay photon angular information to determine if a photon will hit HyCal (Figures 6.10 and 6.11). We are including this data only for comparison to other collaboration analyses. This geometric acceptance is consistent with other acceptance studies where final state photon absorption losses are modeled (Figure 6.12 and 6.12). However, this simulation has a lot of HyCal information, and consistency of efficiency calculation is preferred. Thus, any “geometric efficiency/acceptance” mentioned later in the text will include all incident and exiting photon losses, unless specifically noted otherwise.

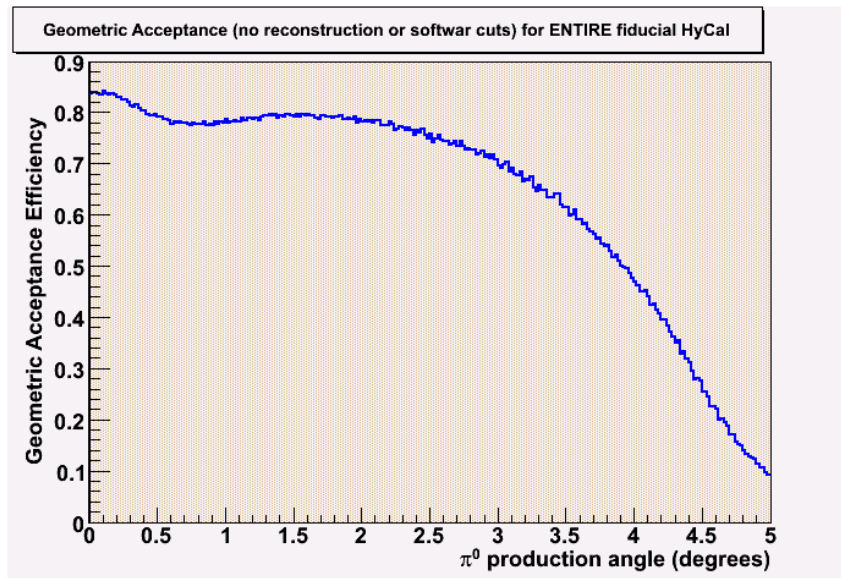


Figure 6.10: Geometric acceptance over entire HyCal

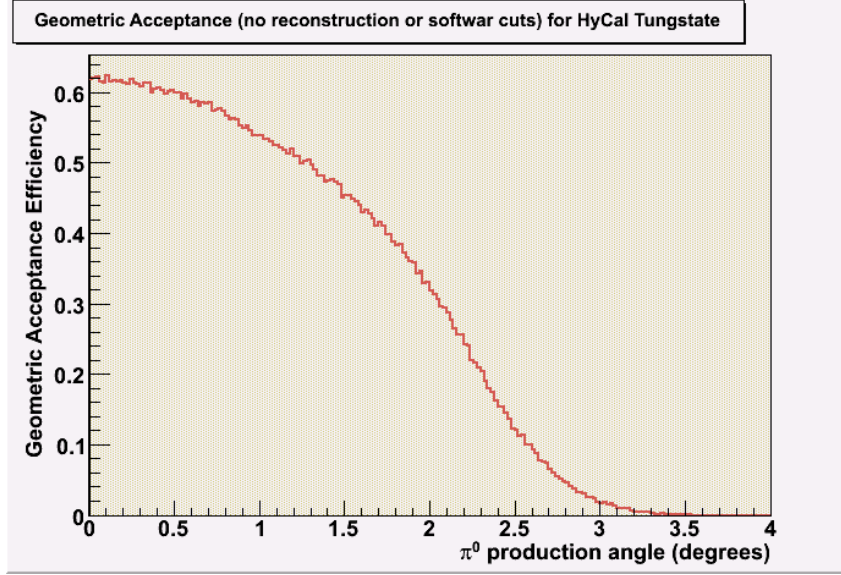


Figure 6.11: Geometric acceptance over HyCal tungstate

The next evolution of efficiency calculations includes using the reconstruction cuts (Equation 7.2).

$$\underline{\text{Efficiency (thrown angle)} =}$$

$$\underline{\# \text{HyCal events reconstructed at thrown prod. angle}} / (\# \text{thrown at production angle}).$$

No information regarding the reconstructed production angle at HyCal is considered.

This efficiency is what we call the (geometric×reconstruction) efficiency (Figures 6.12 and 6.13). The reconstruction efficiency has the appropriate cuts denoted in Chapter 5.1 applied for calculating this efficiency. Additionally, target absorption effects are already built into the above efficiencies.

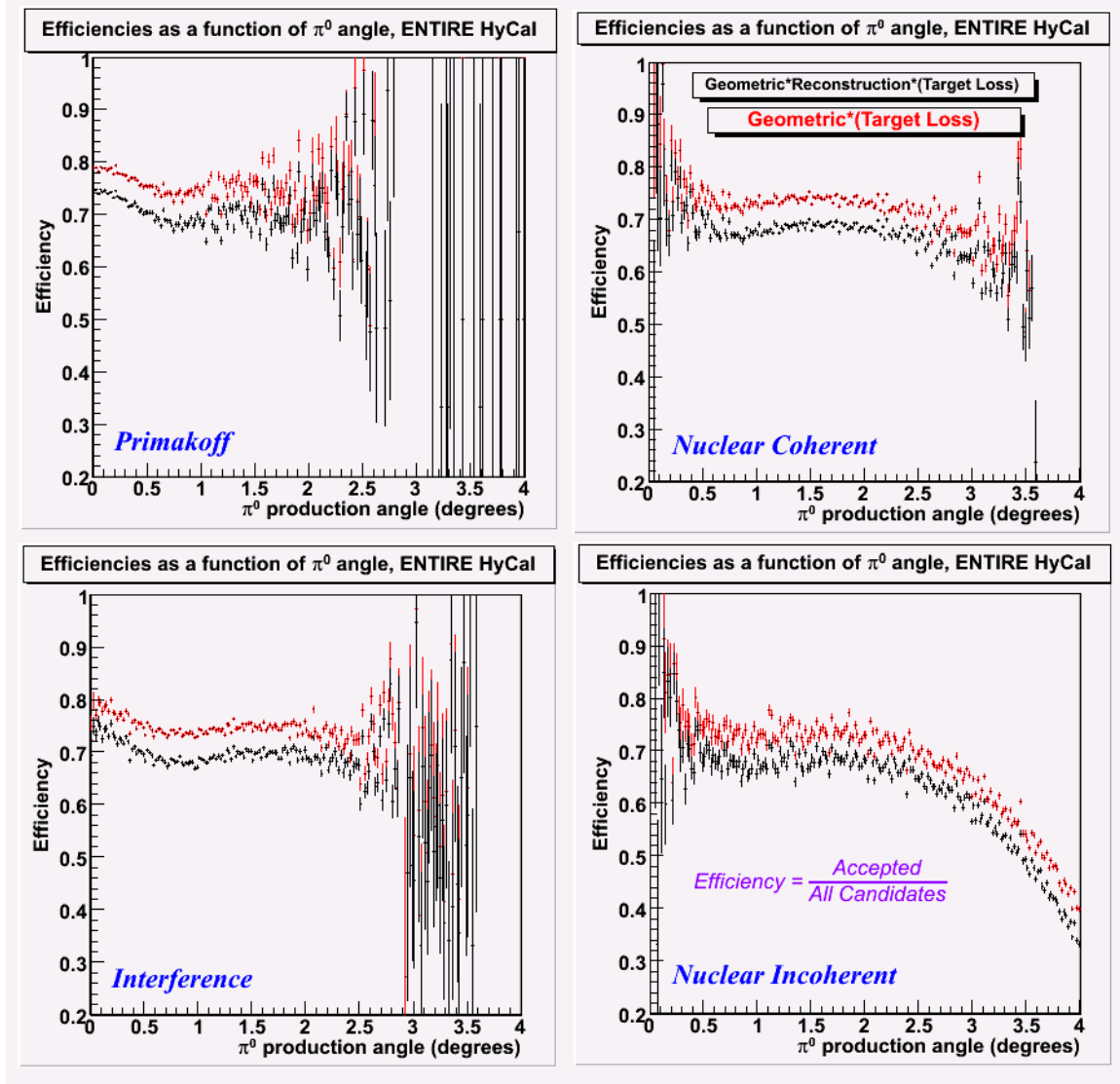


Figure 6.12: Geometric and geometric×reconstruction efficiencies for all photo-nuclear processes, entire HyCal acceptance

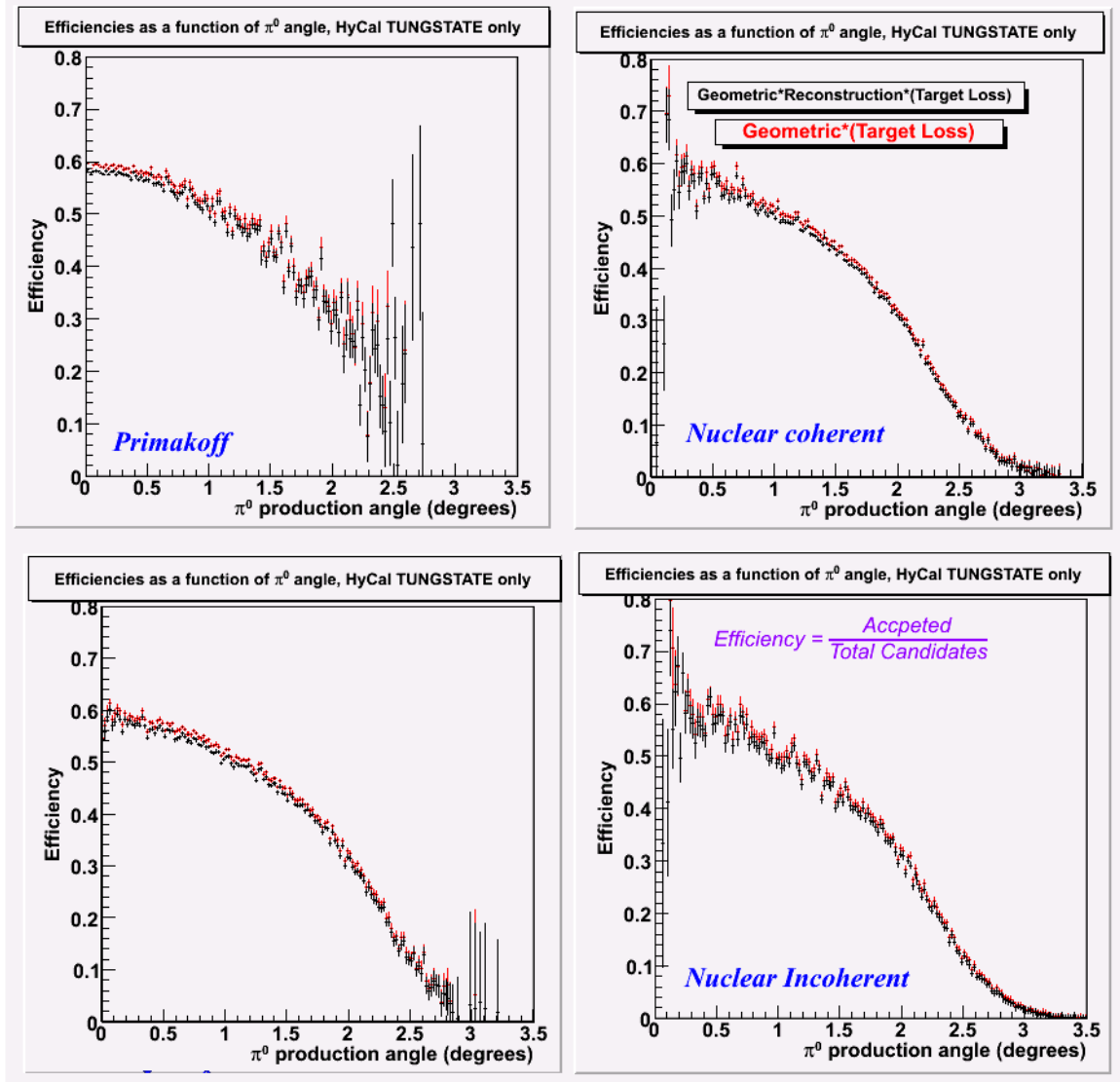


Figure 6.13: Geometric and geometric×reconstruction efficiencies for all photo-nuclear processes, tungstate only acceptance

For completeness it is required to look at the reconstruction efficiency as a function of the thrown angle (Figures 6.14, .615, 6.16, and 6.17).

$$\text{Efficiency (Thrown angle)} = \# \text{ of events reconstructed} / (\# \text{ of HyCal events}) \quad (7.3)$$

This is exactly (geometric efficiency)/(geometric×reconstruction efficiency). Target absorption effects are built into this efficiency as well.

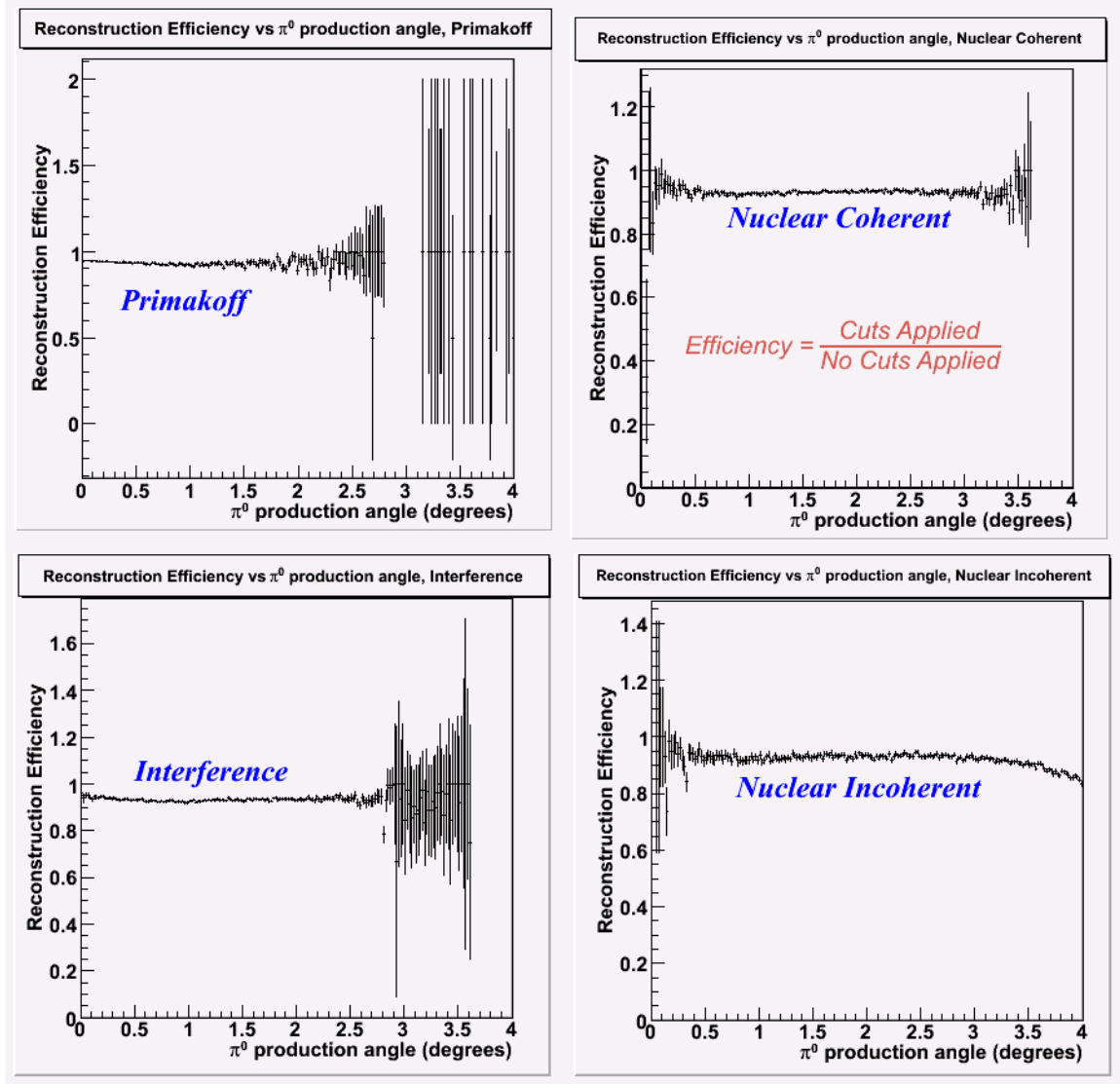


Figure 6.14: Reconstruction efficiencies for all photon-nuclear processes, entire HyCal acceptance

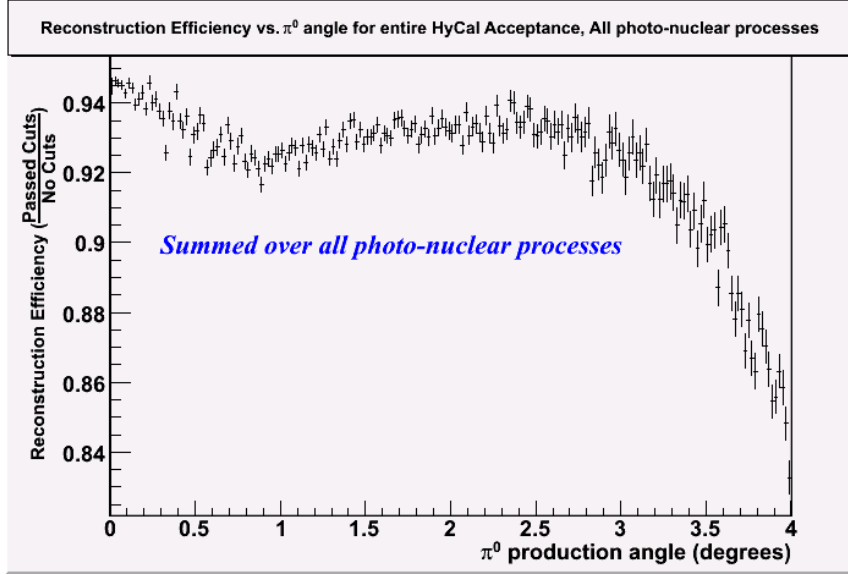


Figure 6.15: Reconstruction efficiency, summed over all photon-nuclear processes, entire HyCal acceptance

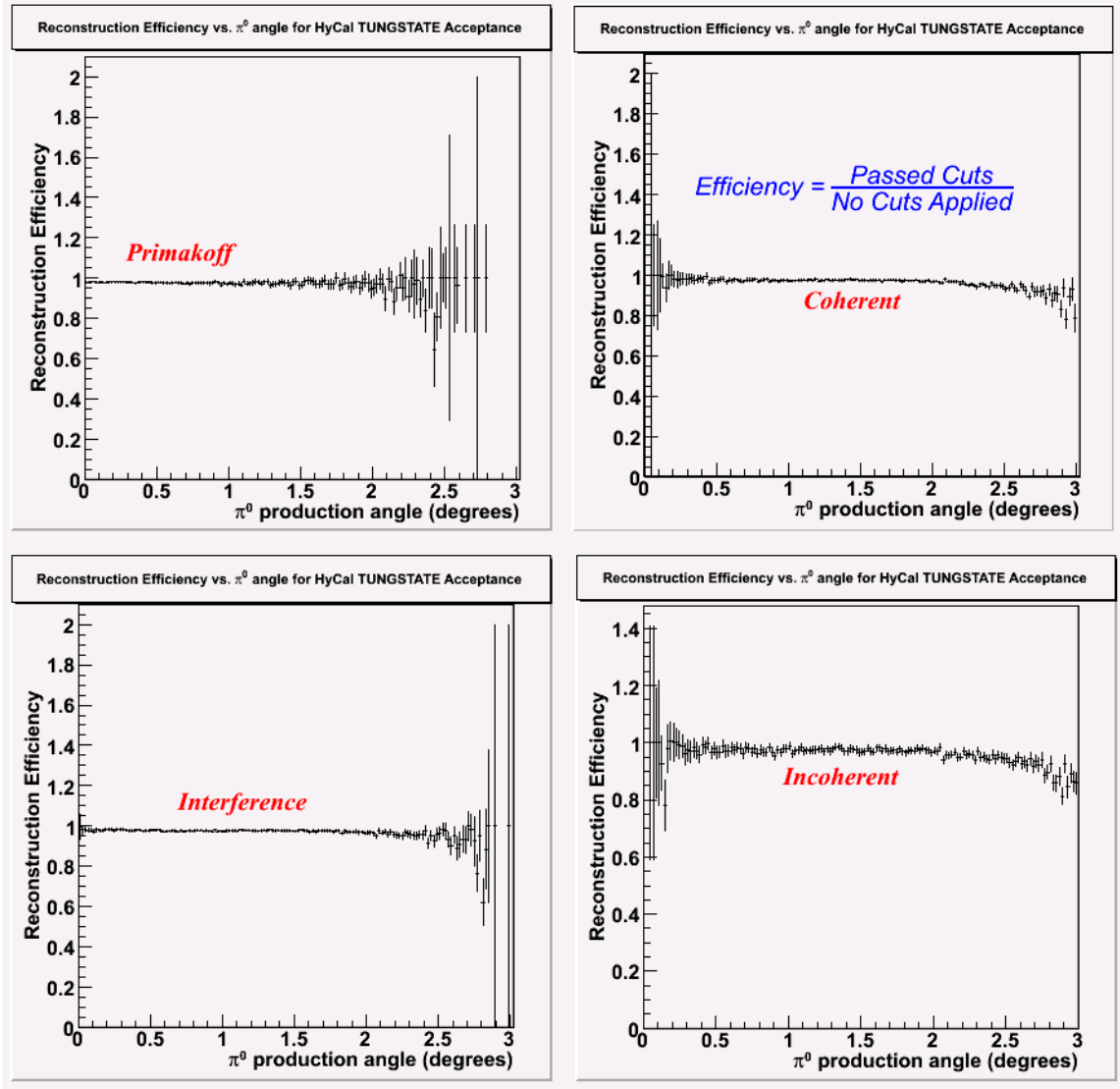


Figure 6.16: Reconstruction efficiencies for all photon-nuclear processes, tungstate only acceptance

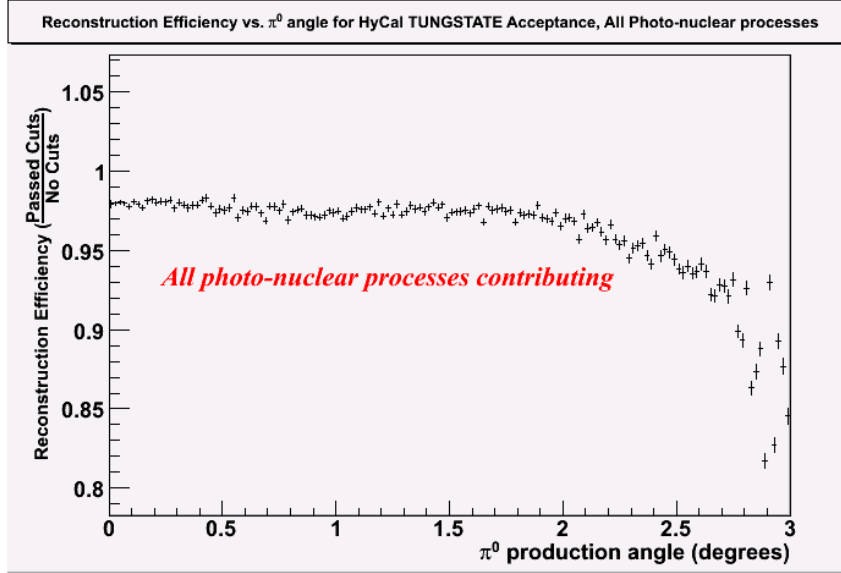


Figure 6.17: Reconstruction efficiency, summed over all photon-nuclear processes, tungstate only acceptance

6.4 Small π^0 production angle Resolution Effects

During testing of the PrimEx Monte Carlo, a small angle resolution effect was noted when the normalized Primakoff yield was plotted as a function of thrown and reconstruction π^0 production angle (Figure 6.18). At small angles, there is a depopulation of the small angle bins and over population of higher angle bins. The source of this effect is due to the reconstruction of the production angle. Figure 6.19 shows the “Thrown angle vs. Reconstructed” angle. A vertical projection along various thrown π^0 production angles reveals a failure of the angle reconstruction algorithm (Figure 6.20). Hundreds of events are poorly reconstructed to higher angles. This effect is ONLY a small angle effect. The loss of phase space to the gaussian distributed error in the reconstructed angle at very small angles is the source of this effect. At sufficiently large production angles (0.25° and larger) there is enough phase space for a mostly gaussian

distributed error (Figure 6.20). Thus, as small angle bins are depopulated by this effect, there is an over population at higher angles.

It should be noted that this effect is absent for the nuclear coherent and incoherent processes. This is probably due to low statistics at small angles. The majority of small angle events do reconstruct within the 0.02° bin width, and the expectation to see gaussian distributed error at low statistics is not unreasonable.

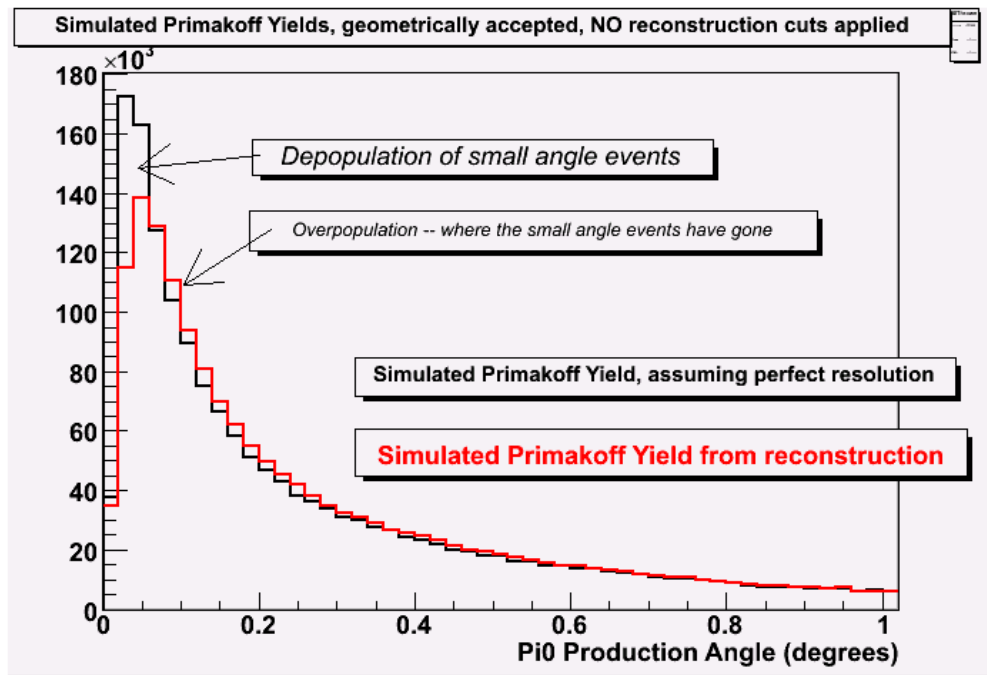


Figure 6.18: Shifting of thrown small angle events to larger reconstructed angles

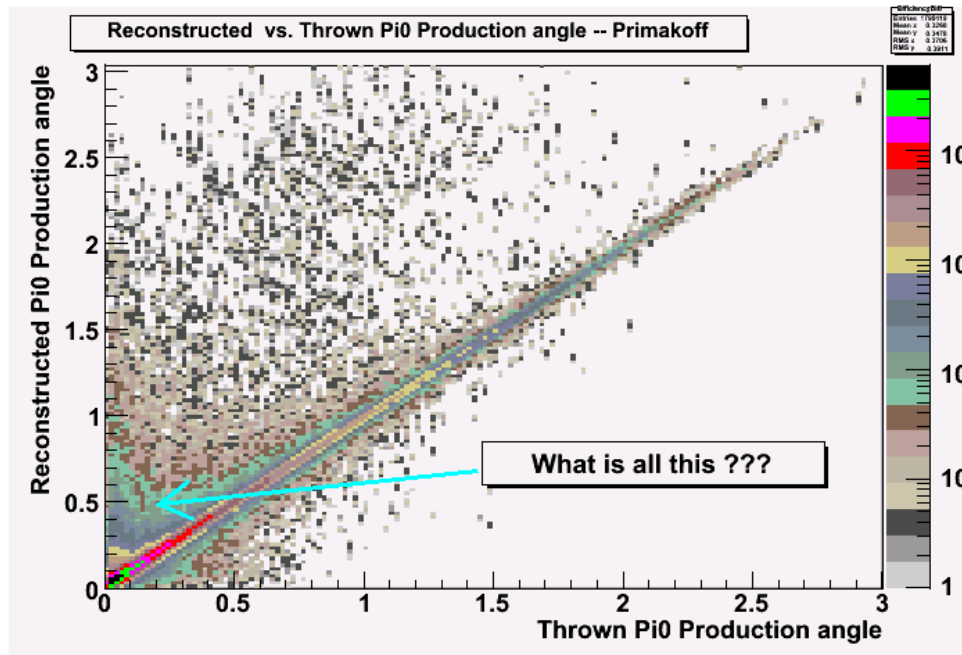


Figure 6.19: Reconstructed vs. Thrown Primakoff Production Angle. Note the large “background” at small production angle

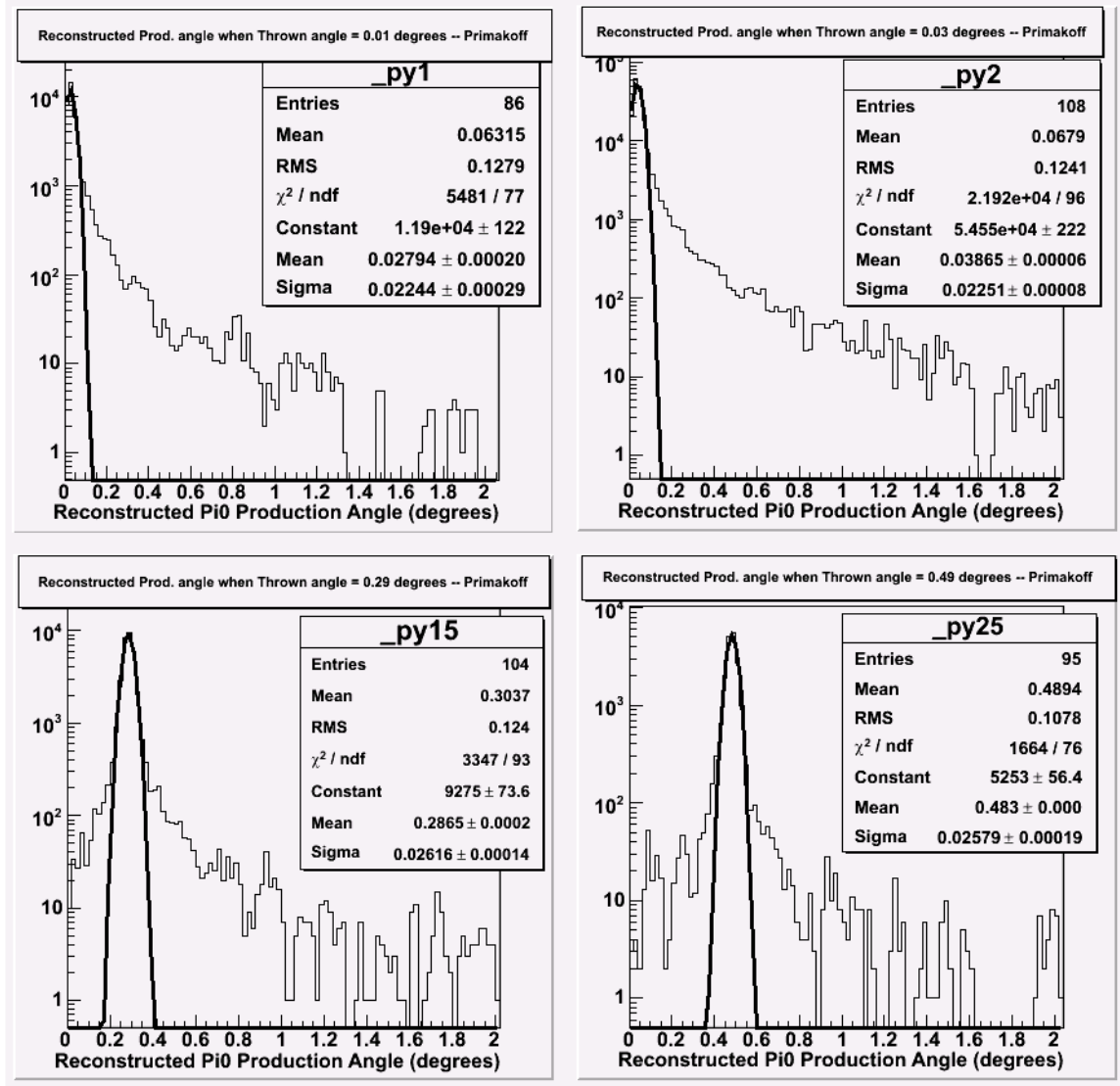


Figure 6.20: Thrown small angle events are getting pushed out to higher reconstructed angles due to limited phase space. Note that sigma of gaussian shows consistent 0.025° angular resolution and mean of gaussian is very close to thrown angle. (HyCal tungstate acceptance).

6.5 Validity of the simulation

While the previous sections describe the effort put forth to develop the simulation into a useful tool, nothing has been shown that demonstrates how well the simulation can reproduce physics. We answer this need with two studies.

6.5.1 Recreation of the experimental angular spectrum

Since this simulation and the geometry defined therein are essentially untested and unverified, the suggestion to use 4-vectors from experimental data was implemented. The specifics of this study are very simple. All of the “Most Likely” candidate events (~ 1.6 million for total HyCal acceptance and 450K for tungstate only) from ^{12}C data were loaded into the simulation and thrown at the simulation HyCal. All software cuts and/or restrictions were turned off since this all these events have passed these cuts once already. A new angular spectrum was reconstructed and compared to the input spectrum. A comparison of these two spectrums (Figures 6.21 and 6.22) shows a very high fidelity ($\sim 99.2\%$), even when the angular spectrum has been passed twice through PrimEx reconstruction software and is subject to a doubling of resolution effects. All fidelity loss was tracked down to events sneaking through non-light producing gaps in the detectors material , especially at shallow incident/polar angle to HyCal (Figure 6.23). A final investigation (Figure 24) using the physical four vectors was to rotate the horizontal and vertical momenta of the reconstructed photons by 90° and propagate these new four vectors in the simulation. This test could potentially reveal any acceptance systematic shifts or unknown detector correlations in the simulation or physical HyCal. The data in Figure 22 and Figure 6.24 do not suggest any such issues are present in PrimEx data.

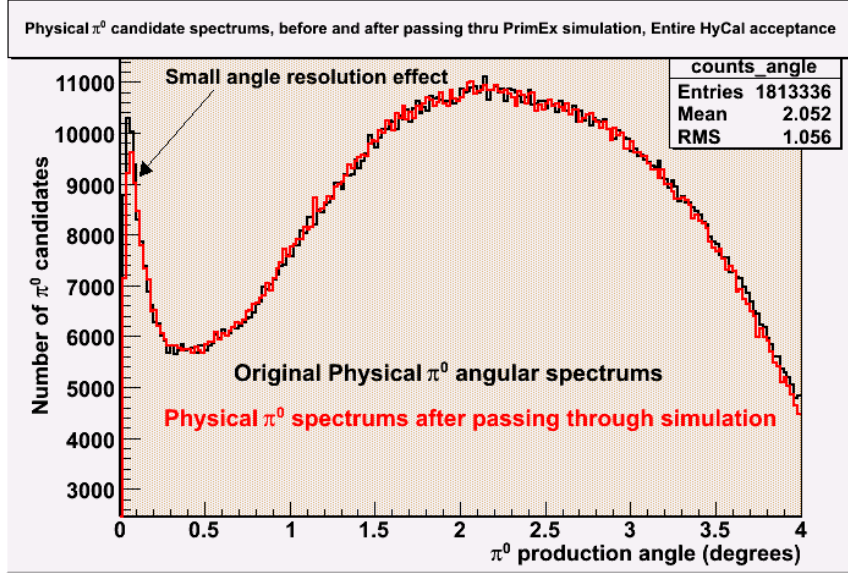


Figure 6.21: Original physical π^0 candidate angular spectrum before and after running through simulation, entire HyCal acceptance

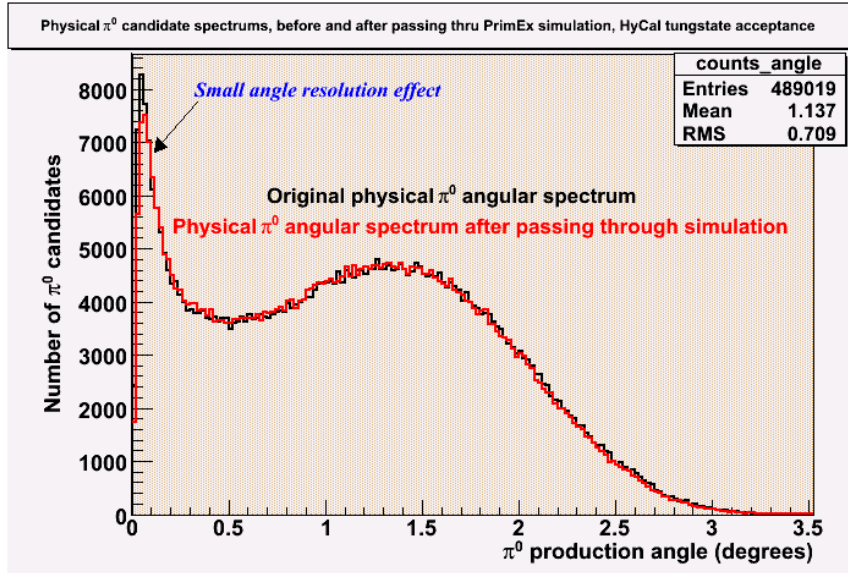


Figure 6.22: Original physical π^0 candidate angular spectrum before and after running through simulation, HyCal tungstate acceptance

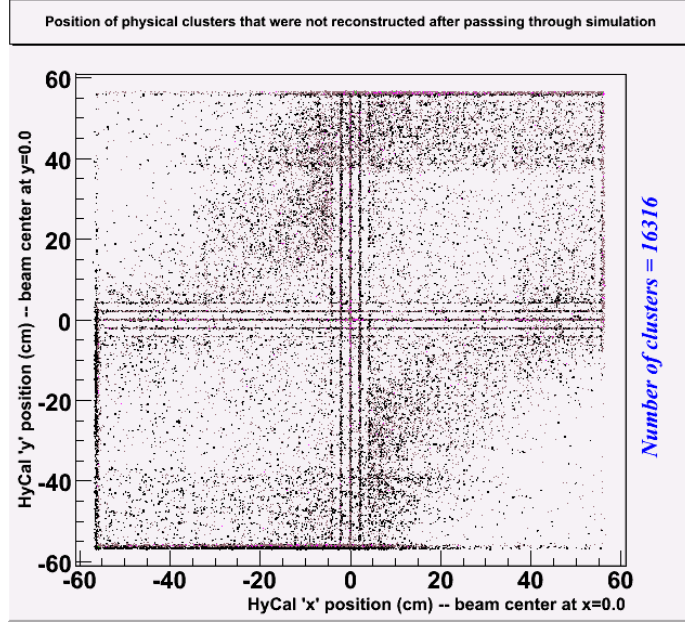


Figure 6.23: Location of physics events that failed to reconstruct after passing through simulation, HyCal tungstate acceptance. $16316/1813336 = 0.002$

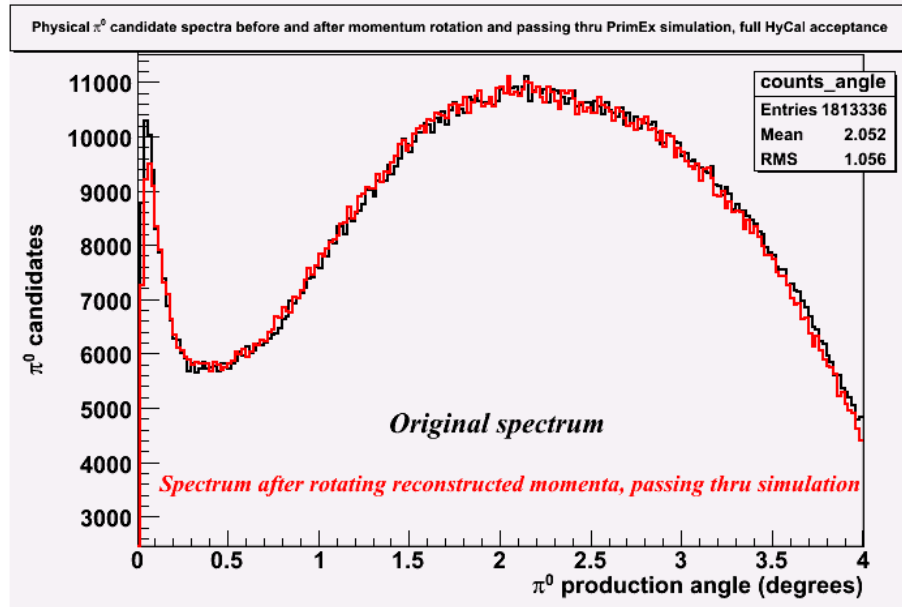


Figure 6.24: Original physical π^0 candidate angular spectrum, before simulation and after photon vertical and horizontal momenta rotation and through simulation, HyCal tungstate acceptance

6.5.2 Effects of a dead detector or detectors

Although no dead tungstate detectors are present in the data, a few detectors with anomalous calibration constants, gains, or pedestals were noticed. (At most, 4 lead glass detectors were maximally ineffective during the same data set.) These detectors could potentially alter the reconstructed π^0 angular spectrum. To simulate a worst case scenario, it is feasible to “turn off” a detector or detectors in the simulation and compare the π^0 angular spectrum to the π^0 angular spectrum with all detectors working.

This was done using 36 million thrown (~21.8 million accepted) simulated events. When using the experimental 4-vectors, angular spectrums were compared only after they had been passed thru PrimEx software twice. To get a better understanding of the effect of a dead detector or detectors on resolution and acceptance, simulation was used. Using simulation eliminated the problem of low statistics and the doubling of software resolution effects. The following scenarios were examined.

- 1.) One tungstate detector turned off.
- 2.) Two randomly located tungstate detectors turned off.
- 3.) Four randomly located tungstate detectors turned off.
- 4.) Ten randomly located tungstate detectors turned off.

Figure 6.25 summarizes the previous four scenarios.

- 5.) One *glass* detector turned off.
- 6.) Two randomly located *glass* detectors turned off.
- 7.) Four randomly located *glass* detectors turned off.

8.) Ten randomly located *glass* detectors turned off.

Figure 6.26 summarizes the previous four scenarios.

For completeness, the same studies were repeated with just the HyCal tungstate acceptance and only tungstate detectors turned off with ~13.2 million accepted (Figure 6.27). See Appendix B for a complete listing and identification of the detectors turned off for this study.

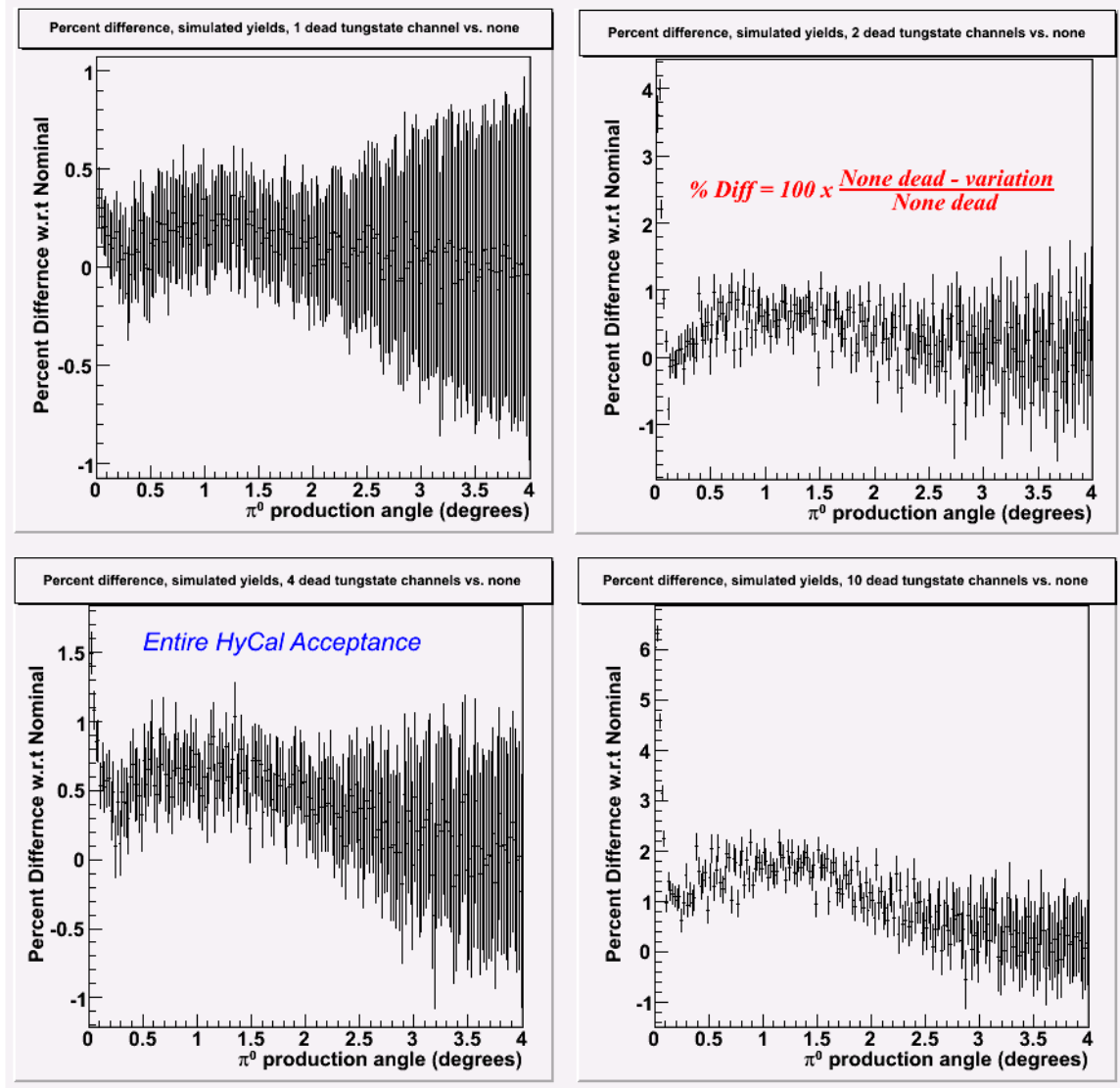


Figure 6.25: How acceptance with dead *tungstate* detectors changes with respect to full acceptance, total HyCal acceptance

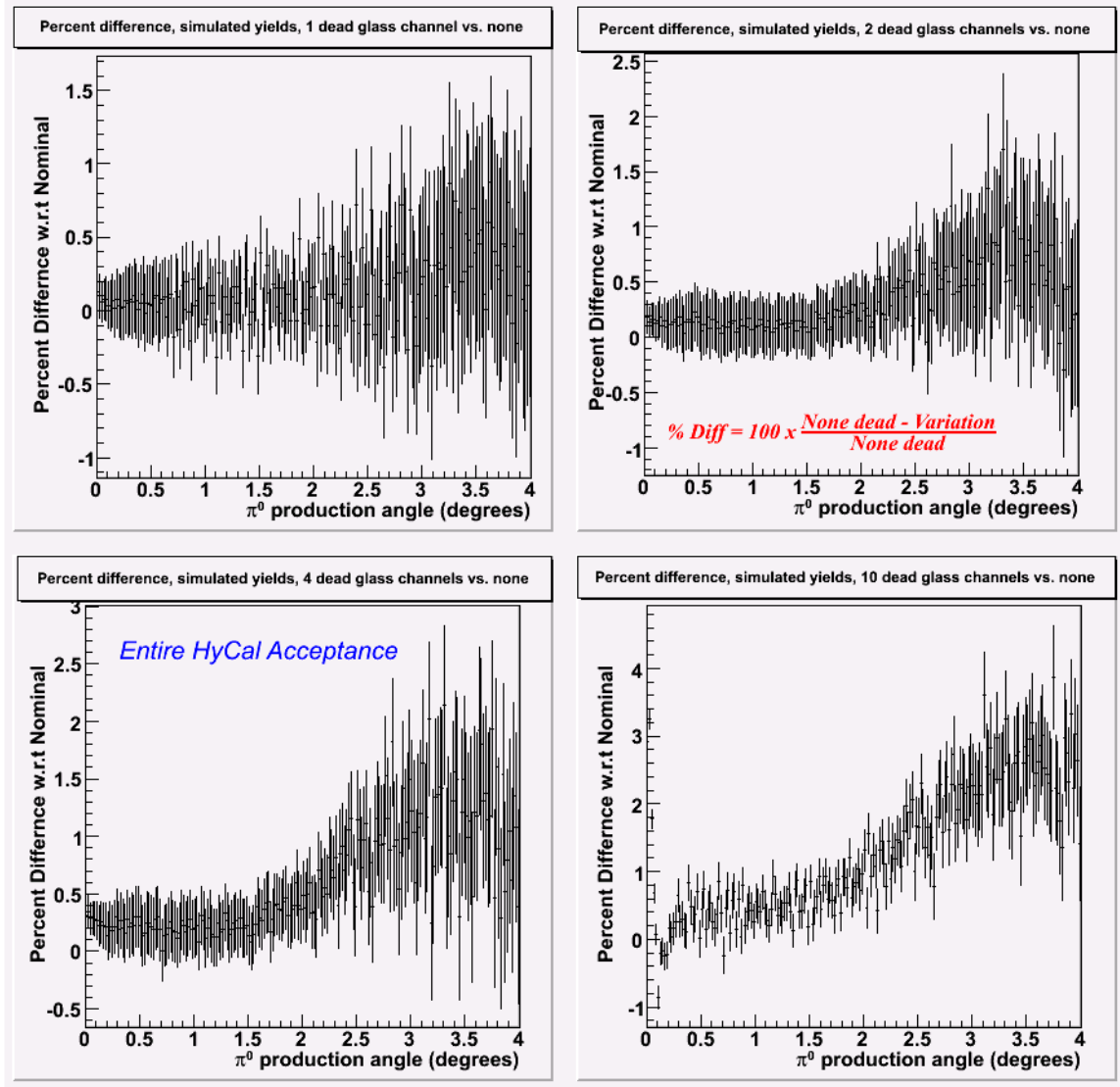


Figure 6.26: How acceptance with dead *glass* detectors changes with respect to full acceptance, total HyCal acceptance

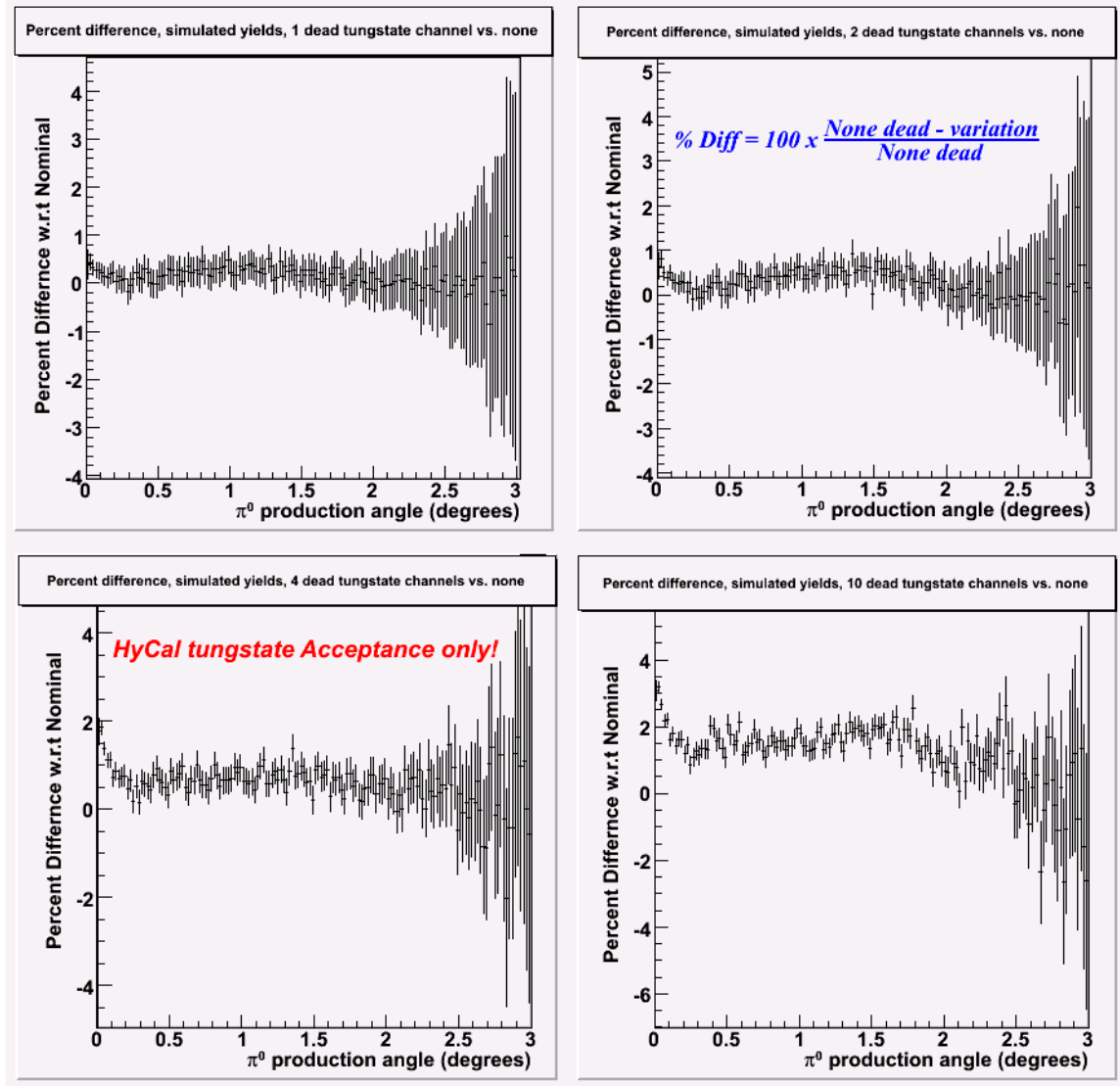


Figure 6.27: How acceptance with dead *tungstate* detectors changes with respect to full acceptance, HyCal tungstate acceptance only

6.5.3 Trigger efficiency study

The worst case scenario, a dead anode not contributing to the total sum trigger and the cluster energy, has been thoroughly explored. However, it is possible to only turn off the contribution of a single detector to the total sum trigger. This represents a dead dynode in the PrimEx trigger, and systematic effects due to trigger inefficiencies can be studied. The following scenarios were examined (Figure 6.28) for tungstate acceptance only.

- 1.) One tungstate trigger dynode turned off.
- 2.) Two randomly located tungstate dynodes turned off.

- 3.) Four randomly located tungstate dynodes turned off.
- 4.) Ten randomly located tungstate dynodes turned off.

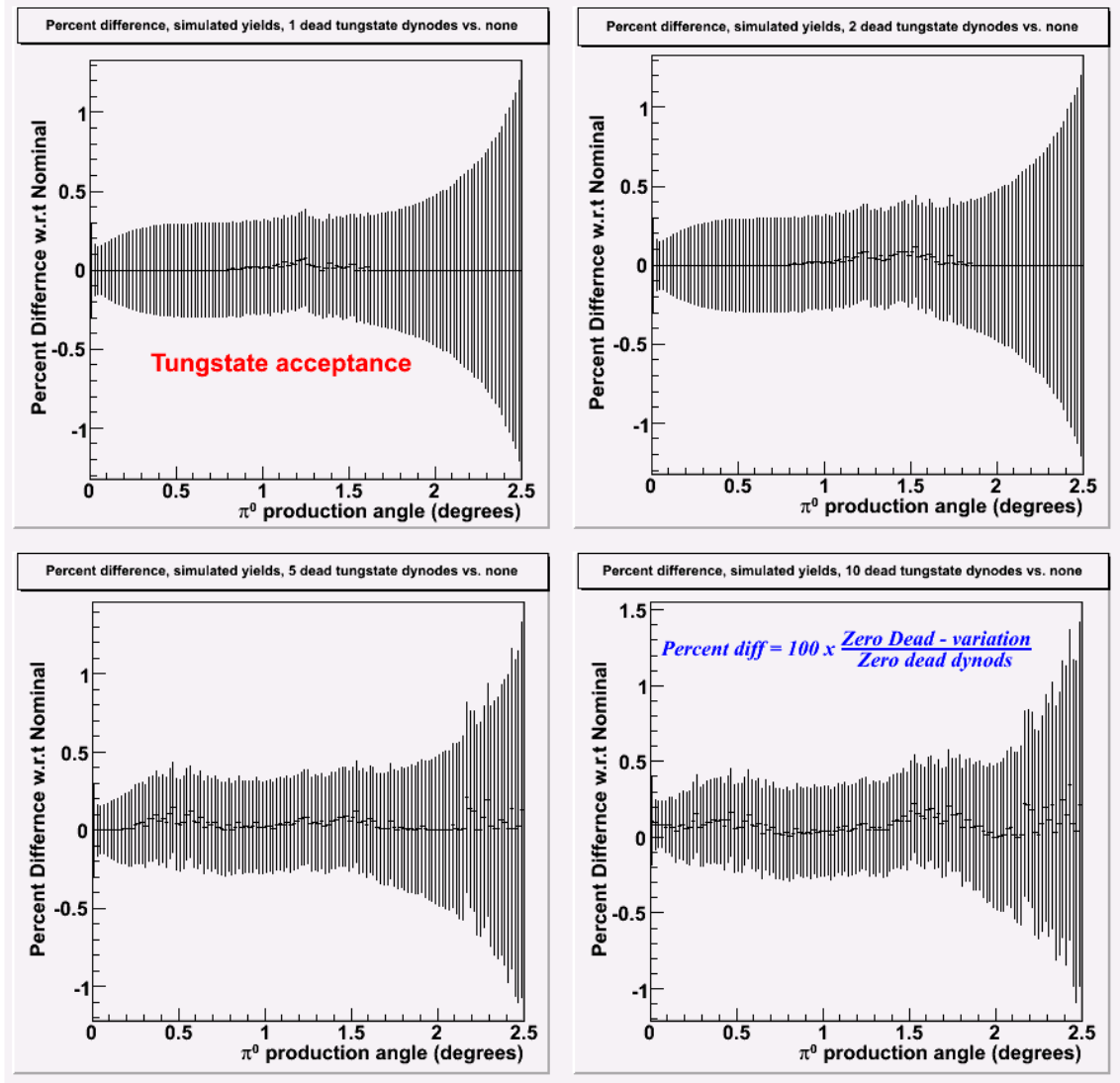


Figure 6.28: How acceptance with dead *tungstate dynodes* changes with respect to full acceptance, HyCal tungstate acceptance only

In summary regarding the simulation and its validity for this experiment, the studies and work detailed in this Chapter should be sufficient evidence of the ample

robustness of the standard PrimEx simulation software and its applicability to the physics.

6.6 Comparison of Cluster Position Finding Methods

With a robust simulation, a comparison of simulated yields between cluster position finding methods is useful (Figures 6.29 and 6.30). While very few systematic effects can be noted or gleaned from such a comparison, it is a test of the relative similarity between the cluster finding algorithms.

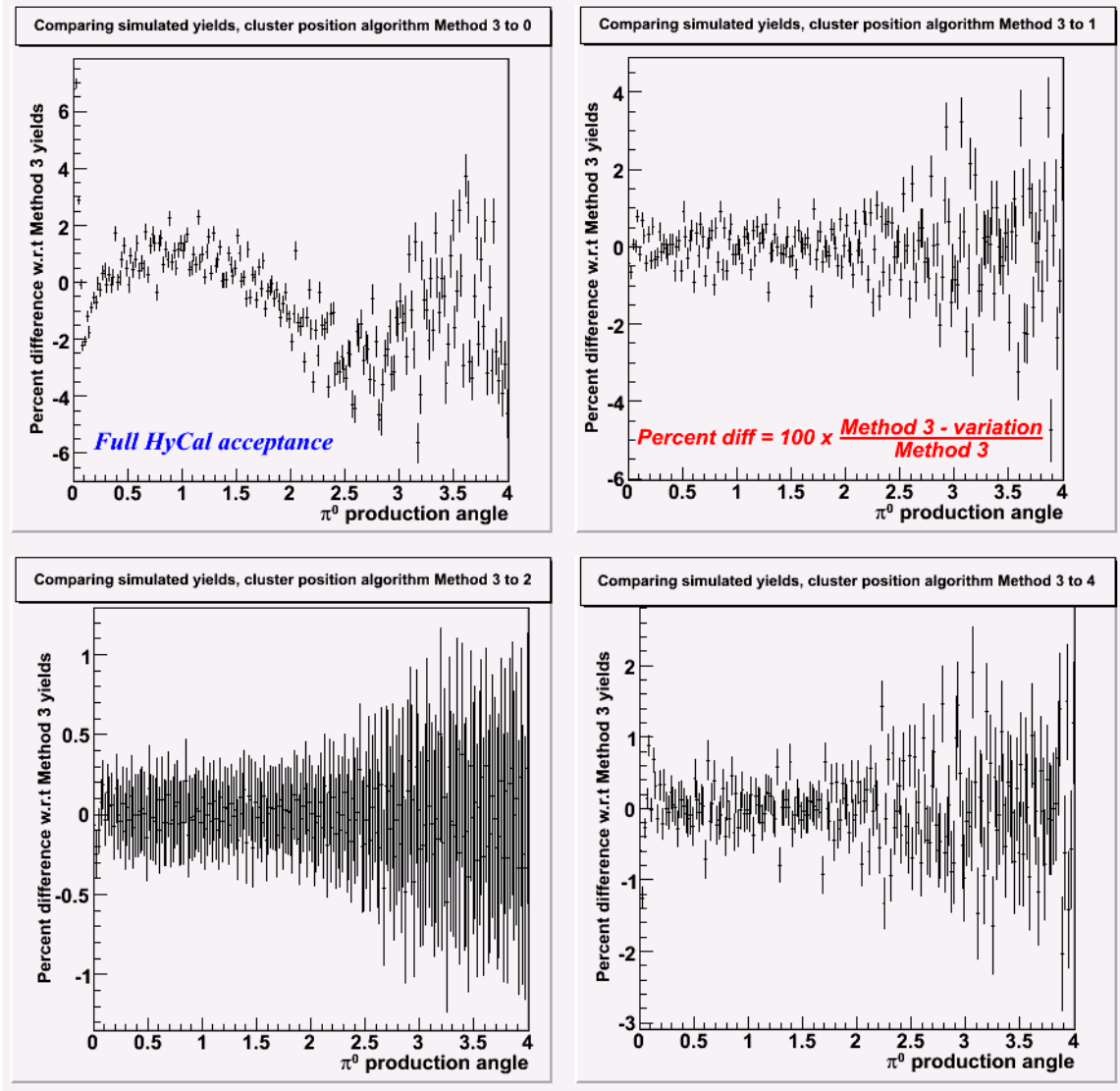


Figure 6.29: Comparing cluster position finding algorithms. Full HyCal acceptance, 36 million events thrown, ~21.8 million accepted

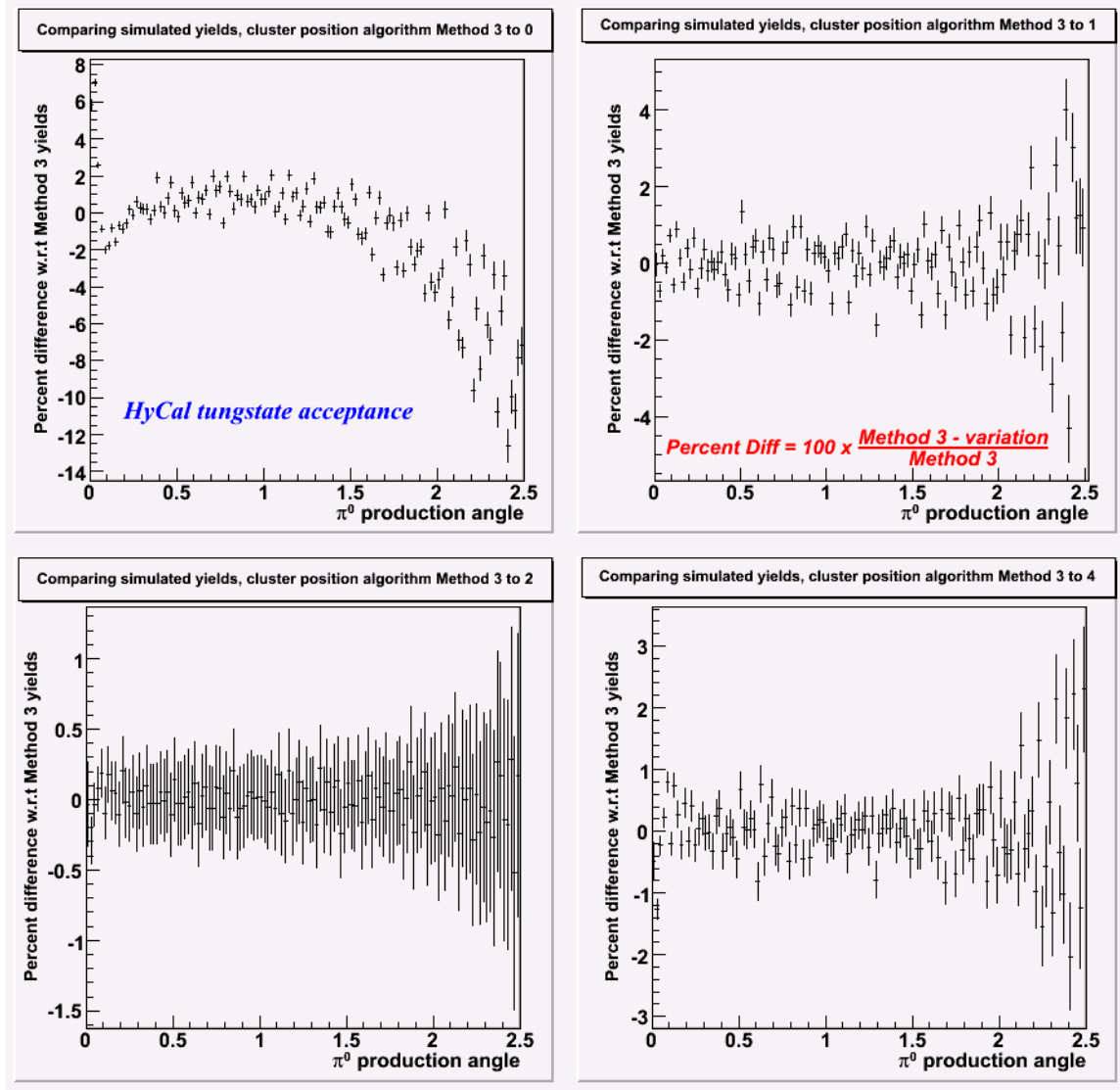


Figure 6.30: Comparing cluster position finding algorithms. HyCal tungstate acceptance, 36 million events thrown, ~13.2 million accepted

6.7 PrimEx Target Thickness effective p_t and Photon Flux Calculation

An extensive measurement of the pyrolytic ^{12}C target was discussed in Chapter 4. Incident photon flux loss is also modeled via an “effective” target thickness. This effective target $p_t = 1.046 \times 10^{23} \text{ atoms/cm}^2 \pm 0.04\%$ models incident beam absorption (i.e. photon flux loss) and the effects of impurities. Interested parties should reference

the following email which contains details on the effective pt calculation:

http://www.jlab.org/ccc/mail_archives/EXPERIMENTS/primex/msg01751.html.

The photon flux (Figure 6.31 and Appendix C) for this analysis was calculated using standard PrimEx software located in CVS (*src/libraries/pflux/*). At the time of this dissertation, an error in the photon flux code was discovered that required a 2.4% increase in the photon flux due to a misunderstanding regarding our DAQ timing oscillator. Figure 6.31 and Appendix C to not have this global 2.4% increase applied, but the radiative width and cross sections quoted in this work do have this correction built in. Please refer to Chapter 4 for details on the extraction of photon flux as a function of E-channels or T-channels.

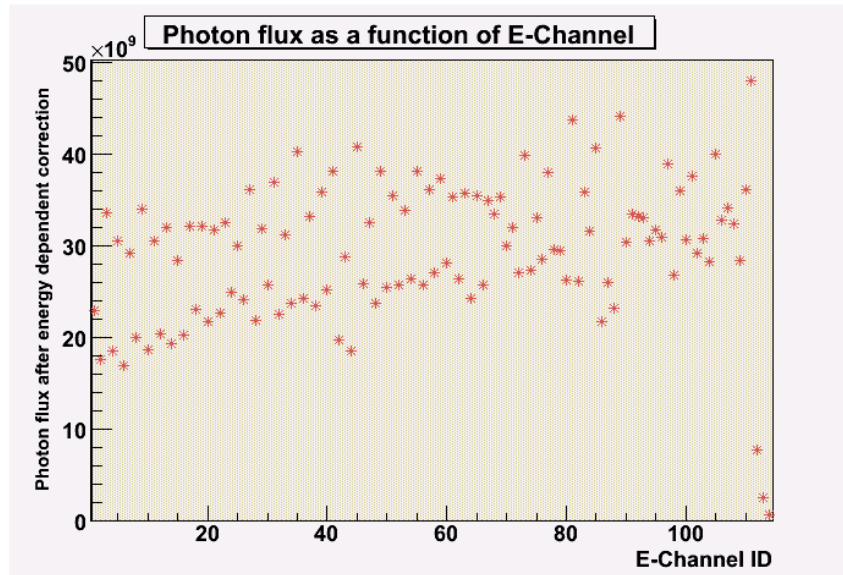


Figure 6.28: Photon Flux for ^{12}C data, tagger rad. B. Total Flux = 3.34898×10^{12} photons

CHAPTER 7

EXTRACTION OF THE π^0 RADIATIVE WIDTH AND FUTURE WORK

7.1 Obtain normalized yields

1.) Using Elastic yields from HyCal tungstate acceptance, we divide the yield in each bin by $\Delta\theta$ (radians), the number of tagged photons incident on the target, and the effective number of target atoms/cm². This gives the uncorrected pion differential cross section (Figure 7.1 and Appendix D),

$$\frac{d\sigma^{\text{uncor}}(\theta)}{d\theta} \quad (7.1)$$

7.2 Generation of simulated normalized yields and fit to physical data.

Let $F(E_\gamma, \theta_\pi, \theta_\pi')$ equal the resolution function for the detector, $\Phi(E_\gamma)$ is the photon flux probability distribution with unit normalization, and $\varepsilon(E_\pi, \theta_\pi)$ the pion acceptance. We would need to do the following integral for direct comparison with data,

$$\frac{d\sigma^{\text{process}}(\theta)}{d\theta} = \iint \frac{d\sigma^{\text{process}}(E_\gamma, \theta')}{d\theta'} F(E_\gamma, \theta, \theta') \Phi(E_\gamma) \varepsilon(E_\pi, \theta') d\theta' dE_\gamma \quad (7.2)$$

where “process” is Primakoff, coherent, interference, or incoherent. Since we don’t have functional forms for $F(E_\gamma, \theta, \theta')$ or $\varepsilon(E_\pi, \theta)$, we’ll use a Monte Carlo to do the integration.

- 2.) Generate random events weighted by $d\sigma^{\text{process}}(E_\gamma, \theta)/d\theta \cdot \Phi(E_\gamma)$. In order to get the right magnitude for the interference cross section, the **number of thrown**

events must be the same for the Primakoff, coherent and interference simulations.

- 3.) Put the events into the monte-carlo and see if they reconstruct as good π^0 's.
- 4.) Run many events and find the ratio of accepted events to thrown events as a function of the *thrown* pion angle, $\epsilon^{\text{process}}(\theta) = N^{\text{accepted}}(\theta)/N^{\text{thrown}}(\theta)$. Also find the total acceptance $\epsilon^{\text{process}} = N^{\text{accepted}}/N^{\text{thrown}}$. We define Monte Carlo generated angular distributions as $D^{\text{process}}(\theta)$.
- 5.) Fit the uncorrected pion differential cross section (defined in Equation. 7.1) with distributions from Primakoff, nuclear coherent, interference, and incoherent,

$$A_1 D^{\text{Prim}}(\theta) + A_2 D^{\text{Coh}}(\theta) + 2\sqrt{A_1 A_2} \cos \phi D^{\text{Inter}}(\theta) + A_3 D^{\text{Incoh}}(\theta) \quad (7.3)$$

where the constants A_1, A_2, ϕ , are fit to the data (Figure 7.2).

- 6.) Find the radiative width.

$$A_1 \Delta\theta \sum_{\theta=0}^{\theta_{\max}} D^{\text{Prim}}(\theta) = K_1 \epsilon^{\text{Prim}} \int_0^{\theta_{\max}} d\theta \int_{\text{Lo-E}}^{\text{Hi-E}} dE_\gamma \frac{d\sigma^{\text{Prim}}(E_\gamma, \theta)}{d\theta} \Phi(E_\gamma) \quad (7.4)$$

The fitted radiative width (Figure 7.2) is given by

$$\Gamma_{\gamma\gamma} = K_1 \Gamma_{\gamma\gamma}^{\text{anomaly}} \quad (7.5)$$

$$\Gamma_{\gamma\gamma}^{\text{anomaly}} = 7.74 \text{ eV (from PDG)}$$

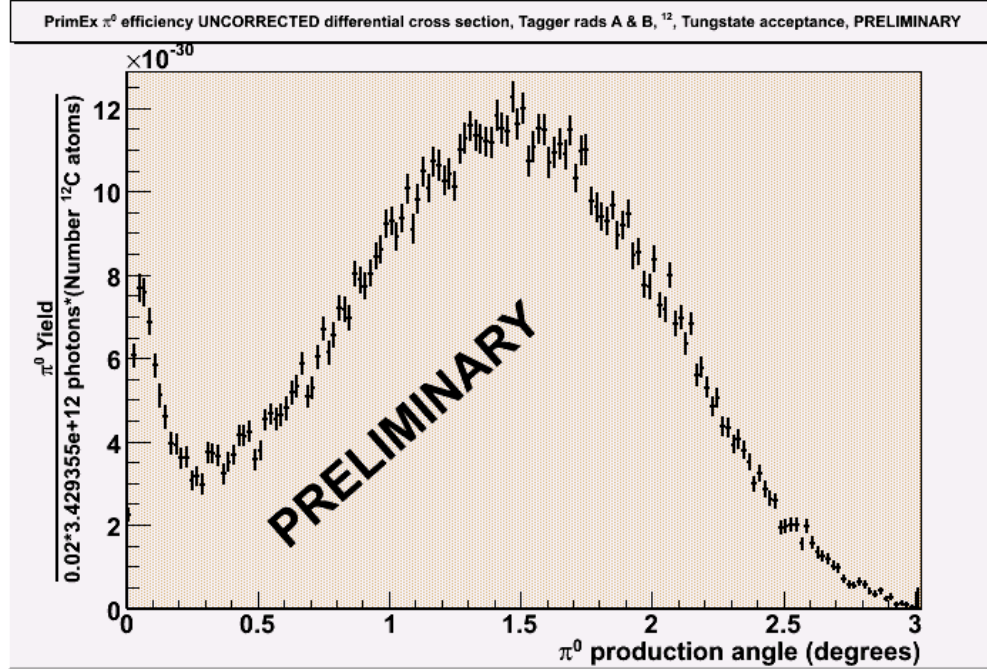


Figure 7.1: Acceptance Uncorrected Differential Cross Section, a.k.a. Normalized Yields. No timing accidental or charge particle veto corrections.

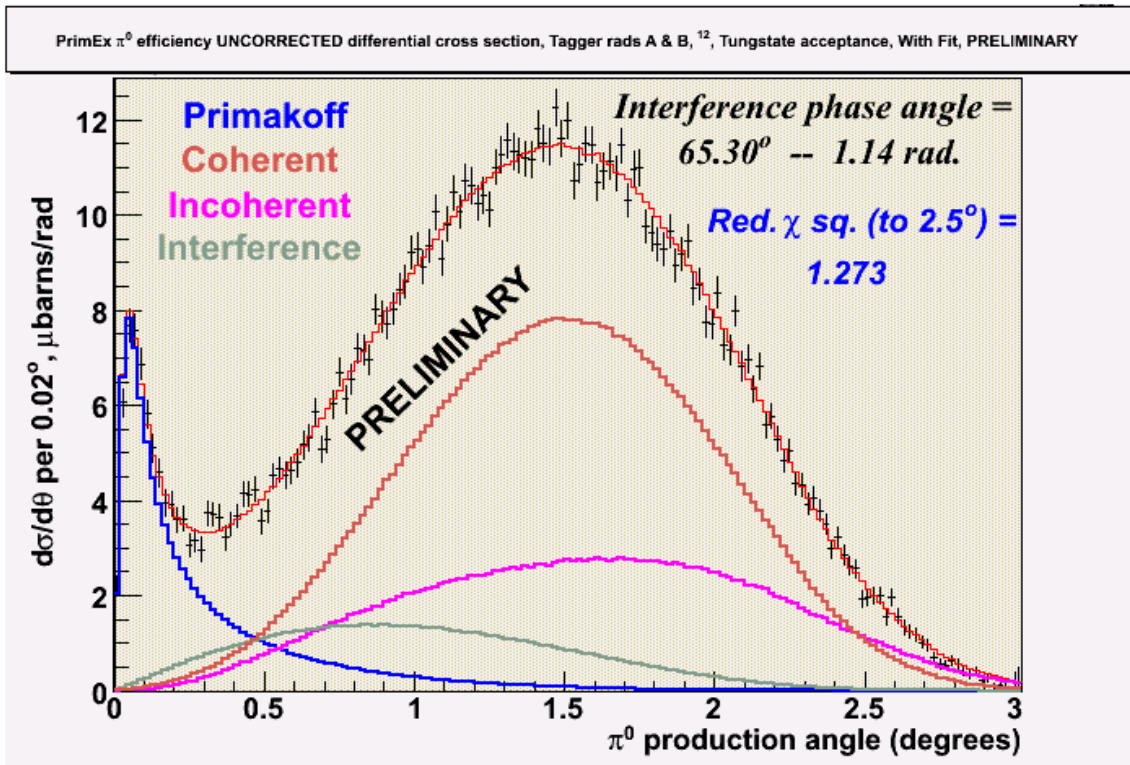


Figure 7.2: Normalized Yields with Fit to 2.5° , HyCal tungstate acceptance

7.3 Acceptance corrected cross sections.

- i. The acceptance as a function of angle and photo-pion production process

(Figure 6.13) is given by (Equation 7.6)

$$\varepsilon(\theta) = \frac{A_1 D^{\text{Prim}}(\theta) + A_2 D^{\text{Coh}}(\theta) + 2\sqrt{A_1 A_2} \cos \phi D^{\text{Inter}}(\theta) + A_3 D^{\text{Incoh}}(\theta)}{\left[\frac{A_1 D^{\text{Prim}}(\theta)}{\varepsilon^{\text{Prim}}(\theta)} \right] + \left[\frac{A_2 D^{\text{Coh}}(\theta)}{\varepsilon^{\text{Coh}}(\theta)} \right] + \left[\frac{2\sqrt{A_1 A_2} \cos \phi D^{\text{Inter}}(\theta)}{\varepsilon^{\text{Inter}}(\theta)} \right] + \left[\frac{A_3 D^{\text{Incoh}}(\theta)}{\varepsilon^{\text{Incoh}}(\theta)} \right]}$$

- ii. The acceptance corrected cross section (Figure 7.3 and Appendix D) is

$$\frac{d\sigma^{\text{cor}}(\theta)}{d\theta} \equiv \frac{1}{\varepsilon(\theta)} \frac{d\sigma^{\text{uncor}}(\theta)}{d\theta} \quad (7.7)$$

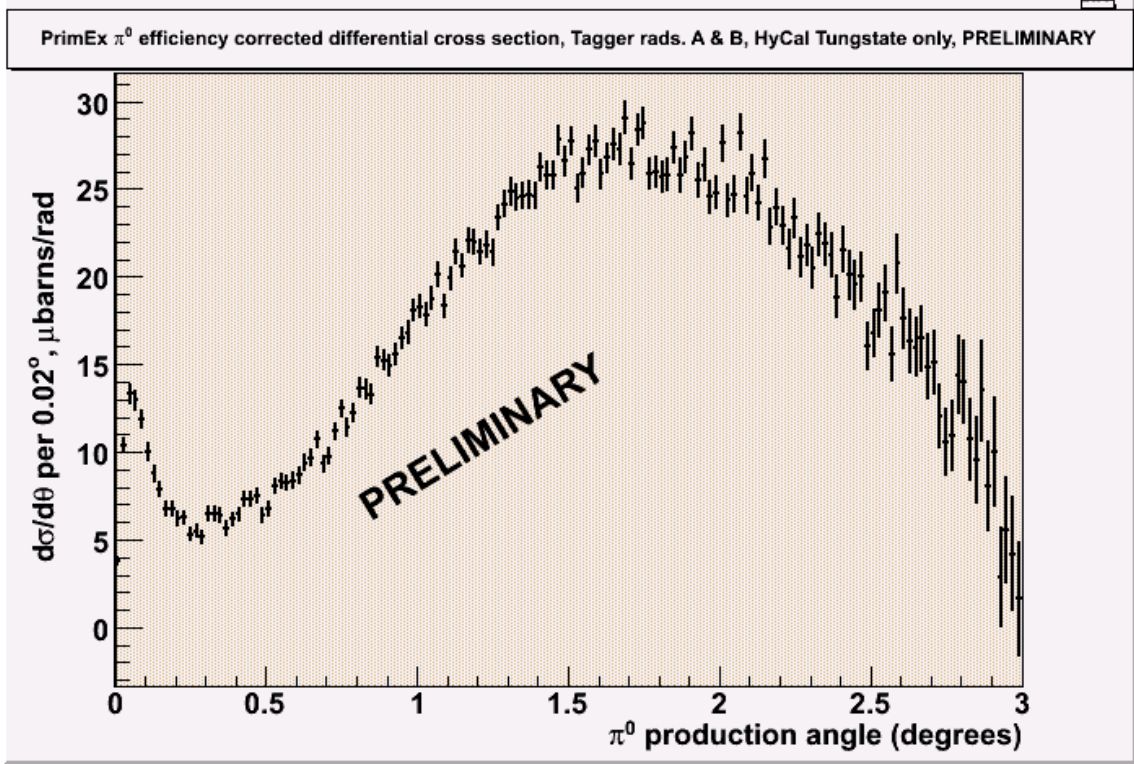


Figure 7.3: Acceptance corrected cross sections, HyCal tungstate acceptance

7.4 Error and Systematic Uncertainty Estimation

The nominal π^0 radiative width from this analysis is

$$\Gamma_{\gamma\gamma} = 8.411 \text{ eV} \pm 0.151 \text{ eV} \pm (\text{stat.}) 1.80\%, \quad (7.8)$$

where the statistical error is from the fit. We propose to quote an asymmetric systematic error. By varying a parameter, we tend to drive the width up or down in a predictable manner. Adding this error *symmetrically* in quadrature tends to overestimate any systematic shifts. Contributing positive systematic contributions will be denoted by “*++” and negative contributions will be denoted by a “*--” and neutral contributions use “***” to denote them.

7.4.1 Photon Flux

See section 4.2.6 and 4.2.7 1.10%. ***

7.4.2 Timing accidental suppression and charge particle veto misidnetification

See section 5.3.3.1 0.20%. ***

See section 5.6 0.05%. ***

7.4.3 Cluster Position Reconstruction

This has been determined by repeating the entire analysis using each of the four logarithmic cluster position finding methods. A maximum of 0.9% difference in the radiative width is seen between Method 3 and the other Methods.

Table 7.1: Cluster Position Systematic Error

<i>Method</i>	<i>Width</i>	<i>% Diff from Nom.</i>	
0	8.195 eV	-2.566	
1	8.365 eV	-0.428	
2	8.375 eV	-0.428	
3 (Nominal)	8.089eV	NA	
4	8.311 eV	-1.198%	*--

Method 0 will not be considered as an upper or lower bound on cluster position finding systematic effects because it is known to suffer from large systematic effects. We wish to compare similar, less systematic effect prone methods.

7.4.4 Target Thickness

Negligible. See 4.2.2. 0.04%. ***

7.4.5 Yield Extraction, Possible Fitting Range Systematics

As noted in 5.3.3.2, there was a clear plateau in the extracted radiative width as a function of the fitting endpoints, consistent with small statistical fluctuations. Therefore, there is no compelling reason to expect any appreciable systematic shifts from varying the fitting range.

7.4.6 Yield Extraction, Possible Integration Systematics

As noted in 5.3.3.3, there was a clear plateau in the extracted radiative width as a function of the integration range, consistent with small statistical fluctuations that grow as the fit error grows. Therefore, there is no compelling reason to expect any appreciable systematic shifts from varying the integration range.

7.4.7 Yield Extraction, Signal and Background Lineshape Degrees of Freedom

Compare radiative widths when using yields extracted from fits with larger number of degrees of freedom in the signal and background models.

Table 7.2: Background and Signal Model Systematic Error

<i>Lineshape</i>	<i>Width</i>	<i>% Diff from Nom.</i>	
Double Gaussians, third order polynomial	8.426 eV	0.467	*--
Triple Gaussians, second order polynomial	8.342 eV	0.171	*++

7.4.8 Total Error Budget

Table 7.3: Total Error Accounting

<i>Source</i>	<i>% Error</i>
Statistical (from fit)	+1.80 %, -1.80 %
Photon flux	+1.10 %, -1.10 %
Cluster Position Reconstruction	+0.00 %, -1.20 %
Timing accidental suppression correction	+0.20 %, -0.20 %
Signal and Background Lineshapes	+0.17 %, -0.43 %
Dalitz Decay	+0.03 %, -0.03 %
Target Thickness	+0.04 %, -0.04 %
Veto Counter Inefficiency	+0.05 %, -0.05 %
Total (without Statistical)	+ 1.13 %, -1.70 %
Total (with Statistical)	+ 2.13 %, -2.47 %

To calculate the total asymmetric error, all neutral and positive systematic errors were added in quadrature to evaluate that contribution. Total neutral and negative systematic effects were added in quadrature to determine the negative systematic error.

7.5 Preliminary radiative width

From this fit we determine that the interference angle $\phi = 1.14$ radians or 65.29° , $K1 = 1.08669$, and our preliminary radiative width is:

$$\Gamma_{\gamma\gamma} = 8.411 \text{ eV} \pm 1.80 \% \text{ (stat.)} + 1.13 \% \text{ (syst.)} - 1.70 \% \text{ (syst.)}, \quad (7.10)$$

$$\Gamma_{\gamma\gamma} = 8.411 \text{ eV} \pm 0.151 \text{ eV (stat.)} + 0.095 \text{ eV (syst.)} - 0.143 \text{ eV (syst.)}. \quad (7.11)$$

The corresponding lifetime is $(7.826 \pm 0.141 + 0.088 - 0.133) \times 10^{-17} \text{ s}$.

7.6 Future work

Four particulars, as follows.

7.6.1 “Conjoined” tungstate and lead glass analysis

While the lead glass detectors suffer from poor resolution and elastic yield extraction systematics, they do provide much better acceptance of the nuclear incoherent background. We proposed a “conjoined analysis” where events are selected only from the HyCal tungstate in the 0.00° to roughly $1.00^\circ \pi^0$ angular range (Figure 7.4). For larger angles, the entire HyCal acceptance is used. This approach should allow for a precision extraction of the π^0 radiative width with a better understanding of how the nuclear incoherent background affects this measurement.

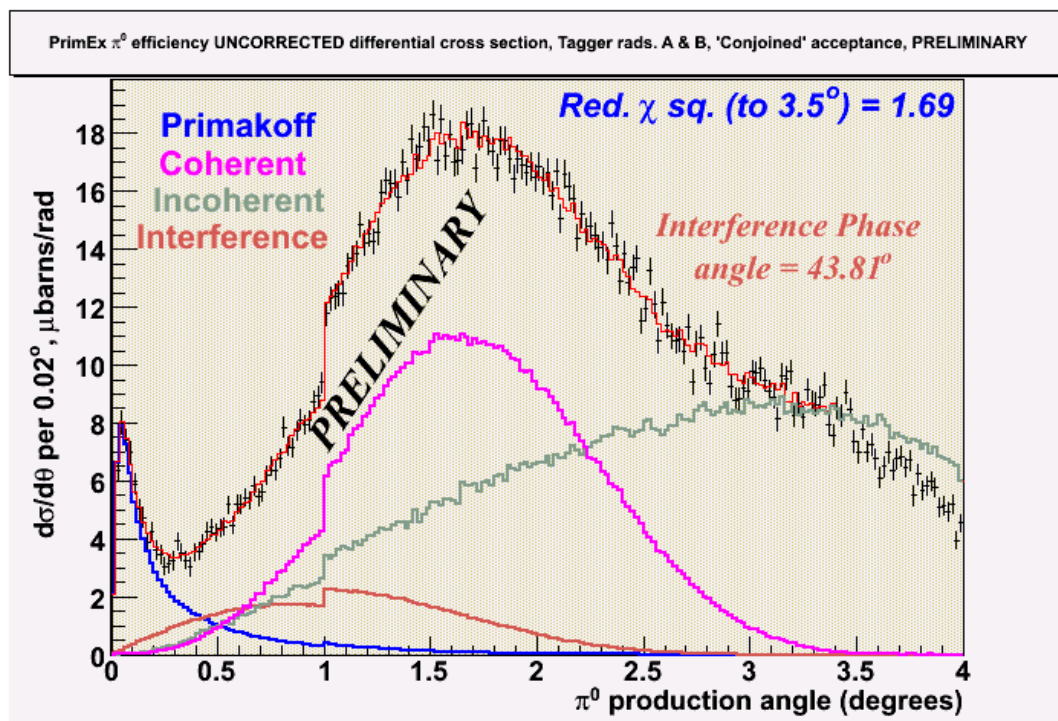


Figure 7.4: “Conjoined” yields

7.7.2 Additional nuclear incoherent photopion production models.

There has been an ongoing effort to incorporate additional models for the nuclear incoherent cross section. Experimental input from a “Conjoined” or similar themed analysis will provide insight into the applicability of the Glauber model utilized in this analysis or one such the Multicolisional Intranuclear Cascade Model (MCMC). See [28 & 29] for information on MCMC.

7.7.3 The ω background contribution.

Recent efforts within the PrimEx collaboration have shown that there is a small but finite elastic pion signal from coherent ω production. The ω cross section on ^{12}C is large, but has a very small acceptance at HyCal (Figure 7.5). We propose to simulate the ω cross section in simulation and reconstruct hybrid mass spectrums (Figure 7.6). These reconstructed spectra do show an inelastic background with elastic peak that broadens with increasing pion angle. We then intend to scale these hybrid mass spectrums to determine the elastic pion ω contribution. The scaled spectra will be subtracted from experimental hybrid mass spectrums before any elastic yield extraction is performed.

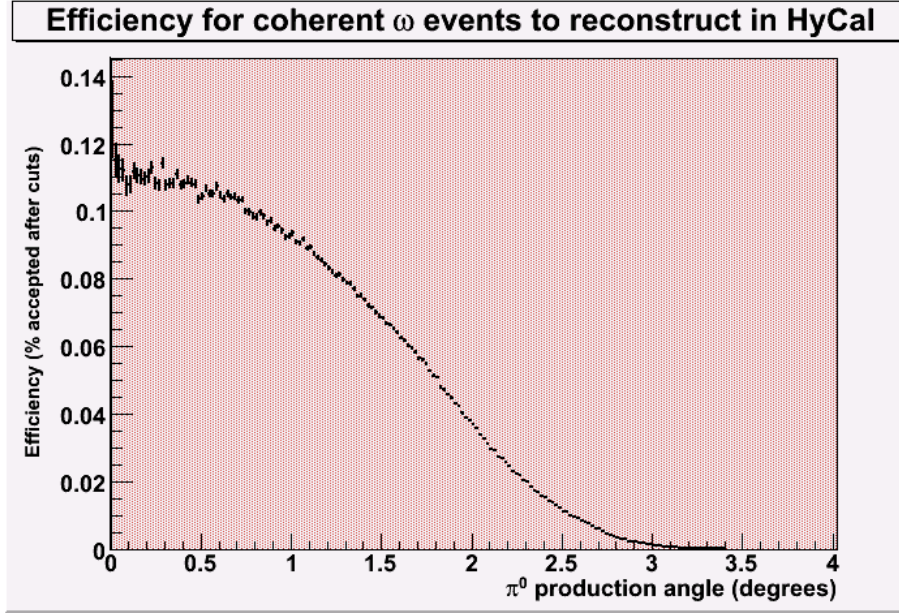


Figure 7.5: Efficiency to accept coherent ω event

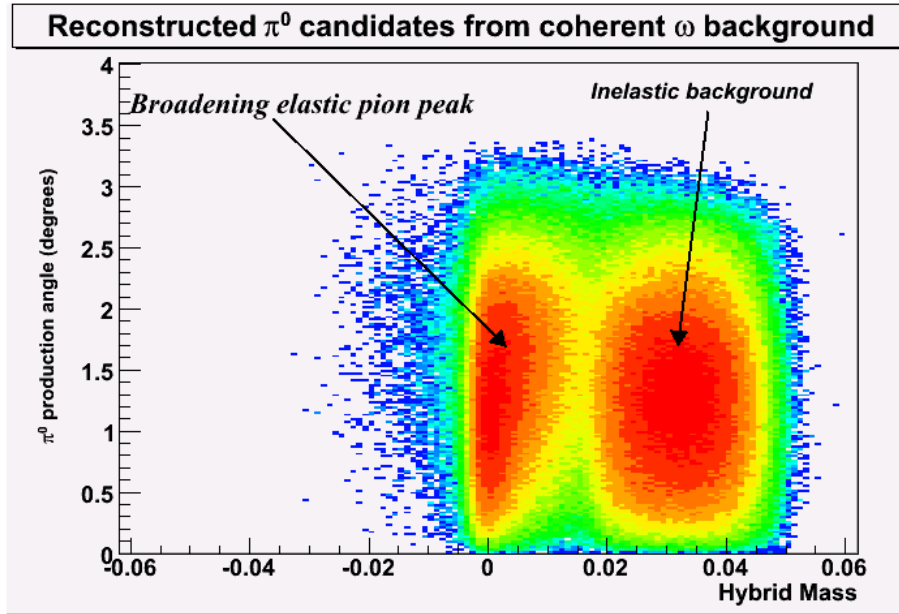


Figure 7.6: Reconstructed π^0 candidate spectra from coherent ω background

7.7.4 Evolving the cross sections to one photon energy.

Finally, we propose to interpolate the cross section to a single photon energy. This energy is, to first order, the weighted average of the photon energy spectrum in Figure (??). To accomplish this, we need to normalize the cross section functions

$$d\sigma^{\text{process}}(E_\gamma, \theta)/d\theta,$$

$$A_2 \Delta\theta \sum_{\theta=0}^{\theta_{\max}} D^{\text{Coh}}(\theta) = K_2 \varepsilon^{\text{Coh}} \int_0^{\theta_{\max}} d\theta \int_{\text{Lo}-E}^{\text{Hi}-E} dE_\gamma \frac{d\sigma^{\text{Coh}}(E_\gamma, \theta)}{d\theta} \Phi(E_\gamma) \quad (7.11)$$

$$2\sqrt{A_1 A_2} \cos \phi \Delta\theta \sum_{\theta=0}^{\theta_{\max}} D^{\text{Inter}}(\theta) = K_{12} \varepsilon^{\text{Inter}} \int_0^{\theta_{\max}} d\theta \int_{\text{Lo}-E}^{\text{Hi}-E} dE_\gamma \frac{d\sigma^{\text{Inter}}(E_\gamma, \theta)}{d\theta} \Phi(E_\gamma) \quad (7.12)$$

$$A_3 \Delta\theta \sum_{\theta=0}^{\theta_{\max}} D^{\text{Coh}}(\theta) = K_3 \varepsilon^{\text{Incoh}} \int_0^{\theta_{\max}} d\theta \int_{\text{Lo}-E}^{\text{Hi}-E} dE_\gamma \frac{d\sigma^{\text{Incoh}}(E_\gamma, \theta)}{d\theta} \Phi(E_\gamma) \quad (7.13)$$

Do the sums and integrals numerically, and find the normalization constants K_2 , and K_{12} and K_3 .

- i. Define the best-fit cross section as (Equation 7.14)

$$\frac{d\sigma^{\text{Fit}}(E_\gamma, \theta)}{d\theta} \equiv \left[K_1 \frac{d\sigma^{\text{Prim}}(E_\gamma, \theta)}{d\theta} + K_2 \frac{d\sigma^{\text{Coh}}(E_\gamma, \theta)}{d\theta} + K_{12} \frac{d\sigma^{\text{Inter}}(E_\gamma, \theta)}{d\theta} + K_3 \frac{d\sigma^{\text{Incoh}}(E_\gamma, \theta)}{d\theta} \right]$$

To evolve the cross sections to one tagged photon energy E_0 find,

$$\frac{d\sigma^{\text{evolved}}(E_0, \theta)}{d\theta} \equiv \frac{d\sigma^{\text{cor}}(\theta)}{d\theta} \left[\frac{\frac{d\sigma^{\text{Fit}}(E_0, \theta)}{d\theta}}{\int_{\text{Lo}-E}^{\text{Hi}-E} \frac{d\sigma^{\text{Fit}}(E_\gamma, \theta)}{d\theta} \Phi(E_\gamma) dE_\gamma} \right] \quad (7.15)$$

APPENDICES

APPENDIX A

RUN LIST FOR TAGGER RADIATORS A AND B

Tagger Radiator A (total = 78)

4593	4596	4597	4598	4599	4600	4606	4607	4610	4611	4612
4613	4614	4615	4618	4619	4620	4621	4622	4623	4624	4625
4626	4627	4628	4629	4630	4631	4632	4637	4638	4639	4640
4654	4655	4656	4677	4680	4681	4682	4685	4686	4687	4688
4689	4690	4691	4692	4693	4694	4695	4696	4698	4699	4700
4701	4697	4702	4703	4704	4705	4706	4707	4708	4717	4718
4719	4720	4721	4722	4723	4724	4725	4731	4732	4733	4734
4738										

Tagger Radiator B (total = 176)

4491	4492	4493	4494	4495	4496	4497	4498	4499	4500	4501
4502	4742	4745	4746	4747	4749	4750	4751	4753	4754	4760
4761	4762	4763	4764	4765	4766	4767	4768	4775	4776	4976
4977	4978	4979	4980	4981	4982	4983	4984	4986	4987	4988
4989	4997	4998	4999	5000	5002	5003	5004	5005	5006	5007
5009	5010	5011	5012	5013	5014	5015	5016	5017	5018	5020
5024	5025	5029	5030	5028	5031	5032	5033	5034	5035	5036
5037	5038	5039	5040	5041	5042	5043	5044	5045	5047	5048
5049	5050	5051	5052	5053	5054	5055	5056	5057	5058	5059
5061	5062	5066	5067	5068	5159	5160	5161	5162	5163	5164
5165	5166	5167	5168	5169	5170	5171	5172	5173	5174	5175
5177	5180	5181	5182	5183	5186	5187	5188	5189	5190	5191
5192	5194	5195	5196	5197	5198	5200	5201	5202	5203	5204
5205	5206	5208	5209	5210	5213	5214	5215	5216	5218	5219
5221	5222	5223	5224	5226	5228	5229	5233	5234	5236	5237
5239	5240	5241	5432	5433	5434	5439	5435	5436	5437	5438

APPENDIX B

LIST OF HYCAL SIMULATION ANODE/DYNODE CHANNELS

Tungstate ID in database

1349 -- when 1 or more tungstate channels off
1299 -- when 2 or more tungstate channels off
1657-- when 3 or more tungstate channels off
1887 -- when 4 or more tungstate channels off
1599-- when 5 or more tungstate channels off
1086 -- when 6 or more tungstate channels off
1438 -- when 7 or more tungstate channels off
1141 -- when 8 or more tungstate channels off
1730 -- when 9 or more tungstate channels off
2038 -- when 10 or more tungstate channels off

Glass ID in database

267 -- when 1 or more glass channels off
216 -- when 2 or more glass channels off
795 -- when 3 or more glass channels off
862 -- when 4 or more glass channels off
49 -- when 5 or more glass channels off
125 -- when 6 or more glass channels off
812 -- when 7 or more glass channels off
266 -- when 8 or more glass channels off
58 -- when 9 or more glass channels off
132 -- when 10 or more glass channels off

APPENDIX C

PHOTON FLUX AND ENERGY BINNING

Mean Bin Energy	Energy Bin Width	Photons in Energy Bin
5.49384	0.00441	1.56E+10
5.49122	0.00415	1.19E+10
5.48595	0.00513	2.30E+10
5.48314	0.00403	1.26E+10
5.48044	0.00531	2.08E+10
5.47391	0.00392	1.15E+10
5.46984	0.00513	1.98E+10
5.46845	0.00403	1.36E+10
5.45832	0.00531	2.32E+10
5.45593	0.00426	1.27E+10
5.45234	0.00519	2.07E+10
5.44978	0.00427	1.39E+10
5.44298	0.00524	2.19E+10
5.43954	0.0045	1.32E+10
5.43213	0.00548	1.94E+10
5.42884	0.00472	1.38E+10
5.42696	0.00531	2.20E+10
5.42313	0.00484	1.57E+10
5.41695	0.00559	2.19E+10
5.41396	0.0049	1.48E+10
5.40499	0.00542	2.17E+10
5.4027	0.0049	1.54E+10
5.39755	0.00571	2.22E+10
5.39266	0.00502	1.70E+10
5.38815	0.00547	2.06E+10
5.3816	0.00508	1.66E+10
5.37639	0.00576	2.48E+10
5.37036	0.00513	1.50E+10
5.36719	0.0056	2.19E+10
5.3631	0.00513	1.76E+10
5.35621	0.00588	2.54E+10
5.35173	0.00513	1.54E+10
5.34672	0.0057	2.14E+10
5.3414	0.00502	1.62E+10
5.33686	0.00582	2.75E+10
5.33162	0.0053	1.64E+10
5.32564	0.00588	2.27E+10
5.32025	0.00525	1.59E+10
5.31512	0.00576	2.45E+10
5.30905	0.00519	1.72E+10
5.30244	0.00577	2.61E+10
5.29599	0.00541	1.33E+10
5.29296	0.00588	1.96E+10
5.28778	0.00525	1.26E+10

5.28228	0.00576	2.79E+10
5.27752	0.00519	1.76E+10
5.27044	0.00588	2.22E+10
5.26724	0.00536	1.62E+10
5.26038	0.00565	2.61E+10
5.25487	0.0056	1.74E+10
5.24893	0.00582	2.42E+10
5.24374	0.00541	1.75E+10
5.23609	0.00565	2.30E+10
5.23373	0.00536	1.79E+10
5.22954	0.00577	2.60E+10
5.2235	0.00553	1.75E+10
5.21705	0.00565	2.46E+10
5.21144	0.00565	1.84E+10
5.20711	0.00576	2.54E+10
5.20128	0.00548	1.92E+10
5.19448	0.00559	2.42E+10
5.19033	0.0053	1.80E+10
5.18389	0.00588	2.42E+10
5.17724	0.00536	1.65E+10
5.17431	0.00565	2.42E+10
5.16683	0.00565	1.75E+10
5.16261	0.00554	2.39E+10
5.15642	0.00582	2.28E+10
5.15089	0.00576	2.41E+10
5.14532	0.00554	2.04E+10
5.14063	0.00559	2.18E+10
5.13615	0.00536	1.84E+10
5.13048	0.00582	2.72E+10
5.12404	0.00554	1.86E+10
5.11781	0.00571	2.25E+10
5.11295	0.00559	1.94E+10
5.10738	0.00559	2.60E+10
5.10085	0.00576	2.01E+10
5.09635	0.00542	2.00E+10
5.09214	0.00594	1.79E+10
5.08492	0.00571	2.98E+10
5.07409	0.00565	1.78E+10
5.07529	0.00553	2.45E+10
5.06646	0.00542	2.16E+10
5.06064	0.00588	2.78E+10
5.05612	0.00548	1.48E+10
5.0506	0.00571	1.76E+10
5.04703	0.0057	1.57E+10
5.04257	0.00554	3.02E+10
5.03342	0.00582	2.06E+10
5.03036	0.00548	2.27E+10
5.02313	0.00594	2.26E+10
5.0184	0.00524	2.27E+10
5.01158	0.00611	2.08E+10

5.00678	0.00559	2.16E+10
4.9999	0.00577	2.11E+10
4.99359	0.00548	2.67E+10
4.98853	0.00547	1.83E+10
4.9838	0.00577	2.46E+10
4.97554	0.00553	2.10E+10
4.97259	0.00571	2.58E+10
4.96647	0.00571	1.99E+10
4.96149	0.00553	2.10E+10
4.95625	0.00576	1.92E+10
4.95142	0.00548	2.74E+10
4.94391	0.00594	2.24E+10
4.9374	0.00536	2.33E+10
4.93132	0.00605	2.20E+10
4.92879	0.00525	1.94E+10
4.92114	0.00611	2.47E+10
4.91568	0.00559	3.04E+10
4.91136	0.00571	7.63E+09
4.90384	0.00548	2.45E+09
4.89774	0.00548	5.40E+08

APPENDIX D

CROSS SECTIONS

Angle Bin (degrees)	Uncorrected Cross Section (μbarns)	Uncorrected CS error (μbarns)	Efficiency Corrected CS (μbarns)	Corrected CS error (μbarns)
0.01	2.22914	0.167333	3.81858	0.286645
0.03	6.05858	0.295063	10.384	0.50572
0.05	7.67464	0.336471	13.3095	0.583515
0.07	7.57231	0.336187	12.9345	0.57425
0.09	6.8693	0.321346	11.8542	0.55454
0.11	5.82139	0.299356	10.0114	0.514821
0.13	5.11029	0.293655	8.77752	0.504387
0.15	4.58605	0.278837	7.8619	0.478013
0.17	3.95478	0.267633	6.79137	0.459594
0.19	3.9249	0.260385	6.7728	0.449319
0.21	3.60885	0.256684	6.22404	0.442693
0.23	3.62335	0.254689	6.26277	0.440216
0.25	3.05372	0.246415	5.2905	0.426908
0.27	3.16335	0.248221	5.48406	0.43032
0.29	2.97657	0.246674	5.16921	0.428383
0.31	3.73516	0.247191	6.47626	0.428594
0.33	3.7054	0.243289	6.47748	0.425299
0.35	3.65001	0.250904	6.38085	0.438624
0.37	3.21981	0.252298	5.65126	0.442823
0.39	3.5149	0.245897	6.17266	0.43183
0.41	3.68036	0.249885	6.45204	0.438074
0.43	4.1475	0.256187	7.29323	0.450496
0.45	4.13427	0.255189	7.32924	0.452399
0.47	4.22843	0.255439	7.52824	0.45478
0.49	3.56676	0.253811	6.36327	0.452811
0.51	3.77957	0.25293	6.73883	0.450964
0.53	4.51829	0.262337	8.07602	0.468903
0.55	4.66043	0.266079	8.35711	0.477134
0.57	4.53367	0.270123	8.23116	0.490426
0.59	4.62841	0.270005	8.36459	0.487961
0.61	4.79451	0.279979	8.6961	0.507815
0.63	5.17007	0.281908	9.37433	0.511155
0.65	5.32231	0.279294	9.66602	0.507236
0.67	5.86308	0.285617	10.7254	0.522481
0.69	5.08088	0.282699	9.33095	0.519173
0.71	5.27994	0.280888	9.74937	0.518658
0.73	6.02271	0.286398	11.185	0.531881
0.75	6.69491	0.295603	12.4752	0.550825
0.77	6.12782	0.296573	11.4439	0.55386
0.79	6.54705	0.300206	12.2483	0.561628
0.81	7.21044	0.31493	13.6665	0.59691
0.83	7.16967	0.311673	13.6163	0.591914
0.85	6.96979	0.30962	13.2865	0.590228

0.87	8.02364	0.316647	15.4146	0.608327
0.89	7.881	0.319854	15.2396	0.618505
0.91	7.71754	0.325683	14.9185	0.629568
0.93	8.02999	0.325291	15.5659	0.630566
0.95	8.45113	0.333425	16.4781	0.650114
0.97	8.60241	0.337418	16.8231	0.659862
0.99	9.22781	0.342018	18.0777	0.670027
1.01	9.28215	0.342111	18.2964	0.67435
1.03	8.92667	0.339491	17.8386	0.678421
1.05	9.35485	0.346465	18.7615	0.694849
1.07	10.0632	0.355998	20.1225	0.71186
1.09	9.10091	0.344526	18.3529	0.69477
1.11	9.81692	0.351763	19.8996	0.713049
1.13	10.4849	0.360803	21.4434	0.737901
1.15	10.0816	0.354022	20.6306	0.72446
1.17	10.7152	0.361686	22.0634	0.744736
1.19	10.6249	0.365109	21.9875	0.755566
1.21	10.2577	0.361157	21.4039	0.753595
1.23	10.4183	0.361421	21.8302	0.757312
1.25	10.125	0.363357	21.3955	0.767821
1.27	11.0169	0.371001	23.3731	0.787105
1.29	11.275	0.367546	24.1262	0.786475
1.31	11.5658	0.372887	24.8633	0.801604
1.33	11.3547	0.374679	24.516	0.80897
1.35	11.2642	0.369623	24.6242	0.808018
1.37	11.1926	0.370054	24.6543	0.815134
1.39	11.1754	0.370915	24.6123	0.816888
1.41	11.8096	0.374934	26.2377	0.833003
1.43	11.5073	0.368845	25.7643	0.825826
1.45	11.4437	0.372801	25.8164	0.84102
1.47	12.2588	0.378995	27.7872	0.859075
1.49	11.6054	0.374679	26.5909	0.858486
1.51	12.0001	0.375189	27.741	0.867335
1.53	10.7322	0.36824	25.0307	0.858845
1.55	11.0651	0.370657	25.9159	0.868126
1.57	11.4972	0.370657	27.2401	0.878192
1.59	11.4749	0.374168	27.7425	0.904613
1.61	10.6912	0.362303	25.8347	0.875483
1.63	10.9312	0.366503	26.7688	0.897511
1.65	11.1439	0.371001	27.5493	0.917168
1.67	10.8872	0.363971	27.2484	0.910941
1.69	11.4635	0.36798	29.08	0.933468
1.71	10.3154	0.355819	26.4264	0.911554
1.73	10.9698	0.359652	28.3648	0.929961
1.75	10.9993	0.36283	28.7585	0.948646
1.77	9.75919	0.346832	25.9148	0.920987
1.79	9.61859	0.347016	25.9848	0.93747
1.81	9.37696	0.343414	25.6792	0.940453
1.83	9.30615	0.342111	25.8285	0.949503
1.85	9.67661	0.344248	27.3639	0.973478

1.87	8.94688	0.339491	25.784	0.978378
1.89	9.18233	0.332179	26.8059	0.969726
1.91	9.46003	0.334666	28.1606	0.996233
1.93	8.45493	0.325879	25.5145	0.983408
1.95	8.54001	0.322633	26.3754	0.996438
1.97	7.75864	0.320053	24.5363	1.01215
1.99	7.7055	0.307553	24.7922	0.989541
2.01	8.38308	0.317953	27.6219	1.04765
2.03	7.28058	0.302534	24.349	1.01179
2.05	7.17748	0.301584	24.705	1.03806
2.07	8.00341	0.307345	28.2396	1.08445
2.09	6.8277	0.29224	24.6192	1.05375
2.11	6.97591	0.293655	25.9121	1.09078
2.13	6.35493	0.277921	24.2047	1.05855
2.15	6.83153	0.284498	26.7118	1.11241
2.17	5.60407	0.267275	22.851	1.08983
2.19	5.77791	0.263671	23.9595	1.09337
2.21	5.30288	0.258047	22.9488	1.11673
2.23	4.84124	0.252172	21.5687	1.12347
2.25	5.04697	0.25065	23.33	1.15865
2.27	4.37122	0.238256	21.1383	1.15215
2.29	4.31851	0.239324	21.8224	1.20936
2.31	3.92594	0.228695	20.5094	1.19472
2.33	4.05333	0.227015	22.4002	1.25457
2.35	3.79573	0.21857	21.8517	1.25829
2.37	3.50042	0.211148	21.2223	1.28015
2.39	2.97849	0.201883	18.8592	1.27828
2.41	3.22722	0.202986	21.5601	1.35609
2.43	2.8489	0.201408	20.095	1.42066
2.45	2.62674	0.18916	19.5247	1.40604
2.47	2.58247	0.188654	19.9893	1.46025
2.49	1.94734	0.172771	16.0348	1.42264
2.51	1.97246	0.16676	16.7787	1.41855
2.53	1.98661	0.172217	18.0678	1.56628
2.55	2.00724	0.170168	19.0791	1.61747
2.57	1.54345	0.157313	15.5927	1.58925
2.59	1.96951	0.161514	20.7403	1.70085
2.61	1.55817	0.153828	17.6133	1.73885
2.63	1.34523	0.150475	16.3232	1.82587
2.65	1.26281	0.136471	15.9702	1.72589
2.67	1.19201	0.136705	16.494	1.89159
2.69	1.02608	0.130009	14.8713	1.88424
2.71	0.959154	0.118187	15.1313	1.86448
2.73	0.707755	0.108626	12.0854	1.85487
2.75	0.569233	0.10565	10.5717	1.96212
2.77	0.546535	0.10165	10.9657	2.0395
2.79	0.643884	0.10165	14.3973	2.2729
2.81	0.575679	0.0994294	13.9616	2.4114
2.83	0.402933	0.08785	10.7182	2.33684
2.85	0.336511	0.08785	9.5851	2.5023

2.87	0.421334	0.0910586	13.5097	2.9197
2.89	0.231563	0.0753433	8.06684	2.62469
2.91	0.264286	0.0829968	10.0001	3.14047
2.93	0.0690485	0.0696236	2.87649	2.90045
2.95	0.121068	0.0672946	5.537	3.07769
2.97	0.0832328	0.0653713	4.18973	3.29063
2.99	0.0297191	0.0613445	1.6151	3.33379

REFERENCES

- [1] Goity, Bernstein, & Holstein, Phys. Rev. D66, 076014, 1-10 (2002)
- [2] Ananthanaravan and Moussallam, JHEP 0205 (2002) 052
- [3] See *e.g.* Dynamics of the Standard Model, J.F. Donoghue, E. Golowich, and B.R. Holstein, Cambridge University Press (1992).
- [4] J.S. Bell and R. Jaciw, Nouvo Cimento 60A, 46 (1969). S.L. Adler, Phys. Rev. 177, 2426 (1969).
- [5] R.M. Barnett *et al.*, Review of Particle Physics, Phys. Rev. D54,1 (1996).
- [6] J. Bijnens, A. Bramon and F. Cornet, Phys. Rev. Lett. 61 (1988) 1453.
- [7] J.F. Donoghue, B.R. Holstein, Y.C.R. Lin, Phys. Rev. Lett., vol. 55. (1985), 2766;
J.F. Donoghue, B. Wyler, Nucl. Phys., B316, (1989), 289.
- [8] J. Bijnens, J. Prades, Z. Phys. C64, (1994), 475. J. Bijnens, private communication with PrimEx collaboration senior members.
- [9] G. von Dardel *et al.*, Phys. Lett., vol. 4, no. 1, (1963), 51.
- [10] H.W. Atherton *et al.*, Phys. Lett., vol. 158B, no. 1 (1985), 81.
- [11] D.A. Williams *et al.*, Phys. Rev. D, vol. 38, no. 5, (1988), 1365.
- [12] H. Primakoff, Phys. Rev. 81, 899 (1951).
- [13] G. Bellettini, *et al.*, Il Nouvo Cimento, vol. 40, no. 4, (1965), 1139.
- [14] G. Bellettini *et al.*, Il Nouvo Cimento, vol 66, no. 1, (1970), 243.
- [15] V.I. Kryshkin, *et al.*, Sov. Phys. JETP, vol 30, no. 6, (1970), 1037.
- [16] A. Browman *et al.*, Phys. Rev. Lett., vol. 33, (1974), 1400.
- [17] A. Browman *et al.*, Phys. Rev. Lett., vol 32 (1974), 1067.
- [18] A. M. Bernstein, Nucl. Phys. A623 (1997) 178c.

- [19] A. Gasparian, S. Gevorkyan, “Theoretical Part of the PrimEx experiment”.
Private notes, July5, 2004.
- [20] K. Gottfried, D. Yennie, Phys. Rev., 182, 1592 (1969).
- [21] Primex Note 28. Available at PrimEx Website (<http://www.jlab.org/primex/>) or
(http://www.jlab.org/primex/primex_notes/primex_notes.html).
- [22] NIM A 440 (200) 263.
- [23] A. Gasparian. “Performance of PbWO₄ Crystal Detectors for a High Resolution
Hybrid Electromagnetic Calorimeter at Jefferson Lab (Proceedings Contribution
to Calor-2002)”. Primex Note 10. Available at PrimEx Website
(<http://www.jlab.org/primex/>) or
(http://www.jlab.org/primex/primex_notes/primex_notes.html).
- [24] Primex Note 46. Available at PrimEx Website (<http://www.jlab.org/primex/>) or
(http://www.jlab.org/primex/primex_notes/primex_notes.html).
- [25] G. Morpurgo, Nuovo Cimento, 31, (1964), 569.
- [26] G. Faldt, Nucl. Phys. B43, (1972), 591.
- [27] Primex Note 50. Available at PrimEx Website (<http://www.jlab.org/primex/>) or
(http://www.jlab.org/primex/primex_notes/primex_notes.html).
- [28] T.E Rodriques et. al. Phys. Rev. C 71, 051603 (R) (2005)
- [29] T.E. Rodriques et. al. Phys. Rev. C 69, 064611 (2004)